UNIVERSITÀ DEGLI STUDI DI NAPOLI "FEDERICO II"

Scuola Politecnica e delle Scienze di Base

Area Didattica di Scienze Matematiche Fisiche e Naturali

Dipartimento di Fisica "Ettore Pancini"

Laurea Magistrale in Fisica

Principles and characterization of superconducting single- and two-qubit gates

Relatori:
Francesco Tafuri
Davide Massarotti
Halima Giovanna Ahmad

Candidato:
Asen Lyubenov Georgiev
Matr. *N*94000724

Anno Accademico 2021/2022

Contents

1 Introduction

Today's world is becoming hungrier and hungrier for computational power. Quantum computers are viewed as capable of propelling our computation capabilities to a new level. For example, they have been proposed to solve analytically many-body problems, like the study of large molecules [1], [2] and to provide noticeable speed-up in tasks like numbers factorization, which would break modern Cryptography [3]. These devices are based on Quantum Mechanics and are promoting an amazing progress on our understanding of quantum protocols, quantum algorithms and of the quantum hardware, which makes possible the realization of a Quantum computer. There has been much progress in this area and today Quantum computers are starting to become a reality.

One of the most advanced Quantum computers is based on solid state systems like superconducting devices. The operation of a superconducting quantum computer is based on very advanced knowledge on physics and technology. The amazing notion which is behind the operation of a superconducting qubit is that they obey to the same rules of Quantum mechanics. As a matter of fact, superconducting qubits allow to artificially implement an atom-like system, i.e. quantized levels. The building blocks of superconducting quantum computers are the tunnel Josephson junctions, which behave as giant atoms. By carefully engineering their circuital features, they provide practical ways to access to macroscopic Quantum Mechanics.

Superconducting quantum circuits have unique technological advantages in terms of scalability and integration. At the same time they are strongly affected by the interaction with the environment, thus providing a unique possibility to study a variety of complex fundamental problems on noise, dephasing, relaxation, decoherence, being the qubit somehow a very sophisticated sensor. The decoherence in superconducting quantum systems plays a fundamental role also in the implementation of high-quality Quantum Gates, the basic operations in Quantum algorithms.

In order to perform quantum computing tasks, qubits must be able to maintain quantum coherence for the overall algorithm duration. Coherence times and the ability to perform gates are tightly related to design characteristics of the device. Leading companies and research groups have developed a large variety of geometries and architectures, which may be protected by non-disclosure agreement, as for the system studied in this thesis. Specifically speaking, this work comes within a collaboration between Seeqc, QuantWare and UniNa, and hardware details on a deeper level cannot be disclosed. Nevertheless, the main goal of this project is not meant to discuss the hardware chip design and specification, but to provide a self-consistent and general protocol for single- and two-qubit systems characterization suitable for any superconducting multi-qubit systems in the transmon regime.

We hereby discuss in detail the sequence of experimental techniques that must be used in order to achieve high-performance superconducting transmon qubits. Such protocols are also a powerful tool for the understanding of the dissipation and decoherence processes due to the unavoidable interaction between the qubit, the user and the environment.

A special focus is given on the optimization of the control signals. This is a crucial step, because the interaction with qubits highly impacts their performance, i.e. how many errors occur when we perform tasks on them. Such optimization protocols are necessary in order to achieve high performing single- and multi-qubit operations, which are essential for quantum computing.

In addition, we study the physics of two coupled superconducting transmon qubits, by showing our first results on two-qubits iSWAP gate. This is not only a crucial step towards the implementation of scalable superconducting Quantum computers, but it also underlines the fundamental role played by control optimization techniques in order to achieve state of-the-art multi-qubit gate fidelities.

In Chapter 2 we are going to set the theoretical principles of superconducting quantum computation. There we discuss the importance of superconductivity (Section 2.2), quantum circuit electrodynamics (Sections 2.3-2.5), operations and performance of the single qubits (Section 2.8) and coupled qubits (Sections 2.9 and 2.10). In Chapter 3 we describe the experimental set-up used in this work. We start with the chip design (Section 3.1), then we proceed with the description of the cooling mechanism of the dilution refrigerator (Section 3.2). Afterwards, we discuss the cryogenic and room-temperature electronics employed in the experiments (Section 3.3) and finally we describe the instruments used for the characterization of qubits (Sections 3.4 and 3.5). In Chapter 4 we are going to explain all the protocols used for the characterization of the qubits and their performance evaluation. In Sections 4.1-4.3 we explore all the characterization procedures necessary to study the relevant features of the qubits. Then, in Sections 4.4 and 4.5 we discuss the protocols for signal optimization and how to evaluate the qubit performance. We also discuss a protocol that couples two qubits (Section 4.6). In Chapter 5 we show our experimental results and we are going to discuss their validity with respect to the theoretical expectations and results in literature.

2 Principles of superconducting qubits

2.1 Basic principle of quantum computing

In this Chapter, we will outline the basic concepts behind the implementation of a special class of qubits, namely the superconducting qubits.

While classical computers are binary system in which the information is encoded in just two possible bits (ones and zeros), quantum computers can encode the information in qubits, which correspond to a quantum vector $|\psi\rangle$ represented on the *Bloch sphere*. In Figure 2.1 the Bloch sphere is reported, for which each point of the spherical surface represents a possible quantum state. The orange arrow shows a generic vector $|\psi\rangle = \alpha|0\rangle + \beta|1\rangle$ [4], with $|\alpha|^2 + |\beta|^2 = 1$ since the Bloch sphere is unitary. The ground and excited states are also called *north pole* ($|0\rangle$) and *south pole* ($|1\rangle$), respectively. The generic operation consists of rotations of the vector $|\psi\rangle$, with corresponding variations of the angles (θ, φ) [4].

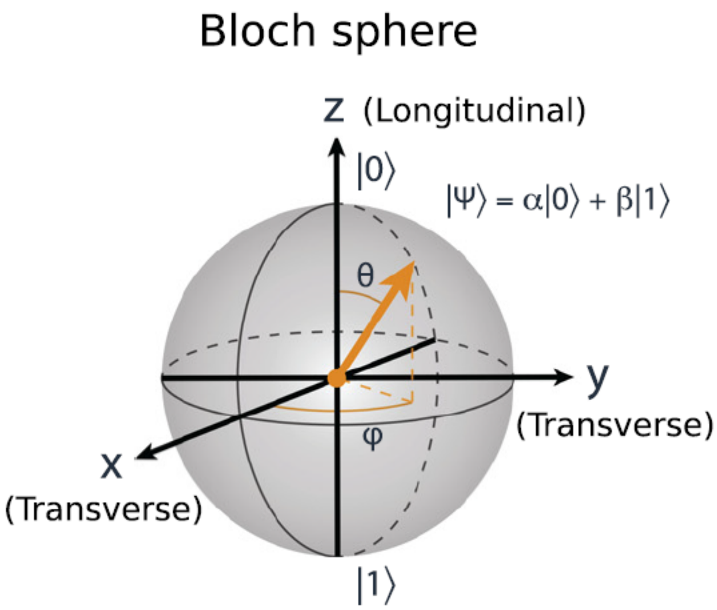

Figure 2.1: Representation on the Bloch sphere of the generic qubit state $|\psi\rangle = \alpha|0\rangle + \beta|1\rangle$.

One of the main challenges behind quantum computation is the physical realization of quantum computers, which must fulfill precise requirements, known as *Di Vincenzo criteria* [3]:

- Capability of building scalable system with many qubits (DV1).
- It must be possible to initialise the quantum system to a known state (DV2).
- High fidelity single and multi-qubit universal gate operations must be available (DV3).
- It must be possible to read out the state of the quantum system, typically via readout of individual qubits (DV4).

- A large number of single and 2-qubit gate operations must be performed within the coherence time of the qubit (DV5). During this mean time the qubit should not randomly go into another state.

Superconducting qubits are very well suited for these five criteria, since they are built on macroscopic circuits that can be realized and manipulated with large flexibility [4]. Superconducting qubit fabrication techniques are similar to those used in semiconducting technology for decades, thus they are promising for scalable systems. As it will be shown in the following, superconducting qubits are macroscopic circuits working at the microwave range, therefore it is possible to initialize the qubit in a known state [5] with commercially available electronics. There have been countless demonstrations of high fidelity single and 2-qubit gates [6], [7], [8]. Moreover, in specific circuital designs, the readout of the single qubits is done via a coupled resonator [9]. The DV5 criterion is more challenging for superconducting qubits, which are susceptible to the external environment. The qubit coherence time is the key parameter that has been improved of orders of magnitude in these last 20 years, and it has boosted the amazing progress in the field [9], [10], [11].

In this Chapter we will present the underlying physics of superconducting qubits and the techniques used to characterize isolated and coupled qubits. First of all, we will recall the advantages of using superconducting technology for these types of devices (Section 2.2). After that we will show how and under which conditions it is possible to establish a computational space by exploiting the peculiar non-linear behavior of the building element of a superconducting qubit, i.e. the Josephson junction (JJ) (Sections 2.3 and 2.4). The next logical step is to start describing how we can engineer superconducting quantum circuits and how to implement a physical coupling between two or more qubits (Sections 2.5, 2.6, 2.7 and 2.9). This will naturally lead to discuss the recent advancements in superconducting technologies. In particular, we will focus on a specific superconducting qubit implementation, i.e. the transmon, which is so far one of the most performing circuits, and up to now the main circuital design exploited by leading industries in the field, such as Google, IBM, etc. [12], [13]. The main goal of this work is indeed to provide a self-consistent experimental protocol for the characterization of the performances of single and multi-qubit transmon platforms for the implementation of high-fidelity single qubit gates (Section 2.10), a fundamental step in order to deal with two- and multi-qubit quantum gate operations.

2.2 Basic phenomenology of superconductors

Superconducting qubits are based on the superconductive state of matter, which is characterized by:

- Perfect conductivity: no heat dissipation
- Meissner effect: expulsion of external fields up to a certain critical field.

The conventional superconductors are described by the Bardeen - Cooper - Schriffer (BCS) theory [14]. According to this theory, the superconducting state occurs below a critical temperature T_c, of the order of a few Kelvin, because of the formation of the so called *Cooper pairs*. These are pairs of electrons with opposite spin, which form as a result of a collective perturbation of the lattice. More specifically, one electron interacts with the crystal lattice through the phonons of the material, it deforms the lattice and later another electron interacts with the deformed lattice [14]. The result of this process is the Cooper pair. It has a charge of $2e$, with e the electrical charge of an electron.

Cooper pairs in the superconductor are described by a macroscopic wave function,

$$|\psi\rangle = \psi_0 e^{i\varphi}, \tag{2.1}$$

where φ is the *gauge-invariant phase*. As in microscopic quantum objects like electrons, atoms or molecules, superconductors are capable to maintain a high coherence in their ground state, even if they are massive macroscopic systems. The energy dispersion relation is reported in Figure 2.2. It shows that there is an energy gap in the excitation spectrum. If the external sources of excitation provide an amount of energy E lower than the superconducting gap 2Δ, the Cooper pair remains in its fundamental state [15]. When a current of Cooper pairs is induced in the superconductors, there is no voltage drop across the system, i.e. the resistance of the superconductor becomes zero below T_c. Therefore, the power dissipated by Cooper pair flow is zero, and superconductors are dissipationless.

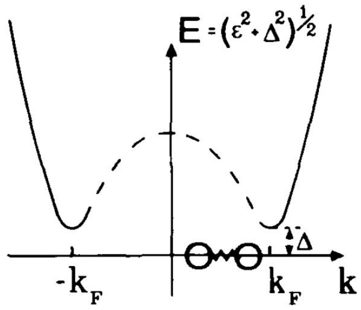

Figure 2.2: Excitation spectrum of a BCS superconductor. When the energy of the Cooper pairs is below 2Δ, the system is superconducting. Figure adapted from [15].

The Meissner effect is also called perfect diamagnetism, referring to the fact that, up to a critical external magnetic field, the superconductor is capable of expelling all the external magnetic fields, expect for a superficial region of thickness λ (London length) [16], as shown in Figure 2.3. If this critical field is reached, the superconductivity is broken [16]. The superconducting material undergoes a transition to its normal state (metallic state) as occurs when going above the critical temperature.

Superconductors are also characterized by an inductance given by:

$$L_s = L_k + L_g, \tag{2.2}$$

where L_s is the total inductance of the superconductor, L_g is the typical geometric inductance and L_k the *kinetic inductance*. The geometric inductance is related to the physical dimension of the superconductor and the composition of the superconducting material, and is the same as in the normal state. The kinetic inductance is related to superconducting parameters, like the London penetration depth λ [14], [17].

2.3 Circuit Quantum Electrodynamics with superconducting system

Circuit Quantum Electrodynamics studies the Hamiltonian of an electrical circuit [18]. In order to exploit the properties of superconductors for computational purposes, we can

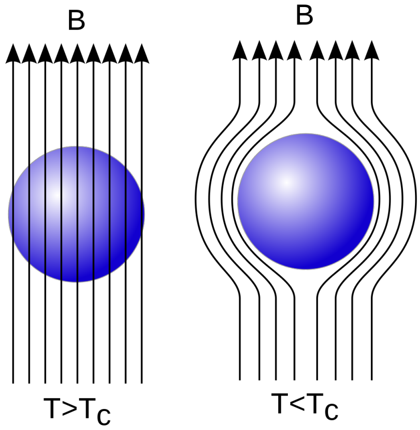

Figure 2.3: Meissner effect representation: in the superconducting state ($T < T_C$, with T_C the critical temperature) magnetic fields lines are expelled, whereas in the normal state ($T > T_C$) the magnetic lines penetrate the superconductor.

first consider a superconducting Quantum Harmonic Oscillator (QHO). In Figure 2.4 we show that a superconducting LC circuit behaves as a QHO with quantized levels [4]. This is also the model we use to describe the readout resonators mentioned in Section 3.1.

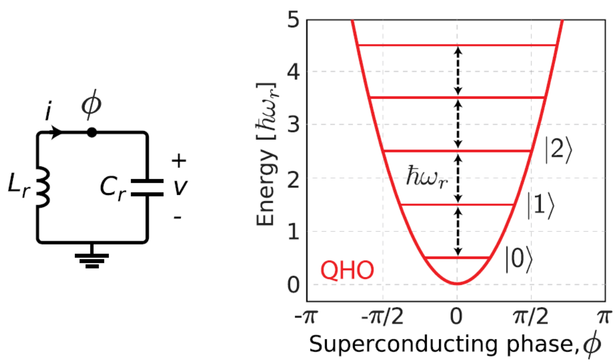

Figure 2.4: Isolated ideal LC oscillator (on the left) and quantized energy levels of an LC circuit which behaves as a quantum harmonic oscillator with frequency ω_r (on the right) [4]. L_r is the inductance and C_r is the capacity of the superconducting circuit, V is the voltage potential across C_r, i is the current flowing through the loop and ϕ is the gauge-invariant phase. Figure adapted from [4].

The Hamiltonian of the harmonic oscillator is the following [4]:

$$H_{QHO} = 4E_C n^2 + \frac{1}{2}E_L \phi^2, \tag{2.3}$$

where n is the excess number of Cooper pairs on the capacitance C_r, ϕ is the *gauge-invariant phase*, $E_C = \frac{e^2}{2C_r}$ is the charging energy and $E_L = \left(\frac{\Phi_0}{2\pi}\right)^2 \frac{1}{L_r}$ is the potential energy due to the inductance with $\Phi_0 = \frac{h}{2e} = \frac{\hbar\pi}{e}$ the superconducting flux quantum. ϕ and n are canonical conjugate observables, such that $[e^{i\phi}, n] = e^{i\phi}$ [4]. By introducing the creation and annihilation operators of single excitations of the harmonic oscillator as

$$n = n_{zpf} \times i(a - a^\dagger) \tag{2.4}$$

$$\phi = \phi_{zpf} \times (a + a^\dagger), \tag{2.5}$$

where $n_{zpf} = \left(\frac{E_L}{32E_C}\right)^{\frac{1}{4}}$ and $\phi_{zpf} = \left(\frac{2E_C}{E_L}\right)^{\frac{1}{4}}$, the QHO Hamiltonian reads as:

$$H_{QHO} = \hbar\omega_r \left(a^\dagger a + \frac{1}{2}\right), \tag{2.6}$$

where $\omega_r = \frac{\sqrt{8E_LE_C}}{\hbar} = \frac{1}{\sqrt{L_rC_r}}$ is the resonator frequency, which gives the spacing between the energy levels as shown in Figure 2.4. Despite having plenty of quantized levels, they are all equally spaced. As a consequence, it is not possible to distinguish between which levels a transition occurred [4]. The QHO is not suitable for building a proper computational space, since some degree of anharmonicity is necessary. This can be introduced through a non-linear inductance. The device that is able to achieve this goal is the Josephson Junction (JJ) [15].

2.4 Josephson Junctions in superconducting qubits

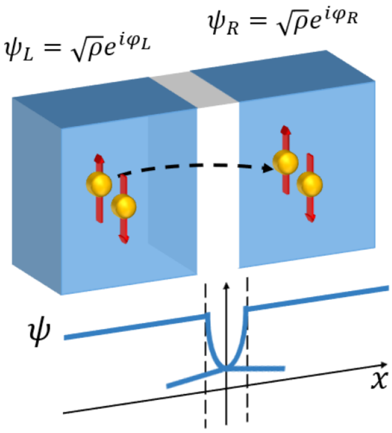

Figure 2.5: Schematic representation of a typical Josephson junction. The blue parts indicate the superconductors and the white part represents the barrier between the superconducting layer. The graph below shows the penetration of the macroscopic wave function $|\psi\rangle$ into the opposite superconductor. ρ is the Cooper pair density and $\varphi_{L,R}$ are the wave function phases, in the left (L) and right (R) superconducting electrodes.

A Josephson junction (JJ) is generally made of a non superconducting layer (barrier) sandwiched between two superconductors. A schematic representation is given in Figure 2.5. The barrier needs to be thin enough (of a thickness around 1 nm in the case of the most common barrier, which is an insulator) to enable the superconducting wave function of either superconducting electrodes to penetrate into each other. This allows for the tunneling of Cooper pairs, which gives rise to the Josephson effect. The Josephson effect is described by the 1^{st} and 2^{nd} Josephson equations [15]:

$$\begin{cases} I_s = I_C \sin\phi \\ \frac{\partial\phi}{\partial t} = \frac{2eV(t)}{\hbar} \end{cases} . \tag{2.7}$$

I_S is the superconducting current, V(t) is the voltage across the JJ and I_C is the critical current, i.e. the maximum supercurrent that the JJ can sustain. The JJ is important because it is the only device that is at the same time superconducting (no dissipation), non-linear (shown in the 1^{st} Josephson equation in Eq.2.7) and it allows to study the phase of quantum systems. The phase of a JJ is a macroscopic variable ($\phi = \varphi_L - \varphi_R$ phase difference between the two superconductors) which can be measured through I_S and $V(t)$, as shown in Eq.2.7. One can notice that in absence of any time variation of ϕ, the voltage drop across the junction is zero. Therefore, a JJ is a non-dissipative element.

Moreover, the JJ behaves as a non-linear inductance. This can be demonstrated by combining the two Josephson equations as follows:

$$\dot{I}_S = \frac{\partial I_S}{\partial \phi}\dot{\phi} = \frac{2e}{\hbar}\frac{\partial I_S}{\partial \phi}V \equiv L_J^{-1}V. \tag{2.8}$$

Therefore, the Josephson inductance can be defined as:

$$L_J = \frac{\hbar}{2eI_C \cos\phi}. \tag{2.9}$$

The non-linearity of L_J induces also a non-linearity in the potential energy of the JJ. By using the 2^{nd} Josephson equation in Eq. 2.7, we derive the phase dependence of the energy stored in the JJ, shown in Figure 2.6, as:

$$U_s = \int_0^t I_s(t)V(t)dt = \frac{\hbar}{2e}I_c\int_0^{\varphi}\sin\phi d\phi = \frac{\hbar I_C}{2e}(1-\cos\varphi), \tag{2.10}$$

where $E_J = \frac{\hbar I_C}{2e} = \frac{I_C\Phi_0}{2\pi}$ is the Josephson energy.

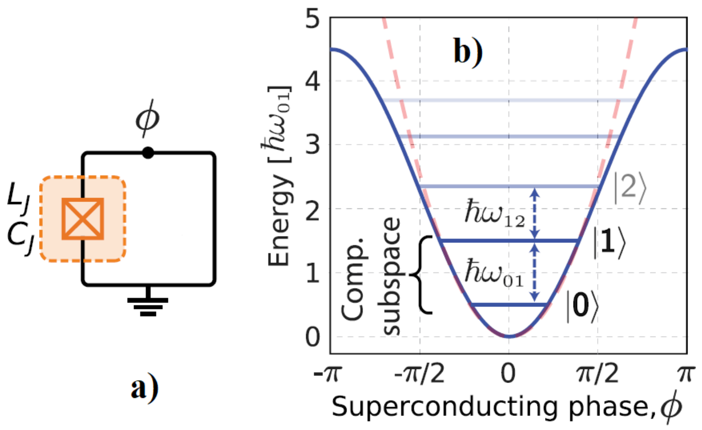

Figure 2.6: a) Circuit schematics of a Josephson junction. **b)** Non-linear potential energy of a Josephson junction (blue line), obtained from Eq. 2.11, compared to the potential energy of a harmonic oscillator (dashed red line), obtained from Eq. 2.3. Figure adapted from [4].

The barrier in Figure 2.5 behaves as a capacitance C_J in the JJ. In this way we have an object that has a non-linear inductance L_J and a capacitance C_J. The Hamiltonian of the circuit in Figure 2.6a is [15]:

$$H = 4E_C n^2 - E_J\cos\phi, \tag{2.11}$$

where E_C is the charging energy of the Josephson junction. In Figure 2.6b we show a plot of the energy levels of the JJ (solid blue line). The JJ provides not equally spaced energy levels and we call this feature anharmonicity. This allows us to establish a computational subspace by using the ground state ($|0\rangle$) and the first excited state ($|1\rangle$), respectively.

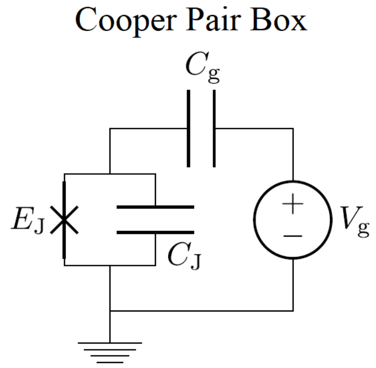

Figure 2.7: Circuit diagram of a Cooper Pair Box, with E_J the Josephson energy, C_J the capacitance of the Josephson junction, C_g the coupling capacitance and V_g the signal generated by the external electronics.

2.5 The Transmon Qubit

In order to define the functioning principle of a specific superconducting quantum circuit and the corresponding quantum observable, we introduce the ratio $\frac{E_J}{E_C}$. It defines the interplay between the two fundamental circuit energy scales, the Josephson energy E_J, related to the non linear inductance of the circuit, and the charging energy E_C, related to the capacitive elements. The first successful superconducting qubit was the Cooper Pair Box (CPB), which is shown in Figure 2.7. The CPB is characterized by a small superconducting island coupled to the JJ: the capacitance C_g couples the CPB to the external electronics in order to measure the charge, which is the quantum observable. Indeed, for the CPB the charge is a well defined quantum variable since the circuit satisfies the condition $E_J < E_C$.

The ratio $\frac{E_J}{E_C}$ is fundamental also in evaluating the impact of different noise sources on the behavior of the superconducting qubit [9]. The importance of this ratio is shown in Figure 2.8, which describes the dependence of the energy levels on the effective offset charge n_g [9]. The energy dispersion of the CPB is defined as [9]:

$$\epsilon \equiv E_m\left(n_g = \frac{1}{2}\right) - E_m(n_g = 0) \simeq (-1)^m E_C \frac{2^{4m+5}}{m!}\sqrt{\frac{2}{\pi}}\left(\frac{E_J}{2E_C}\right)^{\frac{m}{2}+\frac{3}{4}} e^{-\sqrt{8\frac{E_J}{E_C}}}. \quad (2.12)$$

An increase in $\frac{E_J}{E_C}$ results in an exponential decrease of energy dispersion with respect to the charge. Indeed, when the charging energy is larger or comparable to the Josephson energy, the circuit energy strongly depends on the charge fluctuations and noise. However, when the $\frac{E_J}{E_C}$ becomes sufficiently large $\left(\frac{E_J}{E_C} \gtrsim 50\right)$, such fluctuations can be suppressed, i.e. the qubit is well protected by charge noise.

A CPB shunted by a large capacitance allows to increase $\frac{E_J}{E_C}$ enough to suppress the charge fluctuations, but we need a different approach in order to read the qubit state without causing excitations to the qubit. The solution comes in a new circuit called transmon, which stands for *transmission line shunted plasma oscillation qubit* (Figure 2.9) [9]. For readout the transmon uses a *resonator*, which is represented in the microwave regime by a harmonic *LC oscillator* [9]. By shunting the qubit with the large capacitance C_B and the coupling capacitance C_g, it has been found that the transmon increases $\frac{E_J}{E_C}$ up to 50-100. The resulting capacitance C_Σ is larger than the CPB and provides a noticeable decrease in

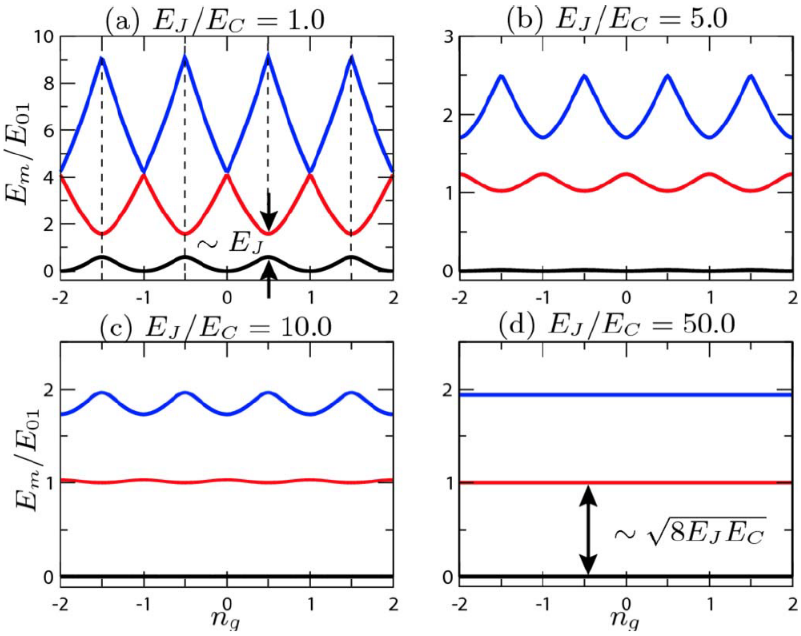

Figure 2.8: Charge dispersion of the qubit energy levels as a function of the number of Cooper pairs n_g for different $\frac{E_J}{E_C}$ ratios. Figure adapted from [9].

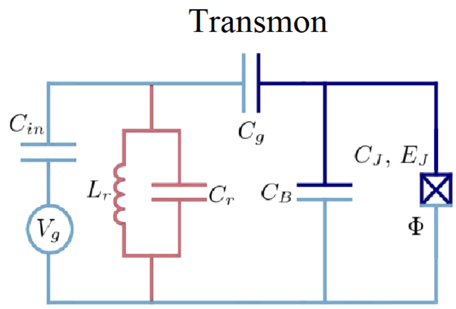

Figure 2.9: Circuit diagram of a transmon qubit: the Josephson junction is identified by C_J and E_J, C_B is the shunt capacitance, the resonator is identified as an LC circuit (L_r and C_r), C_g is the coupling capacitance and C_{in} is the coupling capacitance to the external electronics. Figure adapted from [9].

the charging energy E_C, which in turn increases $\frac{E_J}{E_C}$ [9].

A drawback related to the increase of the ratio $\frac{E_J}{E_C}$ is the reduction of the relative and absolute anharmonicity, defined as [9]:

$$\alpha \equiv E_{12} - E_{01} \qquad\qquad \alpha_r \equiv \frac{\alpha}{E_{01}}, \tag{2.13}$$

which sets the separation between the energy levels of the transmon. It is indeed possible to find approximate forms of these anharmonicities in the $\frac{E_J}{E_C} \to \infty$ limit, which are:

$$\alpha \simeq -E_C \qquad\qquad \alpha_r \simeq -\left(\frac{8E_J}{E_C}\right)^{-\frac{1}{2}}. \tag{2.14}$$

The dependence of the anharmonicities as a function of E_J/E_C is shown in Figure 2.10. Nevertheless, the anharmonicity only decreases as a power law, compared to the charge

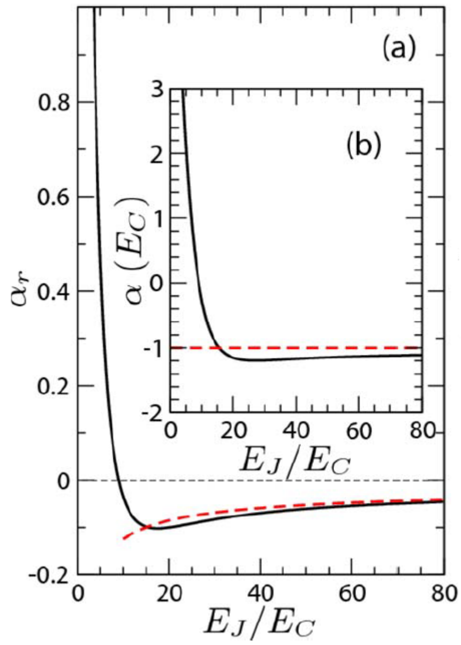

Figure 2.10: Relative **a)** and absolute **b)** anharmonicity at the charge degeneracy point ($n_g = \frac{1}{2}$) as a function of the ratio $\frac{E_J}{E_C}$ [9]. The solid curves correspond to the exact expressions [9], while the dotted red curves correspond to the approximated result in Eq. 2.14. Figure adapted from [9].

dispersion, which decreases exponentially [9]. For these reasons the transmon qubit is widely used as the fundamental qubit of small quantum processors, since the charge noise is strongly reduced without affecting too much the anharmonicity of the system.

2.5.1 Readout of qubits

The transmon qubit also drastically improves the readout of the qubit state, since the resonator provides an appropriate tool to read the qubit state without destroying it. This type of measurement is called Quantum Non Demolitive (QND), because the qubit does not collapse in a particular state when readout is attempted [4].

The Hamiltonian of the transmon, including the coupling with the superconducting resonator, is given by [4]:

$$H_{JC} = \omega_r \left(a^\dagger a + \frac{1}{2} \right) + \frac{\omega_q}{2} \sigma_z + g(\sigma_+ a + \sigma_- a^\dagger). \tag{2.15}$$

This is called Janynes-Cummings Hamiltonian [4] and is the sum of three terms: the resonator Hamiltonian, the qubit (two-level system) Hamiltonian and the interaction between the qubit and the resonator, respectively. ω_r is the resonance frequency of the resonator, ω_q is the frequency of the qubit, $g \approx e \sqrt{\frac{\omega_r}{C_r} \frac{C_g}{C_B + C_g + C_J}} \left(\frac{E_J}{E_C} \right)^{\frac{1}{4}}$ is the coupling between the qubit and the resonator with e the electron charge [9], $\sigma_{+,-}$ are the operators that represent excitation and de-excitation of the qubit and $a^\dagger$, a are the creation and annihilation operators of the resonator, respectively. When we couple the qubit to the resonator, we are creating a quantum system in which the observables of the qubit are entangled with those of the resonator.

Specifically speaking, transmon qubits generally work in the so-called *dispersive regime*

[4]. We define the *detuning* as $\Delta = |\omega_q - \omega_r|$ and we reach the dispersive regime for $g \ll \Delta$. In the dispersive regime, it is possible to develop a second-order perturbation theory with respect to $\frac{g}{\Delta}$ and obtain the corresponding Hamiltonian [4]:

$$H_{disp} = (\omega_r + \chi\sigma_z)\left(a^\dagger a + \frac{1}{2}\right) + \frac{\tilde{\omega}_q}{2}\sigma_z, \tag{2.16}$$

where $\chi = \frac{g^2}{\Delta}$ is known as *dispersive shift*. In this expression both qubit and resonator frequencies are renormalized: $\tilde{\omega}_q = \omega_q + \frac{g^2}{\Delta}$ and $\tilde{\omega}_r = \omega_r + \chi\sigma_z$. In the dispersive state, the resonance frequency of the resonator will shift positively or negatively accordingly to the detuning sign, as shown in Figure 2.11. In the dispersive regime, the qubit and the resonator are not directly exchanging energy, since they are far detuned from each other. For this reason we can probe the resonator with an appropriate RF signal and obtain information about the qubit state without destroying it, hence Quantum Non Demolitive measurement.

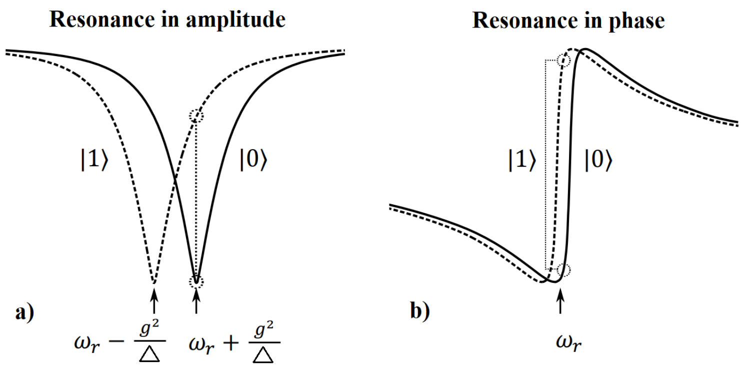

Figure 2.11: Effect of the dispersive shift on: **a)** the magnitude of the readout resonance, and **b**) the phase, depending on the qubit state $|0\rangle$ and $|1\rangle$. Figure adapted from [19].

2.5.2 Qubit Drive

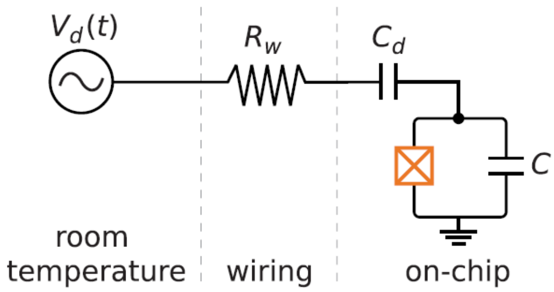

Figure 2.12: Circuit diagram of microwave drive line capacitively coupled to a transmon qubit. Figure adapted from [4].

As requested by the Di Vincenzo criteria, the qubit state has to be initialized in a particular quantum state. Moreover, to perform gate operations it is necessary to drive the qubit along the Bloch Sphere. As it will be shown in the next Sections, qubit frequencies of superconducting circuits are in the microwave range, therefore the qubit drive is done through an RF signal which resonates with the qubit, and the particular shape of the signal allows for different operations. In Figure 2.12 we show the circuit diagram of the transmon coupled to a microwave drive line.

In case of a capacitive coupling between the drive signal and the transmon, the Hamiltonian reads as:

$$H = H_{JC} + \frac{C_d}{C_\rho} V_d(t)\hat{Q}, \tag{2.17}$$

where H_{JC} is the Hamiltonian of the transmon in Eq. 2.15, $\hat{Q}$ is the charge operator, C_d is the coupling capacitance, $C_\rho = C_d + C$ and $V_d(t)$ is the drive signal. Since the charge in Eq. 2.17 can be written as [4]:

$$\hat{Q} = -iQ_{zpf}(a - a^\dagger), \tag{2.18}$$

with $Q_{zpf} = \sqrt{\frac{\hbar}{2Z}}$ and $Z = \sqrt{\frac{L}{C}}$, the Hamiltonian reads as:

$$H = \underbrace{-\frac{\omega_q}{2}\sigma_z}_{H_0} + \underbrace{\Omega V_d(t)\sigma_y}_{H_d}, \tag{2.19}$$

where $\Omega = \frac{C_d}{C_\rho} Q_{zpf}$ and $\omega_q = \frac{E_1 - E_0}{\hbar} - E_C$. Here we have omitted the resonator Hamiltonian term for the sake of simplicity. H_0 represents the Hamiltonian of the two-level system and H_d is the Hamiltonian of the drive signal. We now move into the *rotating frame* and rewrite H_d as [4]:

$$\tilde{H}_d = \Omega V_d(t)(\cos(\omega_q t)\sigma_y - \sin(\omega_q t)\sigma_x); \tag{2.20}$$

where $V_d(t)$ can be expressed as $V_d(t) = V_0 v(t)$ and $v(t)$ is:

$$v(t) = s(t)\sin(\omega_d t + \phi) = s(t)(\cos(\phi)\sin(\omega_d t) + \sin(\phi)\cos(\omega_d t)). \tag{2.21}$$

s(t) is a dimensionless envelope function, so that the amplitude of the drive is set by $V_0 s(t)$. We define the *in-phase component* as:

$$I = \cos(\phi) \tag{2.22}$$

and the *out-of-phase component* as:

$$Q = \sin(\phi). \tag{2.23}$$

The drive Hamiltonian in the rotating frame then becomes:

$$\tilde{H}_d = \Omega V_0 s(t)(I\sin(\omega_d t) - Q\cos(\omega_d t)) \cdot (\cos(\omega_q t)\sigma_y - \sin(\omega_q t)\sigma_x). \tag{2.24}$$

By expressing the drive pulse in the dipole approximation, valid for $\delta\omega = \omega_q - \omega_d \ll \omega_q + \omega_d$, we can drop fast rotating terms in Eq. 2.24. On the typical time scales of the phenomena into play, terms oscillating with frequency $\omega_q + \omega_d$ average out to zero (rotating wave approximation, or RWA). In the RWA we obtain:

$$\tilde{H}_d = \frac{1}{2}\Omega V_0 s(t)\left[(-I\cos(\delta\omega t) + Q\sin(\delta\omega t))\sigma_x + (I\sin(\delta\omega t) - Q\cos(\delta\omega t))\sigma_y\right], \tag{2.25}$$

or by using the definition in Eqs. 2.22 and 2.23:

$$\tilde{H}_d = -\frac{\Omega}{2} V_0 s(t) \begin{pmatrix} 0 & e^{i(\delta\omega t+\phi)} \\ e^{-i(\delta\omega t+\phi)} & 0 \end{pmatrix}. \tag{2.26}$$

When $\delta\omega = 0$, i.e. when the drive signals resonate with the qubit frequency, Eq. 2.26 becomes:

$$\tilde{H}_d = -\frac{\Omega}{2} V_0 s(t)(I\sigma_x + Q\sigma_y). \tag{2.27}$$

This shows that for an in-phase pulse ($\phi = 0$) the drive applies a rotation around the x-axis of the Bloch sphere, whereas for an out-of-phase pulse ($\phi = \frac{\pi}{2}$) it applies a rotation around the y-axis. Therefore, qubit drive can be performed by combining in-phase and out-of-phase pulses. In Section 3.4 we define how I and Q signals are generated by standard microwave electronics.

2.5.3 Rabi Oscillations of a two-level system

The dynamics of a two-level system exposed to a time-dependent drive field $\hat{H}$:

$$\hat{H}(t) = \frac{\hbar}{2} \begin{pmatrix} \omega_q & \omega_d e^{-i\omega t} \\ \omega_d e^{i\omega t} & -\omega_q \end{pmatrix}, \tag{2.28}$$

where ω is the frequency of the rotating frame, ω_q is the qubit transition frequency and ω_d is the frequency of the drive field, satisfies the Schrödinger equation:

$$i\hbar \frac{d\left|\psi(t)\right\rangle}{dt} = \hat{H}\left|\psi(t)\right\rangle, \tag{2.29}$$

where $\left|\psi(t)\right\rangle = a_1(t)\left|1\right\rangle + a_0(t)\left|0\right\rangle$, where $\left|0\right\rangle$ stands for the ground state and $\left|1\right\rangle$ for the excited state [20]. By moving into the rotating frame, the coefficients, the state and the Hamiltonian become:

$$b_1(t) = e^{\frac{i\omega t}{2}} a_1(t) \tag{2.30}$$

$$b_0(t) = e^{-\frac{i\omega t}{2}} a_0(t) \tag{2.31}$$

$$\left|\tilde{\psi}(t)\right\rangle \equiv b_1(t)\left|1\right\rangle + b_0(t)\left|0\right\rangle \tag{2.32}$$

$$\tilde{H} = \frac{\hbar}{2} \begin{pmatrix} -\delta\omega & \omega_d \\ \omega_d & \delta\omega \end{pmatrix}. \tag{2.33}$$

The dynamics of $\tilde{H}$ is still the same as that of $\hat{H}$ according to:

$$i\hbar \frac{d\left|\tilde{\psi}(t)\right\rangle}{dt} = \tilde{H}\left|\tilde{\psi}(t)\right\rangle \tag{2.34}$$

and through its diagonalization the time-dependent eigenstate is:

$$\left|\tilde{\psi}(t)\right\rangle = \cos\left(\frac{\theta}{2}\right) e^{\frac{it}{2}\sqrt{\delta\omega^2+\omega_d^2}}\left|\tilde{\psi}_-\right\rangle + \sin\left(\frac{\theta}{2}\right) e^{-\frac{it}{2}\sqrt{\delta\omega^2+\omega_d^2}}\left|\tilde{\psi}_+\right\rangle, \tag{2.35}$$

where

$$\left|\tilde{\psi}_+\right\rangle = \cos\frac{\theta}{2}\left|1\right\rangle + \sin\frac{\theta}{2}\left|0\right\rangle \tag{2.36}$$

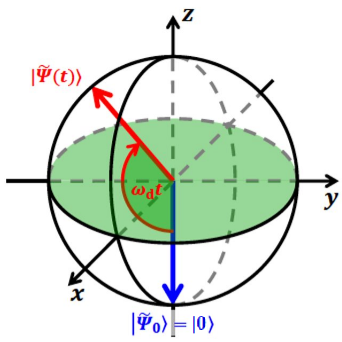

Figure 2.13: Bloch sphere representation of $|\tilde{\psi}(t)\rangle$ in presence of a perturbative field. The system is on-resonance with $\delta\omega = 0$, hence $\theta = \frac{\pi}{2}$ and at t=0 we find it in the $|0\rangle$ state, while at t we find it at $|\tilde{\psi}(t)\rangle$.

$$\left|\tilde{\psi}_{-}\right\rangle = -\sin\frac{\theta}{2}\left|1\right\rangle + \cos\frac{\theta}{2}\left|0\right\rangle \tag{2.37}$$

and θ is the angle of $|\tilde{\psi}_{+,-}\rangle$ in the laboratory frame from the z-axis (Figure 2.13), such that $\tan\theta = -\frac{\omega_d}{\delta\omega}$.

The probability that the two-level system is excited in $|1\rangle$ through the application of a drive field is:

$$P_1 \equiv \left|\langle 1|\psi(t)\rangle\right|^2 \equiv \left|\langle 1|\tilde{\psi}(t)\rangle\right|^2 = \frac{\omega_d^2}{\omega_d^2 + \delta\omega^2}\sin^2\left(\frac{t\sqrt{\delta\omega^2 + \omega_d^2}}{2}\right), \tag{2.38}$$

which means that the population of the two-level system oscillates with frequency $\Omega_r = \frac{\sqrt{\delta\omega^2+\omega_d^2}}{2}$, called *Rabi frequency* (Figure 2.14) [20].

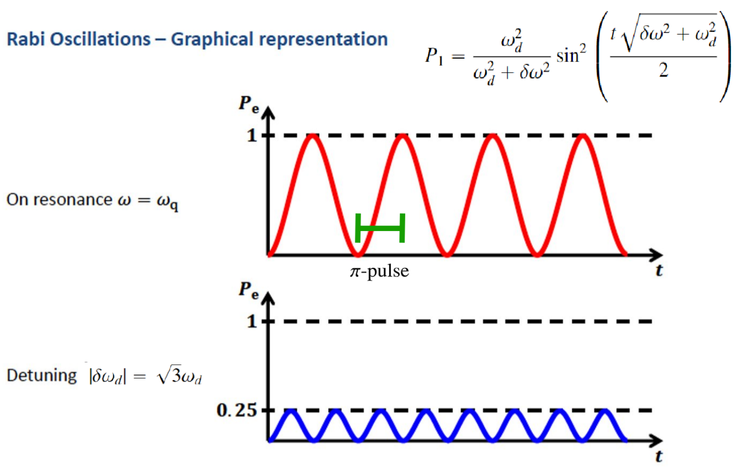

Figure 2.14: Simulation of Rabi oscillation of a two-level system for two different detunings $\delta\omega_d = 0$ (red curve) and $|\delta\omega_d| = \sqrt{3}\omega_d$ (blue curve). From the expression of P_1 in Eq. 2.38 we expect oscillations with decreased amplitude when the detuning increases. Moreover, the Rabi oscillation frequency increases when the detuning becomes larger.

From Eq. 2.38, it is possible to notice that when the detuning between the drive field and the qubit frequency is large, the amplitude of the oscillations reduces. On the contrary, when the detuning is small, the Rabi oscillation frequency increases (Figure 2.14). Therefore, driving the qubit with an oscillating field allows to identify when the drive frequency resonates with the qubit, i.e. when Rabi oscillations show maximum amplitude and minimum Rabi frequency. In this case, the half period of these oscillations represents the π-pulse, i.e. the pulse that sends the qubit from $|0\rangle$ to $|1\rangle$.

2.6 Relaxation and dephasing of qubits

As discussed in Section 2.1, qubits are sensitive to decoherence phenomena due to relaxation and dephasing when they are coupled to the environment. We can distinguish decoherence phenomena in: longitudinal relaxation, pure dephasing and transverse relaxation [4].

2.6.1 Longitudinal relaxation

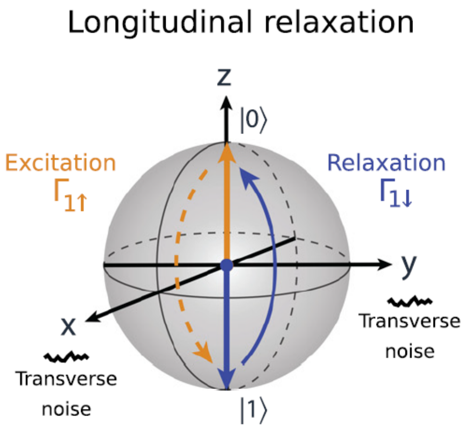

Figure 2.15: Graphical representation of longitudinal relaxation: the blue line represents the decay from $|1\rangle$ to $|0\rangle$ ($\Gamma_{1\downarrow}$) and the orange line represents the excitation from $|0\rangle$ to $|1\rangle$ ($\Gamma_{1\uparrow}$) due to the interaction with the environment. Figure adapted from [4].

When a qubit interacts with its environment, due to the transverse noise on the x-y plane, it is possible to observe transitions $|0\rangle \leftrightarrow |1\rangle$. The effects of such interactions are shown in Figure 2.15.

While in principle both relaxation and excitation are possible, superconducting qubits work at ultra-low temperatures, of the order of 10 mK, thus preventing excitations from the ground state to the first excited state. This will be discussed in more detail in Section 3.2. Therefore, the excitation rate $\Gamma_{1\uparrow}$ in Figure 2.15 can be neglected [4], i.e. the total relaxation rate corresponds to $\Gamma_1 \approx \Gamma_{1\downarrow}$.

This decay rate gives rise to the characteristic time $T_1 \equiv \frac{1}{\Gamma_1}$, which describes the time for which the qubit remains in $|1\rangle$ after being excited in that state. State-of-the-art transmon qubits are able to reach T_1 times in the range of tens of μs and even values of low hundreds of μs have been reported [4].

2.6.2 Pure dephasing

The *pure dephasing* rate Γ_φ, shown in Figure 2.16, describes depolarization in the x–y plane of the Bloch sphere. In the rotating frame, the Bloch vector appears stationary. Pure dephasing in the transverse plane arises from the longitudinal noise. Such longitudinal noise causes the qubit frequency ω_q to fluctuate, such that it is no longer equal to the

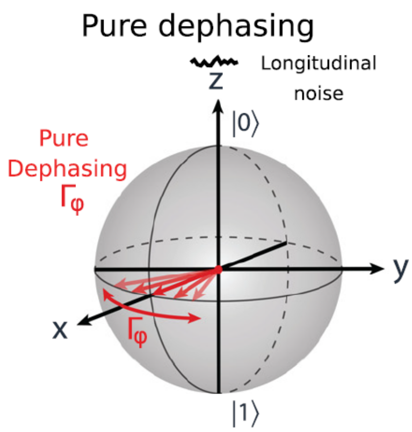

Figure 2.16: Graphical representation of pure dephasing on the equator of the Bloch sphere due to longitudinal noise. Figure adapted from [4].

rotating frame frequency ω_d, and causes the Bloch vector to precess forward or backward in the rotating frame. A Bloch vector along the x-axis will diffuse clockwise or counter-clockwise around the equator due to the stochastic frequency fluctuations, depolarizing the azimuthal phase with a rate Γ_φ. This eventually leads to a complete depolarization [4].

Comparing energy relaxation and pure dephasing, there are two main distinctions. Pure dephasing is not a resonant phenomenon. It is affected by a broad range of frequencies that change the frequency of the qubit [4]. Moreover, pure dephasing is elastic, which means that there is no energy exchange with the environment [4]. As a consequence, it can be inverted through a unitary operation [4].

2.6.3 Transverse relaxation

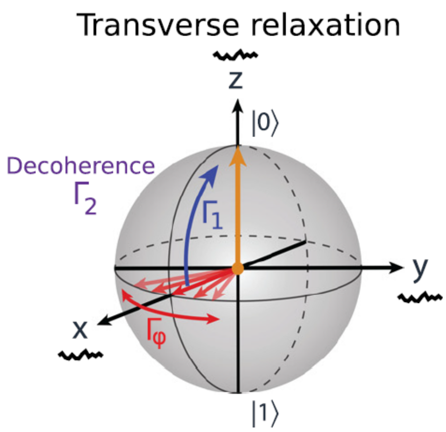

Figure 2.17: Graphical representation of transverse relaxation: in red, the dephasing and in blue the energy relaxation processes due to longitudinal and transverse noise sources, respectively. Figure adapted from [4].

The *transverse relaxation* rate describes the loss of coherence of a superposition state (Figure 2.17), and reads as [4]:

$$\Gamma_2 = \frac{\Gamma_1}{2} + \Gamma_\varphi \tag{2.39}$$

In this case there are both pure dephasing processes due to longitudinal noise and energy relaxation processes due to transverse noise. Such relaxation processes can break the phase, because it makes the Bloch vector point to the north pole $|0\rangle$, thus losing all information about the direction in which the vector had been pointing along the equator. The relative phase of the superposition state is lost.

From Γ_2 one derives $T_2 \equiv \frac{1}{\Gamma_2}$. The typical T_2 times for superconducting qubits are in the range of the tens or low hundreds of μs and are limited by the relaxation time T_1 [9]. The best that one can get, for ideal $\Gamma_\varphi = 0$, is $T_2 = 2T_1$.

2.7 Flux tunability of superconducting qubits

In this thesis, a special focus will be given to *split transmons*, which is a particular type of transmon with a DC-SQUID instead of a single JJ, as reported in Figure 2.18. SQUID stands for *Superconducting Quantum Interference Device* and it introduces a further degree of freedom (external flux) into the transmon. The DC SQUID is made of a superconducting ring with two JJs and it allows to tune the frequency of the qubit, like in the insets of Figure 2.18. The qubit frequency depends on the Josephson energy E_J as [9]:

$$\omega_q = \sqrt{8E_C E_J \left|\cos\left(\frac{\pi\Phi}{\Phi_0}\right)\right|}. \tag{2.40}$$

The external flux allows to tune the Josephson energy, hence the frequency of the qubit, as shown in Figure 2.18. The current flowing in a symmetric DC SQUID (the two JJs have equal critical currents) is [21]:

$$I_s = I_{s1} + I_{s2} = I_C \sin\varphi_1 + I_C \sin\varphi_2 = 2I_C \cos\left(\frac{\varphi_1 - \varphi_2}{2}\right) \sin\left(\frac{\varphi_1 + \varphi_2}{2}\right), \tag{2.41}$$

with $I_{s1,2}$ the superconducting currents across the two JJs, I_C the critical current of both JJs and $\varphi_{1,2}$ the phase across the two JJs. The phase difference $\varphi_2 - \varphi_1$ is not independent and it is bound to the flux quantization:

$$\oint_\Gamma \vec{\nabla}\varphi \cdot d\vec{l} = 2\pi n, \tag{2.42}$$

with φ the phase variable and Γ the closed circuit of the DC SQUID over which the linear integral is done. This provides the expression for the phase difference:

$$\varphi_2 - \varphi_1 = \frac{2\pi\Phi_{ext}}{\Phi_0}, \tag{2.43}$$

with Φ_{ext} the external flux.

The possibility to tune the qubit frequency by means of an external knob, such as the flux, opens up the possibility to provide a useful and practical way to control and manipulate the qubit. However, it also introduces novel noise sources that may affect its performance. In order to tackle this problem, the research community has focused its interest in the implementation of asymmetric DC-SQUID, i.e. when the two JJs in the loop are fabricated with different critical currents compared to symmetric DC-SQUID. The impact of symmetric and asymmetric SQUIDs, where the asymmetry parameter is $d = \frac{\gamma-1}{\gamma+1}$ with

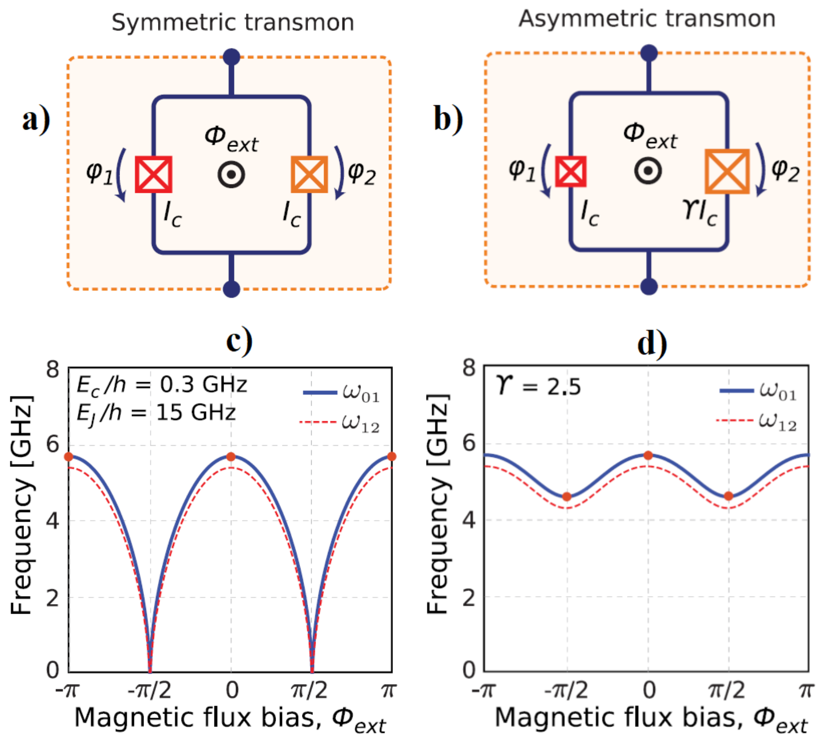

Figure 2.18: Flux dependence of the qubit frequency transitions ω_{01} and ω_{12} in the case of symmetric and asymmetric transmons [4]. In **a)** Schematics of a symmetric split-transmon with I_c critical current of the Josephson junctions in the SQUID; in **b)** schematics of an asymmetric split-transmon, with γ the scaling factor for the critical current of one of the two Josephson junctions; in **c)** and **d)** ω_{01} (blue curve) and ω_{12} (red dashed curve) as a function of the external magnetic flux field Φ_{ext} for a symmetric and an asymmetric split-transmon, respectively, with E_J, E_C and γ defined in the legends. Red dots identify the transmon sweet-spots. Figure adapted from [4].

$\gamma = \frac{E_{J2}}{E_{J1}}$, is shown in Figures 2.18c. The variation of E_J in the asymmetric case is much lower when compared to the symmetric case. The derivation for the Hamiltonian of the asymmetric transmon gives the following expression [4]:

$$H = 4E_C n^2 - \underbrace{E_{J\Sigma}\sqrt{cos^2(\varphi_e) + d^2 sin^2(\varphi_e)}}_{E'_J(\varphi_e)} cos(\phi), \tag{2.44}$$

where $\varphi_e = \frac{\pi\Phi_{ext}}{\Phi_0}$ and $E_{J\Sigma} = E_{J1} + E_{J2}$. The interaction Hamiltonian with the environment provides the way to quantify the noise affecting the system:

$$\hat{H}_{int} = v\hat{O}_q\hat{\lambda}, \tag{2.45}$$

where $\hat{O}_q$ represents the qubit degrees of freedom and $\hat{\lambda}$ the noise source.

It is possible to show that the transitions between qubit eigenstates due to the external noise follow an exponential decay law [4]. Therefore, it is possible to find Γ_1:

$$\Gamma_1 = \frac{1}{\hbar^2}\left|\langle 0|\frac{\partial \hat{H}_q}{\partial \lambda}|1\rangle\right|^2 S_\lambda(\omega_q). \tag{2.46}$$

$S_\lambda(\omega_q)$ is the corresponding noise spectral density [4]. It is possible to reduce Γ_1 to zero when $\frac{\partial \hat{H}_q}{\partial \lambda} = 0$. When this occurs, the system is in the *sweet spot* with respect to λ.

In case of flux-tunable transmon, there are flux sweet spots in both the symmetric and asymmetric cases, which correspond to the maxima or minima of the Josephson potential in Eq. 2.44. While in both cases it is possible to sit on a sweet spot, fluctuations may move the qubits away from the sweet spots and may cause flux noise [4]. In the asymmetric case, the behavior of the qubit frequency as a function of magnetic flux is smoother than the symmetric one, therefore fluctuations from sweet spots induce lower noise levels when compared to the symmetric case [22].

2.8 Single qubit gates, fidelity and Randomized Benchmarking

Superconducting transmon qubits have been proposed as the building block of gate-based quantum processors [13], [23], [24]. A gate-based quantum computer is a device able to perform quantum algorithms, which are typically schematized as a set of unitary operations, namely *quantum gates*, applied on an initial input quantum state, followed by a measurement of the output quantum state [25]. As stated in Section 2.1, in order to build a quantum computer, it is fundamental to search for a device able to implement universal gate sets, i.e. a sequence of gates and measurements able to perform generic operation. An example of possible quantum algorithms are reported in [26], [27], [28]. A universal gate set can be made with just single- and two-qubits gates.

Single-qubit gates move an arbitrary quantum state from one point on the Bloch sphere to another point by rotating the qubit state vector by a certain angle and around a particular axis. Conventionally, the computational basis is the eigenbasis of the σ_z operator.

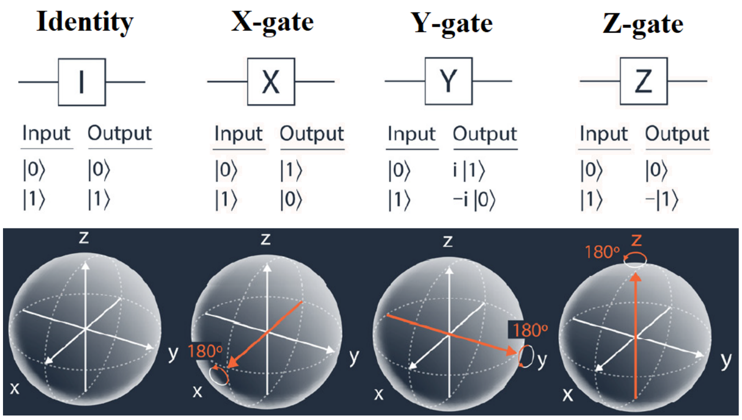

Figure 2.19: Single-qubit gates: in the first row quantum circuit representation of single-qubit gates; in the second and third row action of gates on the ground state $|0\rangle$ and the excited state $|1\rangle$ and representation on the Bloch sphere, respectively. Figure adapted from [4].

A convenient way to visualize single qubit gates is the quantum circuit representation in Figure 2.19. We define the most basic qubit gates involving single qubits in terms of their quantum circuit representation: the identity gate I, which gives in return the initial state, and the X, Y and Z gates. The last correspond to rotation of the quantum state around the x-, y- and z-axes of the Bloch sphere, respectively. As a matter of fact, the I, X, Y and Z gates correspond to the Pauli matrices σ_0, σ_x, σ_y and σ_z, respectively:

$$I = \begin{pmatrix} 1 & 0 \\ 0 & 1 \end{pmatrix} \qquad X = \begin{pmatrix} 0 & 1 \\ 1 & 0 \end{pmatrix} \qquad Y = \begin{pmatrix} 0 & -i \\ i & 0 \end{pmatrix} \qquad Z = \begin{pmatrix} 1 & 0 \\ 0 & -1 \end{pmatrix}. \tag{2.47}$$

Since Pauli matrices are unitary, they are also reversible, i.e. applying a gate and its opposite should result in the state vector returning to its original form [4].

The evaluation of the performance of the single-qubit gates is a key study in the implementation of superconducting quantum processor. Even though single qubit gates in Figure 2.19 fulfill mathematically the request of unitarity, quantumness and universality of the gate set, the physical realization on a realistic quantum hardware is one of the most challenging goals. This is particularly relevant for superconducting quantum processors, in which the strong sensitivity to the environmental condition and the unavoidable interaction between the user and the system may cause strong deviation on the outcomes of a single-qubit gate from theoretical expectations. Moreover, related to the problem of measurement in Quantum Mechanics, the state of a quantum system is represented by a state vector $|\psi\rangle$ on the Bloch sphere only in the scenario of pure states. Quantum states in physical applications are more likely to be a statistical ensemble of different state vectors, also known as mixed states. While pure states are represented as vectors pointing on the surface of the Bloch Sphere, mixed states fall inside the sphere. The scientific community introduced a mathematical and physical way to quantify the quality of the qubit performances by means of the state and the gate fidelity [29].

The state fidelity measures the distinguishability of two quantum states, ρ and σ, where ρ is the experimental quantum state density matrix and σ is its theoretical expectation. This is defined as:

$$F(\rho,\sigma) = Tr\left[\sqrt{\sqrt{\rho}\sigma\sqrt{\rho}}\right]^2, \tag{2.48}$$

i.e. it measures the deviation of an experimental quantum state from the theoretical expectation. If $\rho = |\psi\rangle\langle\psi|$ and $\sigma = |\phi\rangle\langle\phi|$ are both pure states, then $F(|\psi\rangle\langle\psi|, |\phi\rangle\langle\phi|) = \left|\langle\psi|\phi\rangle\right|^2$ becomes the standard definition of quantum probability. More importantly, if the state $|\phi\rangle$ exactly corresponds to $|\psi\rangle$, the fidelity approaches the limit value of 1, i.e. if the quantum system is prepared exactly in the state $|\phi\rangle$ we measure the state $|\phi\rangle$ with 100 % probability.

The definition of state fidelity can be extended to a definition of *gate fidelity*:

$$\mathcal{F}(\hat{U}, \hat{\Lambda}_U) = \int d\rho F(U\rho U^\dagger, \hat{\Lambda}_U(\rho)). \tag{2.49}$$

Here U represents an ideal unitary gate, with $U^\dagger$ its adjoint, whereas $\hat{\Lambda}_U$ is the imperfect realization of such gate. Eq. 2.49 describes the fidelity between the result of the ideal operation and the result of the actual operation averaged over all pure-state density matrices [29]. For a pure state $\rho = |\psi\rangle\langle\psi|$, the integrand in the gate fidelity can be simplified to:

$$F(U\rho U^\dagger, \hat{\Lambda}_U(\rho)) = \langle\psi|U^\dagger\hat{\Lambda}_U(|\psi\rangle\langle\psi|)U|\psi\rangle. \tag{2.50}$$

Finally, if the gate $\hat{\Lambda}_U(\rho)$ is also unitary and exactly implements U, $\hat{\Lambda}_U(\rho) = U\rho U^\dagger$, Eq. 2.50 reduces to 1. This means that we obtain the maximum probability to have the same outcomes of the application of a unitary gate on the quantum state.

As one can notice in Eq. 2.50, the gate fidelity is given by a projection and averaging over all pure states $|\psi\rangle$. Since averaging over all pure states is not experimentally possible [29], a possible solution is given by *Randomized Benchmarking* (RB).

The RB procedure produces an average gate fidelity over a set of randomly chosen gates. A benefit of this approach is that, similarly to Monte Carlo algorithms, the randomized approach allows to get a fast convergence rate of the fidelity integral. RB does not focus on a particular gate, hence it provides an aggregate fidelity. The disadvantages are directly related to the random procedures used in the measurement [29]. Since RB does not focus on any particular gate, it only quantifies how well we are able to control the qubits. As a consequence, these results cannot be directly applied to improve the single operations in the RB protocol. For example, the single-qubit RB protocol uses gates that include the Z-gate, which corresponds to a π-shift on the Bloch sphere around the z-axis, but we cannot use the RB result directly to improve the parameters of the Z-gate.

The randomly chosen gates applied in the RB fidelity test fall in the category of the so called Clifford gates [30]. It tests the concatenation of many operations (hundreds of operations) applied on a qubit system and is more representative of real life algorithms. Clifford gates are generated by $C_i = e^{\pm i\sigma_u \frac{\pi}{4}}$ with $u = x, y$, where σ_x and σ_y correspond to single-qubit gates reported in Eq. 3.1. The complete set of single-qubit Clifford gates is $\left\{I, \pm X_\pi, \pm Y_\pi, \pm Z_\pi, \pm X_{\frac{\pi}{2}}, \pm Y_{\frac{\pi}{2}}, \pm Z_{\frac{\pi}{2}}\right\}$ [31].

The general protocol for RB is:

1. Initialize the system in the ground state;
2. Apply a series of random Clifford gates, in the pattern $\prod_i C_i Pi$ with C_i the Clifford gate generator and P_i the Pauli rotations, i.e. I, X, Y and Z;
3. Apply the inverse Clifford or Pauli pulse to return to an eigenstate of Z, which should in theory be the initial state, i.e. the ground state;
4. Perform repeated measurements of Z and compare with theory to obtain the fidelity;

We expect that after the RB test, if there has not been any error, the system will return to its initial state. The gathered data is called the *survival probability*, measured by varying the number of applied Clifford gates. Experimentally, one can notice that the fidelity instead recovers an exponential decay of the type:

$$F_N = (1 - \alpha_n) + \alpha_n \left(1 - \frac{\epsilon_m}{\alpha_n}\right)\left(1 - \frac{\epsilon_s}{\alpha_n}\right)^N, \tag{2.51}$$

where $\alpha_n = \frac{2^n - 1}{2^n}$ gives the dimensionality of the n-qubit system and N is the length of the Clifford sequence used. The term $\left(1 - \frac{\epsilon_s}{\alpha_n}\right)$ is related to what are known as polarizing errors ϵ_s and they appear when the Clifford gate and its inverse do not return the qubit to its initial state. $\left(1 - \frac{\epsilon_m}{\alpha_n}\right)$ represents *state preparation and measurement* (SPAM) errors [29]. SPAM errors with ϵ_m are related to errors in the preparation of the initial state and to errors in the measurement of the final state. Therefore, the measurement of the gate fidelity allows to get information on the quality of the gate implemented on the actual hardware. In other words, fidelity test provides a measure of how often the system actually returns in the initial state after the sequence (survival probability), as a function of the number of Clifford gates applied related to the quality of the gates themselves.

The fidelity is not only related to the electronics and the sequence applied, but it is also intrinsically related to the quality of the qubit itself. In particular, an estimate of the maximum fidelity achievable in a qubit is strongly dependent on the coherence of the qubit and the dephasing due to the phenomena explained in Section 2.6. The fidelity for a system of N coupled qubits is [32]:

$$\bar{F}_N = 1 - \frac{d}{2(d+1)}\tau \sum_{k=1}^{N}(\Gamma_1^k + \Gamma_\varphi^k), \tag{2.52}$$

where $d = 2^N$ and Γ_1 and Γ_φ are the characteristic rates of the qubit, described in Section 2.6. τ is the mean duration of the gate. In the case of the single-qubit Clifford sequence, we expect a τ in the hundreds of nanoseconds [32].

Even though the performance of a single qubit is of immeasurable importance towards the implementation of quantum algorithms, it is not possible to build a universal gate set with just single-qubit gates. Quantum algorithms require at least the possibility to achieve high-fidelity (F>99 %) two-qubit gates [10]. In order to build such operations, it is fundamental to understand how we can couple two or more qubits in superconducting quantum processors. In the following, we will report the most common circuital approaches to build coupled quantum systems, as those discussed in this thesis.

2.9 Coupling of two superconducting transmons

In literature, coupling between superconducting qubits can be achieved by means of several coupling schemes: via direct capacitive coupling, via direct inductive coupling, via a capacitively coupled resonator or via another qubit [4], which are all shown in Figure 2.20. We will focus on two transmon qubits capacitively coupled through a high-frequency resonator coupler. The Hamiltonian of two coupled systems takes the generic form:

$$H = H_1 + H_2 + H_{int}, \tag{2.53}$$

with H_1 and H_2 the Hamiltonians of the two qubits and H_{int} is the interaction Hamiltonian between the two qubits.

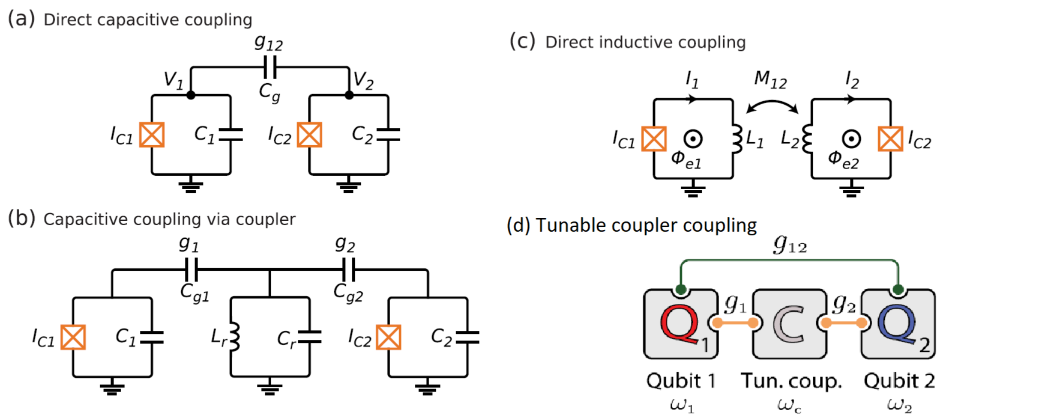

Figure 2.20: Circuital schematics of two-qubit coupling: **a)** direct capacitive coupling; **b)** capacitive coupling mediated by a linear resonator coupler; **c)** direct inductive coupling; **d)** two-qubit coupling mediated by a frequency-tunable coupler. **a)**, **b)**, **c)** are adapted from [4] and **d)** is adapted from [33].

In this thesis we will operate the system in the dispersive regime and the qubits are far detuned from the coupling resonators $\left(\left|\Delta_{1,2}\right| = \left|\omega_{q1,q2} - \omega_r\right| \gg g_{1,2}\right)$. In this limit it is possible to apply the second-order perturbation theory and the system is described by the following effective Hamiltonian [34]:

$$H_{eff} = \frac{\omega_{q1}}{2}\sigma_1^z + \frac{\omega_{q2}}{2}\sigma_2^z + (\omega_r + \chi_1\sigma_1^z + \chi_2\sigma_2^z)a^\dagger a + J(\sigma_1^-\sigma_2^+ + \sigma_1^+\sigma_2^-), \tag{2.54}$$

where $\omega_{q1,q2}$ are the frequencies of the two coupled qubits, ω_r is the resonance frequency of the coupling resonator and $\chi_{1,2}$ are the dispersive shifts of the resonator due to the coupling with the qubits, where $\chi_{1,2} = \frac{g_{1,2}^2}{\Delta_{1,2}}$ with $g_{1,2} \approx e\sqrt{\frac{\omega_r}{C_r}}\frac{C_{g1,g2}}{C_B+C_{J1,J2}+C_{g1,g2}}\left(\frac{E_{J1,J2}}{E_{C1,C2}}\right)^{\frac{1}{4}}$ [9]. The J in Eq. 2.54 is the coupling between the two qubits mediated by the coupling resonator. This is a transverse interaction and has the form [34]:

$$J = g_1 g_2 \frac{\Delta_1 + \Delta_2}{2\Delta_1\Delta_2}, \tag{2.55}$$

where $\Delta_{1,2} = \omega_{q1,q2} - \omega_r$. The qubit-qubit interaction is due to the virtual exchange of photons with the coupling resonator. Eq. 2.54 describes the interaction between two two-level systems. When $\Delta_{12} = \omega_{q1} - \omega_{q2}$ is comparable to J, this causes an *avoided level crossing* [34]. In order to experimentally achieve the avoided level crossing, we tune one of the qubits into resonance with the other through an external flux.

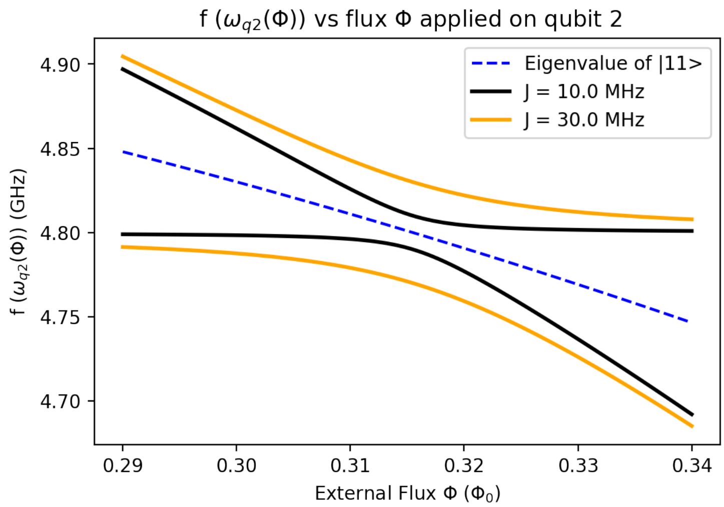

Figure 2.21: Theoretical simulation of the avoided level crossing for two two-level systems, qubit 1 and qubit 2, as a function of the external flux Φ applied on qubit 2, according to Eq. 2.56, for J=10 MHz (black curve) and 30 MHz (orange curve). The blue dashed line represents the eigenvalue of the $|11\rangle$ state, which is the reference level.

The Hamiltonian in Eq. 2.54 can be represented in matrix form and it is a 4×4 matrix. As reported in Appendix B, its diagonalization leads to [35]:

$$f(\omega_{q2}) = \frac{\omega_{q1} + \omega_{q2}}{2} \pm \frac{\sqrt{(\omega_{q2} - \omega_{q1})^2 + 4J^2}}{2}, \tag{2.56}$$

where ω_{q1} is the frequency of the fixed low-frequency qubit and $\omega_{q2} = \omega_{q2}^{(0)}\sqrt{\left|\cos\left(\frac{\pi\Phi}{\Phi_0}\right)\right|}$ is the frequency of the tunable high-frequency qubit. The two coupled qubits have the new eigenbasis:

$$\left\{|00\rangle,\ |\psi_s\rangle = \frac{1}{\sqrt{2}}(|01\rangle + |10\rangle),\ |11\rangle,\ |\psi_a\rangle = \frac{1}{\sqrt{2}}(|01\rangle - |10\rangle)\right\}. \tag{2.57}$$

For large qubit-qubit detuning, the two two-level systems realize asymptotically $|01\rangle$ and $|10\rangle$ as: $|\psi_a\rangle \to |10\rangle$ and $|\psi_s\rangle \to |01\rangle$. When the qubit-qubit detuning decreases, the entangled states $|\psi_s\rangle = \frac{1}{\sqrt{2}}(|01\rangle + |10\rangle)$ and $|\psi_a\rangle = \frac{1}{\sqrt{2}}(|01\rangle - |10\rangle)$ are realized. By using Eq. 2.56 and the flux dependence of qubit 2, we can predict the avoided level crossing, as shown in Figure 2.21.

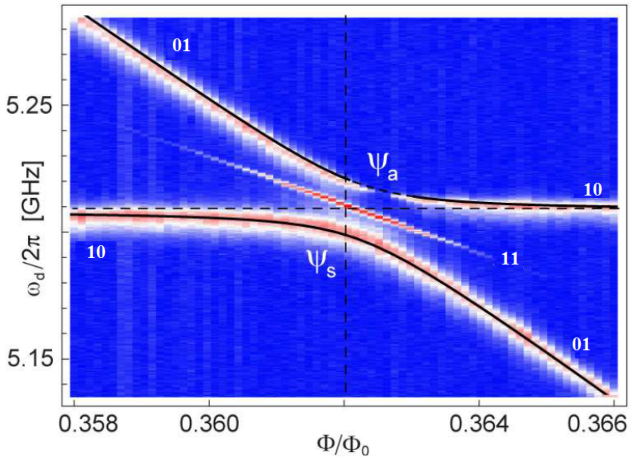

Figure 2.22: Spectroscopic measurement of the avoided level crossing as function of normalized flux $\frac{\Phi}{\Phi_0}$ threading the first qubit loop with the second qubit at a fixed frequency. The solid lines indicate energy levels calculated from a diagonalization of the two-qubit Jaynes-Cummings Hamiltonian. Figure adapted from [35].

An experimental example of this behaviour with transmons is shown in Figure 2.22, where there is a straight line in the middle of the avoided level crossing. This does not always occur and it is only expected when the drive power is high enough to induce two-photon transitions from $|00\rangle$ to $|11\rangle$ and it is only allowed directly at the avoided level crossing. The possibility to establish an avoided level crossing between two qubits is fundamental for the implementation of multi-qubit gates. As a matter of fact, it establishes a finite exchange of energy between the two resonant qubits.

2.10 The iSWAP two-qubit gate

There are more than one universal gate sets [4], because some gate sets are easier to implement on certain types of qubits than others. The feasibility of the gate depends on how easy it is to implement on the particular hardware. Such gates are called *native gates* and they are typically the gates for which the Hamiltonian governing the gate implementation gives rise to a unitary propagator that corresponds to the gate itself. Among all the possible two-qubit gates achievable for capacitively coupled qubits, we will focus our attention on the iSWAP [4].

The iSWAP gate swaps an excitation between the two qubits and adds a phase $i = e^{i\frac{\pi}{2}}$. The unitary matrix which describes this gate is:

$$U_{iSWAP} = \begin{bmatrix} 1 & 0 & 0 & 0 \\ 0 & 0 & -i & 0 \\ 0 & -i & 0 & 0 \\ 0 & 0 & 0 & 1 \end{bmatrix}. \tag{2.58}$$

The interaction term of the Hamiltonian in Eq. 2.54 is the key to understand how we perform a two-qubit gate, in particular the iSWAP gate. For simplicity, we can consider a direct capacitive coupling between the two qubits, instead of the resonator mediated coupling [4]. This allows us to rewrite the coupling J between the two qubits as:

$$J \rightarrow J_{q-q} = \frac{1}{2}\sqrt{\omega_{q1}\omega_{q2}}\frac{C_{q-q}}{\sqrt{C_{q-q}+C_{J1}}\sqrt{C_{q-q}+C_{J2}}}, \tag{2.59}$$

where C_{q-q} is the qubit-qubit coupling capacitance and C_{Ji} is the capacitance of qubit i. For simplicity, we suppress the explicit flux dependence of the ω_{q_i} and simply refer to the coupling as J [4]. The interaction part of the Hamiltonian in Eq. 2.54 becomes [4]:

$$H_{qq} = J\left(\sigma_1^-\sigma_2^+ + \sigma_1^+\sigma_2^-\right) = \frac{J}{2}(\sigma_x\sigma_x + \sigma_y\sigma_y). \tag{2.60}$$

The first term of Eq. 2.60 shows that a capacitive interaction leads to a swapping of excitations between the two qubits, i.e. the iSWAP [4]. As a matter of fact, the unitary operator corresponding to this interaction is:

$$U_{qq}(t) = e^{-i\frac{J}{2}(\sigma_x\sigma_x+\sigma_y\sigma_y)t} = \begin{bmatrix} 1 & 0 & 0 & 0 \\ 0 & \cos(Jt) & -i\sin(Jt) & 0 \\ 0 & -i\sin(Jt) & \cos(Jt) & 0 \\ 0 & 0 & 0 & 1 \end{bmatrix}, \tag{2.61}$$

where the time duration for the swap exchange energy is related to the coupling energy as $t' = \frac{\pi}{2J}$. Thus, we recover the unitary matrix in Eq. 2.58.

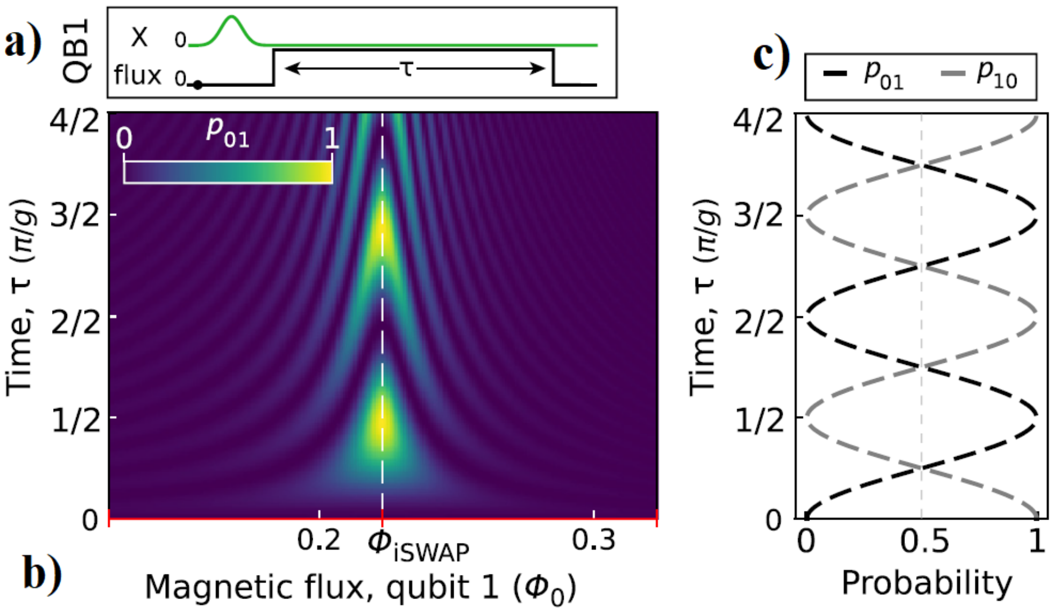

Figure 2.23: iSWAP gate experiment adapted from [4]: **a)** Pulse sequence to put the two-qubit system in the $|10\rangle$ state (green line) and the flux pulse used to put the two qubits into resonance (black line). The flux pulse is applied to one of the two qubits, which is usually the one with higher transition frequency, in this case (QB1), for a duration τ. **b)** Probability p_{01} to find the system in $|01\rangle$ as a function of the amplitude of the magnetic flux and the flux pulse duration τ. In **c)** line-cut of panel **b)** at magnetic flux Φ_{iSWAP} (black dashed curve), compared with the probability to be in the state $|10\rangle$, p_{10} (grey dashed line).

In order to perform an iSWAP experiment, we need to tune into resonance the two qubits.

First we need to excite one of the qubits, for example qubit 1, such that the system is in the $|10\rangle$ state, as shown in Figure 2.23a. Since we want to mitigate possible flux noise, we operate the qubits at their sweet spot. In this example, this means that we tune qubit 1 because it has the higher sweet spot transition frequency. We leave qubit 2 at its sweet spot and we apply the flux pulse on qubit 1 to make the two qubits resonant. However, in order to observe the swap of energy typical of the iSWAP, in accordance with Eq. 2.58, we need to apply the flux pulse for at least $t' = \frac{\pi}{2J}$. By varying the amplitude and duration of the flux pulse on qubit 1 it is possible to measure the probability for the system to be in the $|01\rangle$ state, as shown in Figure 2.23b. From Figure 2.23c we can observe the swap of energy between the two qubits, in fact, when qubit 1 goes from state $|1\rangle$ to $|0\rangle$, qubit 2 goes state $|0\rangle$ to $|1\rangle$. In order to have a good iSWAP gate, it needs to be fast, so the time t' must be as low as possible. This is achieved by having very high coupling J between the two qubits. If the coupling is too weak, the gates will be too slow for any practical applications.

The iSWAP gate is a fundamental two-qubit gate, since it can provide a universal gate set for a quantum processor together with specific single-qubit gates. Therefore, it is one of the most used in literature. An example of universal gate set containing the iSWAP in some form is [36]:

$$G = \{Z_{-\frac{\pi}{2}}, H, \sqrt{iSWAP}\}, \tag{2.62}$$

where H is the Hadamard gate represented by the following unitary matrix:

$$H = \frac{1}{\sqrt{2}} \begin{pmatrix} 1 & 1 \\ 1 & -1 \end{pmatrix}. \tag{2.63}$$

As shown in Eq. 2.61, by tuning the capacitive coupling between the qubits for a time t', we obtain the iSWAP gate. If we tune the coupling for a time $t'' = \frac{\pi}{4J}$, we obtain:

$$U_{qq}\left(\frac{\pi}{4J}\right) = \begin{bmatrix} 1 & 0 & 0 & 0 \\ 0 & \frac{1}{\sqrt{2}} & -\frac{i}{\sqrt{2}} & 0 \\ 0 & -\frac{i}{\sqrt{2}} & \frac{1}{\sqrt{2}} & 0 \\ 0 & 0 & 0 & 1 \end{bmatrix} \equiv \sqrt{\mathbf{iSWAP}}, \tag{2.64}$$

The $\sqrt{iSWAP}$ gate, which is typically referred to as *squareroot-iSWAP* gate, can be used to generate Bell-like superposition states, for example $|01\rangle + i\,|10\rangle$ [4].

Another very common gate that uses the iSWAP is the CNOT [4]. This gate uses the first qubit as for control and the second qubit as the target. The CNOT can be obtained from the iSWAP as follows:

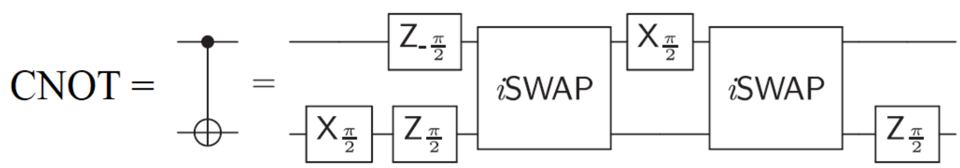

. (2.65)

3 Experimental set-up and qubit measurements

Transmon qubit characterization requires both cryogenic systems in order to reach temperatures of 10 mK and microwave cryogenic and room temperature electronics to control and read the qubit state. In Section 3.1 we will show the chip design based on transmon qubits. In Section 3.2, we will describe the cooling procedure of the dilution refrigerator used in this work. In Section 3.3, we will describe the cryogenic and room-temperature electronics. In Sections 3.4 and 3.5 we will discuss time-domain and spectroscopic measurements, for basic and advanced characterizations of superconducting qubits.

3.1 Transmon chip

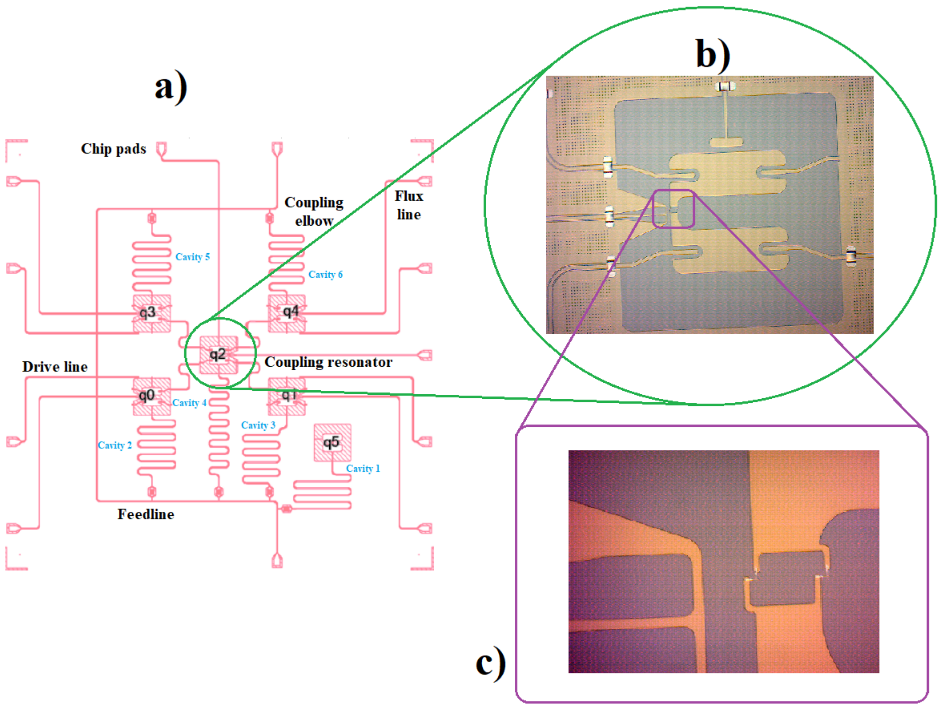

Figure 3.1: a) Layout of the chip fabricated by QuantWare. The chip contains a feedline, to which 6 readout resonators are coupled by means of an elbow geometry. The five coupled qubits have a Qubit Drive line and a Flux line. The qubit-qubit coupling through qubit 2 is realized through a coupling resonator. **b)** SEM image of qubit 2 and all the lines that couple to it. **c)** SEM image of the DC SQUID in the qubits. Images **b)** and **c)** are courtesy of the Seeqc quarters in London, UK.

The transmon chip measured and characterized in this master thesis is realized by QuantWare, spin-off company of the University of Delft, within the framework of a collaboration with the University of Napoli Federico II and Seeqc-EU company. The Josephson junctions are composed of aluminum electrodes and AlO_x barrier, while the other components of the circuits are made of niobium-titanium nitride. There are six floating qubits [37], five of which (qubits 0 to 4) are coupled and the last one (qubit 5) is a single isolated qubit. The chip layout is shown in Figure 3.1. While qubit 0 and qubit 1 have the lowest frequency on chip, qubit 3 and qubit 4 have the highest frequency. Qubit 2, which is coupled to all the qubits, has a medium frequency (see Table 1 for further details). This design is suitable for advanced quantum error detection and correction [6], [28], [38].

Qubits 0 to 4 are coupled to a flux line, a drive line and the outer qubits (0, 1, 3, 4) are coupled to the central qubit (2) through high-frequency bus resonators (Figure 3.1b), which we refer to as coupling resonators, as we have discussed in Section 2.9.

The six readout resonators have been designed in such a way that the corresponding resonator frequency increases with the number of the label (except for cavity number 1 coupled to qubit 5, which has the lowest resonance frequency). The designed values of the resonance frequency are reported in the Table 1. This design choice allows to separate the cavities so that their resonance frequencies do not overlap.

Cavity 1 – Q5	**Cavity 2 – Q0**	**Cavity 3 – Q1**	**Cavity 4 – Q2**	**Cavity 5 – Q3**	**Cavity 6 – Q4**
7.00 GHz	7.20 GHz	7.40 GHz	7.60 GHz	7.80 GHz	8.00 GHz
Q5	**Q0**	**Q1**	**Q2**	**Q3**	**Q4**
4.70 GHz	4.70 GHz	4.70 GHz	5.60 GHz	6.50 GHz	6.50 GHz
$^{E_J}/_{E_C}$ of Q5	**$^{E_J}/_{E_C}$ of Q0**	**$^{E_J}/_{E_C}$ of Q1**	**$^{E_J}/_{E_C}$ of Q2**	**$^{E_J}/_{E_C}$ of Q3**	**$^{E_J}/_{E_C}$ of Q4**
42	42	59	79	79	42

Table 1: Resonance frequencies of the coupling resonators, of the qubits and $\frac{E_J}{E_C}$ ratios of the qubits in Figure 3.1a.

We will give particular attention to qubits 0 and 2, which as the other qubits on the chip are of the split-transmon type. The junctions in the DC SQUIDs of these qubits are made to be symmetric, which would allow for large variation in the qubit frequencies, as detailed in Section 2.7. A SEM image of the DC-SQUID is provided in Figure 3.1c. Furthermore, the charging energy E_C and the Josephson energy E_J are engineered so that we are able to work in the $\frac{E_J}{E_C} \gg 1$ regime. This is achieved through the use of a large shunting capacitance, as discussed in Section 2.5. Expected readout resonator frequencies and ratios $\frac{E_J}{E_C}$ are reported in Table 1.

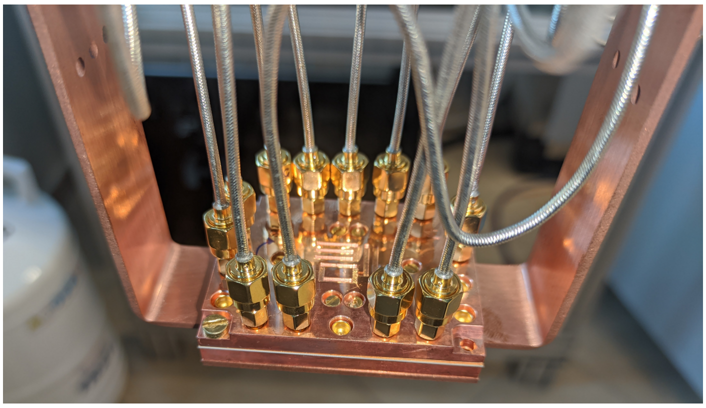

Figure 3.2: Chip package mounted on the Mixing Chamber of the cryostat and microwave lines connected to the external electronics.

The readout resonators, as described in Section 2.5.1, are used to read the qubit state without destroying it. The resonators are used to measure the state of the qubit and are operated in the dispersive regime. The electrical signals used for the readout are in the microwave regime. The resonators are coupled to the feedline and this configuration allows for multiplexing, i.e. to address multiple resonators with the single feedline by sending signals with different frequencies. All these lines receive their signal from the chip pads, which are connected to the external control electronics as shown in Figure 3.2. Every single connection to the package corresponds to a microwave line connected to the external electronics.

The RF lines designed and realized on the chip are all Coplanar Waveguide (CPW) and they use Transverse Electromagnetic Modes (TEM). The CPWs can be engineered in such a way that we can maximize the magnetic or the electric field of the TEM signal. This is useful because in some cases we need a microwave electric field (qubit drive or readout), and in other cases we need a magnetic field (flux biasing of the DC SQUID).

In order to maximize the electric field of the TEM modes necessary for driving the qubit on the Bloch sphere, the drive lines are capacitively coupled to the qubit, as shown in Figure 2.12. Similarly, the resonators are capacitively coupled, as shown in Figure 2.9, to the qubits in order to perform quantum non demolitive measurements, as discussed in Section 2.5.1. The flux lines are inductively coupled to the DC-SQUID of the transmon, to apply an external magnetic flux which tunes the qubit frequency, as discussed in Section 2.7. The resonators are coupled to the feedline through *elbow couplings* and the coupling is capacitive in order to maximize the electric part of the signal.

The characteristics of the readout resonator depend on the materials used and on its geometry. In general, $\frac{\lambda}{2}$ or $\frac{\lambda}{4}$ resonators are employed. When studying the propagation of the fundamental TEM mode, we observe in both cases nodes and anti-nodes of the electric and magnetic parts of the signal, as shown in Figure 3.3.

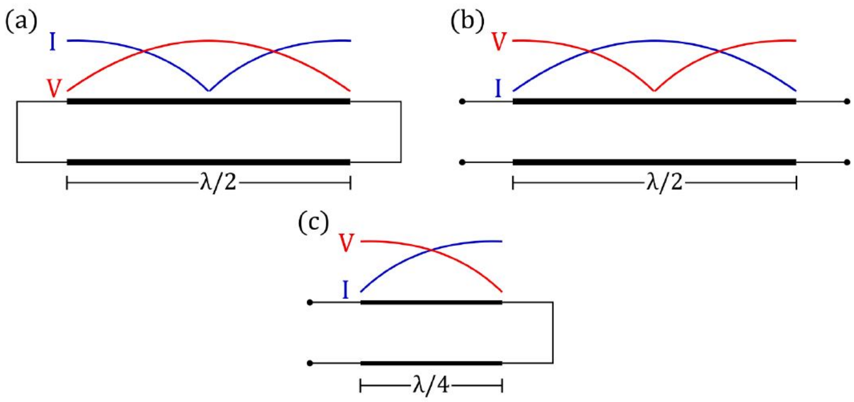

Figure 3.3: Schematic of a $\frac{\lambda}{2}$ resonator **a)** short-circuited (it maximizes the current **I**, hence the magnetic field needed for an inductive coupling) and **b)** open (it maximizes the voltage ***V***, hence the electric field needed for the capacitive coupling). In **c)** a schematic of $\frac{\lambda}{4}$ resonator. The ***V*** in the graphs refers to the electric part of the TEM mode, whereas the ***I*** to the magnetic part.

By tuning the length and the design of the resonator, both the $\frac{\lambda}{2}$ and $\frac{\lambda}{4}$ designs are feasible. However, in the chip measured and analyzed in this work the $\frac{\lambda}{4}$ resonator are employed. The loaded (total) quality factor is related to the internal and coupling quality factors in this way:

$$\frac{1}{Q_l} = \frac{1}{Q_i} + \frac{1}{Q_c}. \tag{3.1}$$

Q_c considers how well the resonator is coupled to the feedline [39], while Q_i takes into account other possible loss mechanisms in the resonator, such as film and dielectric losses, radiation loss, etc. [39].

3.2 Dilution Cryostat

The study of superconducting qubits requires the use of a dilution refrigerator, which cools down the qubits to 10 mK. In Figure 2.6 we showed the energy levels of a JJ, which are engineered in the transmon in such a way that the ground $|0\rangle$ and excited $|1\rangle$ states are separated by several GHz. We can associate this energy to an equivalent temperature according to:

$$T = \frac{h\nu_{01}}{k_B}, \tag{3.2}$$

and the typical equivalent temperature is around 200 mK. If the qubits are sufficiently below this temperature, transitions between the two computational levels are undoubtedly due to the drive signal and not to thermal fluctuations.

We have employed the dilution cryostat in Figure 3.4a for qubit characterization. It is a dry dilution BlueFors refrigerator [40] at the CESMA-UniNa-Seeqc joint lab.

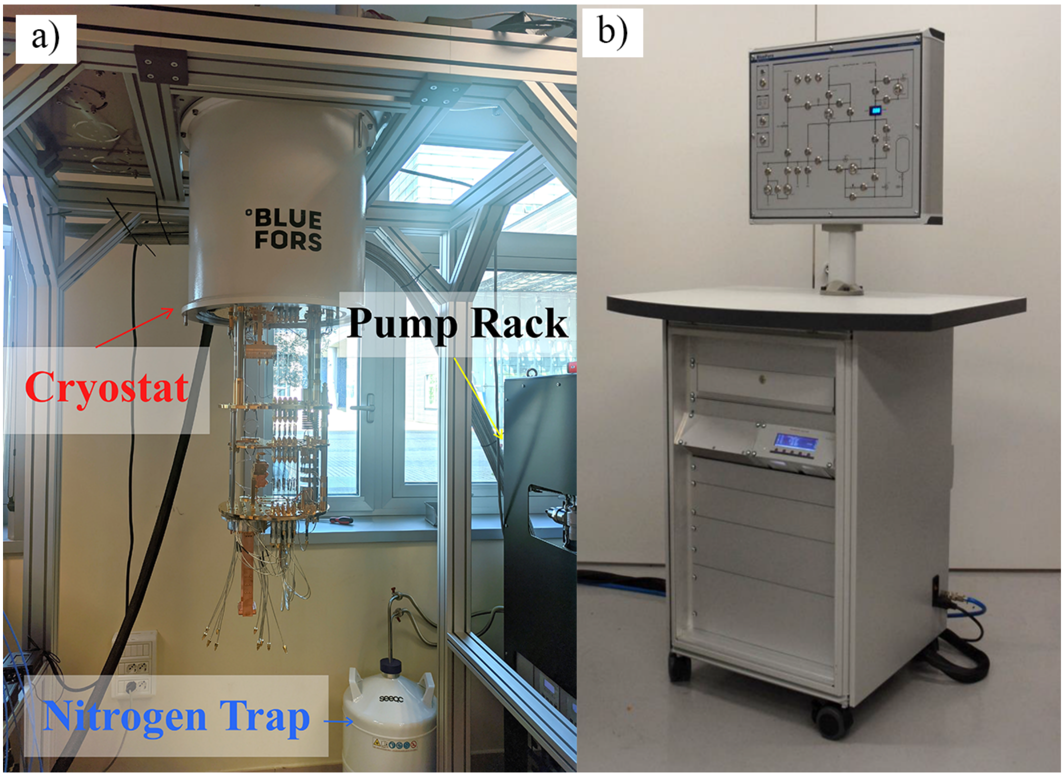

Figure 3.4: BlueFors dilution cryostat at the CESMA-UniNa-Seeqc lab. In **a)**, inner view of the cryostat, the pump rack and nitrogen trap and **b)** Control Unit (CU).

Dilution refrigerators allow to reach and continuously maintain temperatures around 10 mK. The BlueFors cryostat consists of three basic components: the cryostat, the Gas Handling System (GHS) (**a**)) and the Control Unit (CU) (**b**)), as shown in Figure 3.4a and b.

The dilution cryostat uses a mixture of two isotopes of helium ($^3He/^4He$) mixed in specific concentration. The process takes advantage of the *dilution method*, which is endotermic [41]. In the Bluefors system, a Cryomech Inc. Pulse Tube (PT) cooler delivers low enough temperatures to start the dilution refrigeration (DR) cycle. The cooling schematic is reported in Figure 3.5a. First there is a cold trap at approximately 50 K, which takes any contamination out of circulation by freezing it, but also serves as a heat exchanger. The incoming gas is then thermalized at the regenerator tube and the 2nd stage of the PT. Figure 3.5b and c show the main parts of our dilution refrigerator: quasi-4K flange, still, heat exchangers, mixing chamber and heat switches. The heat switches are used for the initial pre-cool of the DR with the PT from room temperature to low enough starting temperature (approximately 4.2 K). After the DR is pre-cooled to <4.2 K, i.e. when ^4He is in the liquid state, the $^3He/^4He$ mixture has to be condensed into the system. In order to start the condensation, it is necessary to compress the gas with a ^3He mixture compressor and reduce the temperature below 4 K. The mixture passes through an impedance where

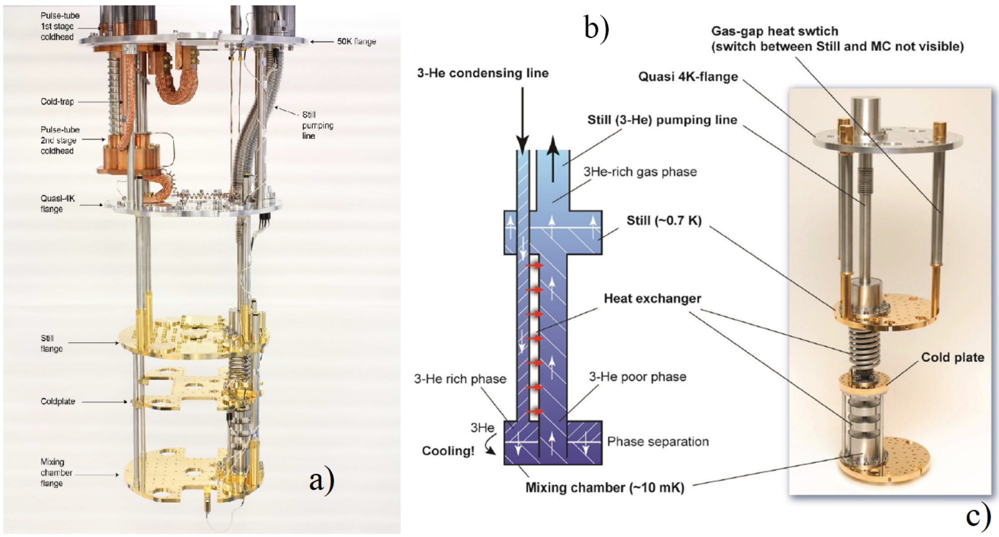

Figure 3.5: a) View of the BlueFors cryostat showing the main components. The pre-cool circuit inside the cryostat, which is responsible for cooling the cryostat to around 4.2 K highlighted in **a)**, while in **b)** we show the dilution process. In **c)** the dilution unit, which enables us to reach temperatures around 10 mK.

it can undergo isoenthalpic expansion and reach a temperature lower than 2 K, at which also the ^3He is liquid. This cooling phase occurs in the dilution unit (DU). Then the mixture is pumped by the pumping rack, consisting of a turbo and rotative pumps and ^3He compressor, thus lowering the temperature below 1 K. From the phase diagram in Figure 3.6 it is clear that, by continuously cooling the mixture to 800 mK, the mixture reaches a critical point in the diagram.

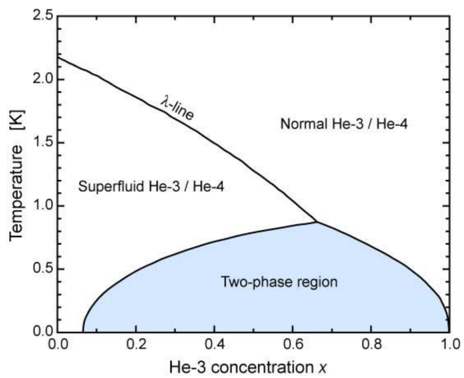

Figure 3.6: Phase diagram of the $^3He/^4He$ mixture: dilution occurs under 0.8 K. When we reach this threshold, we have the separation into a dilute and a concentrated phase.

In the Mixing Chamber (MC) the dilution occurs and two phases are formed: a concentrated one and a diluted one. The concentrated phase is mostly ^3He, while the diluted one is mostly ^4He with a small fraction of ^3He. The diluted mixture is pumped from the MC to the still by the pumping system. The enthalpy of ^3He in the dilute phase is larger than in the concentrated phase. Hence energy is required to move ^3He atoms from the concentrated to the dilute phase, so cooling will occur down to 10 mK. The process is maintained active in a closed loop.

There is also an external cold trap in the loop, which is mainly used to clean the mixture from various contaminants. The cold trap is immersed in a container filled with liquid nitrogen and is a sponge-like material containing activated charcoals. The contaminants get absorbed by the charcoal as the mixture passes through the cold trap.

The cryostat has a plate structure, as shown in Figure 3.5. This structure helps the exchange of heat in the dilution process and allows the MC to reach 10 mK. At each of these plates, external screens are used as vacuum or radiation shields. The most external shield, anchored at the RT plate, is necessary to establish a vacuum of 10^{-4} mbar in order to decouple the fridge from the environment. This is achieved with the help of a rotary and a turbo pump. Other shields, anchored at the 50 K plate, the quasi-4 K plate, the still plate, the cold plate and the MC plate, serve as Electromagnetic Faraday cages. The MC and the still plate, in particular, use gold-plated copper screens, which shield from infrared radiation.

3.3 Cryogenic and room-temperature electronics

The cryostat is equipped with RF coaxial input and output lines, and cryogenic electronics, thermally anchored to different cryostat plate stages. These plates are made of gold-plated copper with large thermal conductivity. A photo and a sketch of the lines in the DR are shown in Figure 3.7.

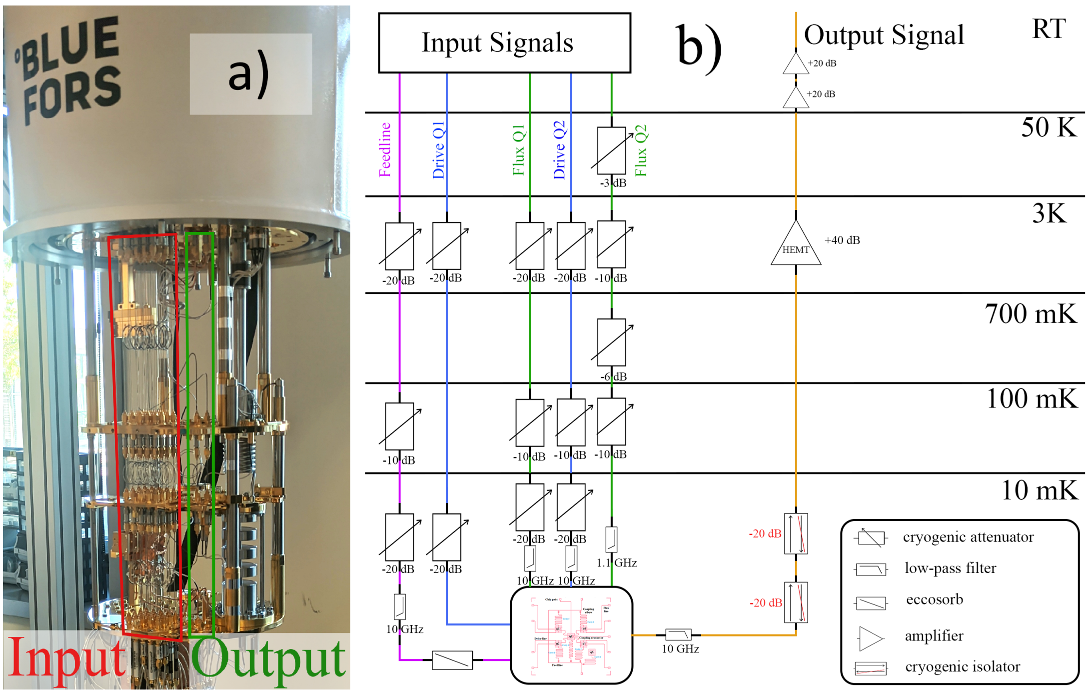

Figure 3.7: a) Input and output lines used for microwave measurements. These lines are thermalized to the plates by a copper bracelet. **b)** Representation of the lines, attenuation, filtering and amplification scheme.

In order to control the qubits, we must use signals which resonate with their characteristic frequencies, which are usually around the low GHz range. The input RF lines are made of stainless steel and are thermalized at every plate. The output lines are made of Cu-Ni, down to the 4 K plate, and then by Nb-Ti, which is superconducting from the 4 K plate to the MC. By using a series of attenuators located at the 4 K plate, the 100 mK plate and the MC plate, it is possible to attenuate the input signal by 50 dB, as shown in Figure 3.7b. Furthermore, the input lines made of stainless steel attenuate the signal by 10-20 dB in the 4-8 GHz range. This is an important request for low-power RF experiments, such as for superconducting qubits which work in the single-photon regime.

The signal response of the qubit is very weak and it needs to be amplified in order to be detected by the external electronics. We use a HEMT (High Electron Mobility Transistor) amplifier at 4 K [42]. The HEMT amplifier is biased by the LNF-PBA from Low Noise Factory [43], which is a Low Noise Power Block (LNPB) (see Figure 3.8) [44], and it supplies the power to another box called LNF. It uses the voltage source to apply a DC bias to the HEMT. In this way it enables us to adjust the drain current and voltage (I_d and V_d) and the voltage gap (V_g). The HEMT operates with 40 dB of amplification from 4 to 8 GHz.

Even though HEMT amplifiers are needed to amplify the signal, they also add noise sources, since they are active elements. In order to protect the qubit from these noise sources, we use cryogenic isolators at the MC plate. An isolator is defined as a device which isolates an electromagnetic device from spurious reflections and transmission of an electromagnetic wave [45]. The waves may be freely transmitted in the direction from the device through the isolator to the room temperature electronics (designated the forward direction), but waves originating outside of the device and traveling in the opposite direction (designated the reverse direction) are attenuated by the isolator to prevent harmful disturbance on the system under test. The attenuation to the reverse direction is of around 20 dB in a frequency range up to 12 GHz, so totally there are 40 dB of attenuation through the two isolators.

Finally, the sample is further protected from external radiation and magnetic fields with a copper-plated cryoperm screen and a tin-plated screen, which is superconducting at low temperatures. There are also various filters, like ecosorb filters and low-pass filters helping in reducing electromagnetic interference at the MC.

A comprehensive showcase of the room temperature set-up for qubit characterization is given in Figure 3.8. Among the main instruments, particular attention should be put on the VNA (Vector Network Analyzer) [46], the up- and down-conversion cards [47], the AWGs (Arbitrary Waveform Generator) [48], the RF signal generators [49], [50], [51] and the digitizer [52]. These are used to generate and measure RF signals in a continuous way and to generate and measure RF signals in the time-domain, respectively. In addition, there is an attenuator card [53] used to further attenuate input RF signals, an amplification card for the output signals and a switch card used to switch from continuous to time-domain measurements.

3.4 Up - and down-conversion

A schematic representation of the time-domain measurement setup is shown in Figure 3.9. The AWG used in the experimental setup is able to generate microwave signals with frequencies up to 400 MHz [48]. Since qubits operate typically in the 4-8 GHz range,

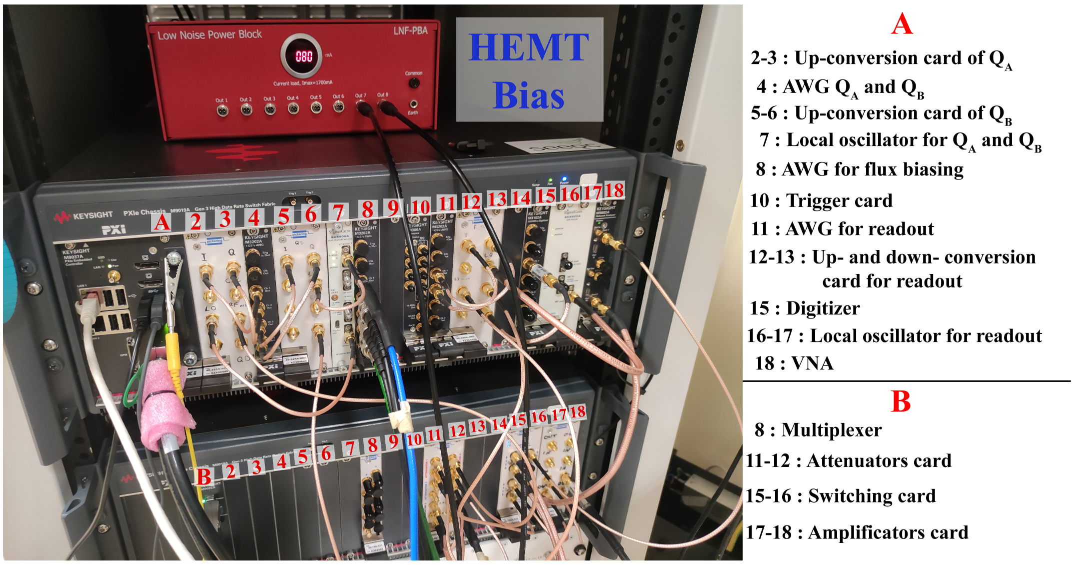

Figure 3.8: Keysight rack with instruments used for characterization of qubits and HEMT bias power supply. All the instruments are reported in the legend. The trigger and the multiplexer cards have not been used in this work.

we need faster signals. Commercial AWGs which generate in the GHz range exist, but are very expensive and more importantly generate pulsed signals with significant noise in the GHz range [48]. For these reasons, we combine the AWG signal with an RF signal (Local Oscillator LO) through an I-Q Mixer (in Figure 3.8, I-Q Mixers are stored in the up and down conversion cards). This process is called up-conversion. In order to generate an appropriate high frequency signal, the AWG provides the I (the in-phase part of the signal) and Q (the quadrature of the signal) of the intermediate (IF) signal (ω_{AWG}), with a frequency lower than that of the LO signal (ω_{IN-LO}), sent into the LO port of the up- and down-conversion card. The I-Q Mixer output frequency is the input signal for the qubit (ω_{in}) and is given by:

$$\omega_{in} = \omega_{AWG} \pm \omega_{IN-LO} \tag{3.3}$$

While the input RF signal has still two frequencies, single-sideband calibration allows to select just one of them, efficiently generating a high-frequency RF signal [54]. Finally, the signal is attenuated at room temperature and further attenuated with cryogenics attenuators in order to work in the single photon regime.

The output signal is of the order of several GHz, hence it would be very difficult for the electronics to read it properly. For this reason demodulation and *down-conversion* are necessary. The output signal goes in a mixer, which has only 3 ports compared to the I-Q mixer which has 4 ports. It combines with the LO signal and the resulting signal has the following frequency:

$$\omega_{IF} = \left|\omega_{out} - \omega_{LO-IN}\right|. \tag{3.4}$$

ω_{IF} is low enough for the digitizer to work properly and convert the signal, in the required frequency range of the order of 0-500 MHz [52]. It acquires for a time $t_{acq} = \frac{N_m}{\nu_s}$, where N_m is the number of measurements and ν_s is the sampling rate of the digitizer, which is 500 MSamples/s. The acquisition time length must be a compromise between a sufficient number of samples during the readout (RO) pulse and the need to remain inside the duration of the RO pulse signal. The aim is to avoid bad triggering and asynchronous

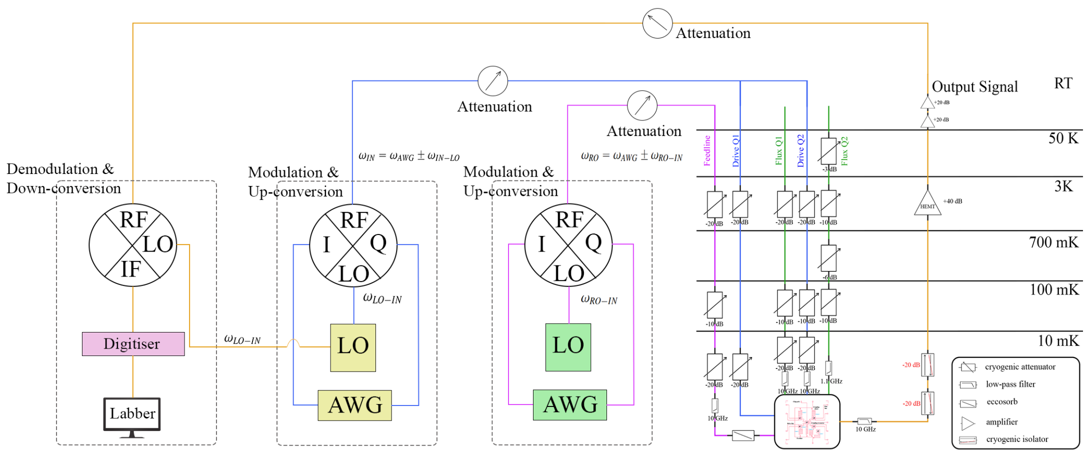

Figure 3.9: Simplified schematic of the experimental setup used for dispersive qubit readout and drive. The blue circuit is responsible for the drive signals, which uses up-conversion, while the orange circuit is responsible for the readout of the output signal, which uses down-conversion. The magenta circuit is responsible for the readout input signal, which uses up-conversion.

acquisitions, while acquiring enough data points. Finally, a Fast Fourier Transform is performed by the integrated software of the digitizer in order to extract the original form of the RO signal coming from the resonators coupled to the qubits. The results are displayed and stored through the Labber software [55]. In Appendix A we show a brief example on how the I-Q mixers are used for up-conversion.

3.5 Vector Network Analyser for continuous wave spectroscopy

Spectroscopy measurements provide fundamental information about the qubits under test, as it will be shown in Sections 4.1 and 4.2. To perform these measurements we use the VNA, an instrument used for studying continuous signals. The VNA is a two-port network, i.e. it is an electric circuit with two pairs of terminals (input and output), as shown in Figure 3.10. Mathematically, a two-port network is fully described by a 2×2 matrix of complex numbers that establish relations between the voltage and current across the ports. A convenient way of expressing the properties of a two-port network is the *ABCD matrix* [17]:

$$\begin{pmatrix} V_1 \\ I_1 \end{pmatrix} = \begin{pmatrix} A & B \\ C & D \end{pmatrix} \begin{pmatrix} V_2 \\ -I_2 \end{pmatrix}. \tag{3.5}$$

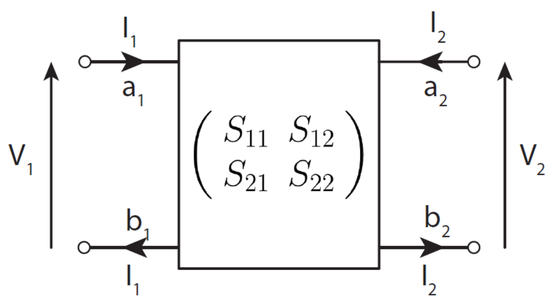

Figure 3.10: Schematic of a two-port network characterized by its scattering matrix

When dealing with high frequency signals, it is difficult to accurately measure directly voltages and currents, hence power and energy variables are used. Thus, the scattering matrix describes the relationship between the incident (a_1, a_2) and reflected (b_1, b_2) waves and is given by:

$$\begin{pmatrix} b_1 \\ b_2 \end{pmatrix} = \begin{pmatrix} S_{11} & S_{12} \\ S_{21} & S_{22} \end{pmatrix} \begin{pmatrix} a_1 \\ a_2 \end{pmatrix}. \tag{3.6}$$

The element in the scattering matrix are called scattering parameters. Each scattering parameter (S parameter) consists of a complex number, which represents the magnitude and phase response of the device at a given frequency. S_{11} and S_{22} are known as the reflection coefficients from port 1 and port 2, whereas S_{21} and S_{12} correspond to the transmission from port 1 to port 2 and vice versa. For a reciprocal two-port network, it holds true that $S_{12} = S_{21}$ and for a symmetrical network $S_{11} = S_{22}$ [17]. Therefore, the VNA is the instrument which sends the signals and measures the response, as shown in Figure 3.11. The real and imaginary parts of the transmission parameter S_{21} are the key quantities for qubit characterization, since they allow to extract the readout resonator characteristics (resonance frequency, dispersive shift and quality factors) and qubit transition frequencies, as shown in Sections 5.1 and 5.2, respectively.

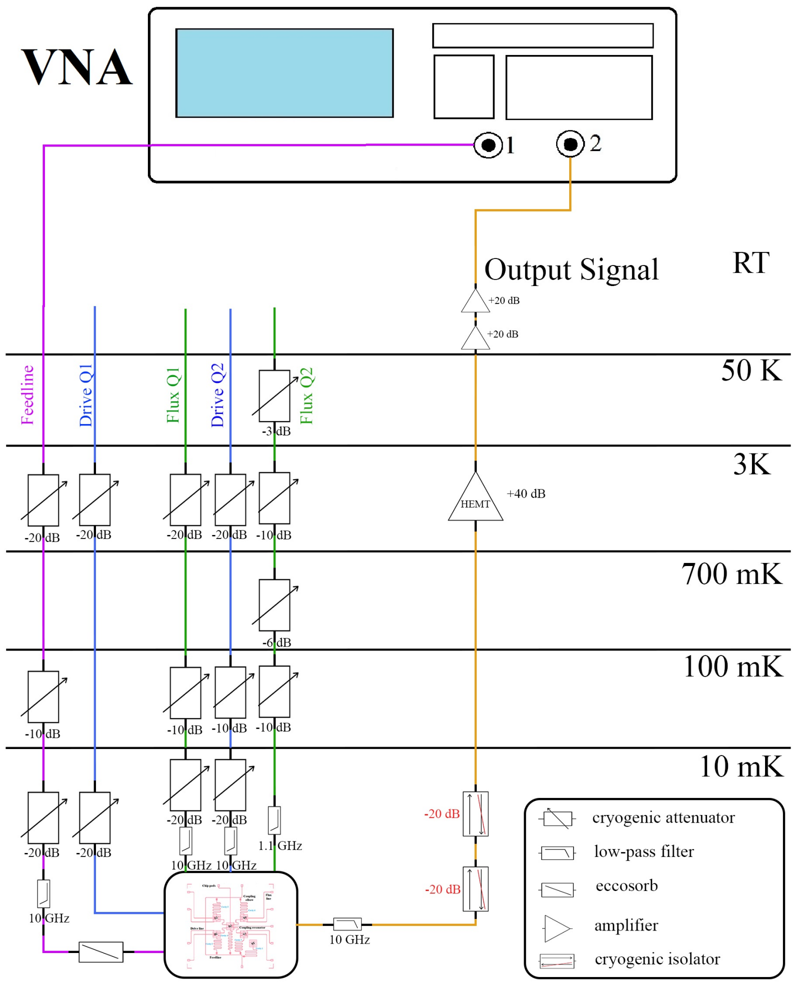

Figure 3.11: Experimental set-up of spectroscopic measurements done with the VNA. The VNA generates the input signal sent to the qubits (magenta line) measures the response (orange line).

4 Protocols for single- and two-qubit characterization

The implementation of a precise protocol is crucial for the realization of high-fidelity gates. By accurately studying the characteristics of the single qubits, we are able to define the basic features of the signals, like the characteristics of π-pulses and the behavior of the qubits as a function of the external flux. These characteristics will be the starting point for the signal optimization, which includes corrections on the output signals of the external electronics. Thanks to these procedures, we are able to reach high single-qubit fidelities. The optimization of the single qubits is the starting point for the implementation of high fidelity multi-qubit gates.

In order to characterize superconducting qubits, we have used a wide variety of protocols, which explore all the important features of the single qubits, in agreement with what is commonly reported in literature. In Section 4.1 we show how to perform the readout resonator spectroscopy, whereas in Section 4.2 the qubit spectroscopy. In Section 4.3 we discuss the time-domain protocols: Rabi oscillations, T_1 measurements, T_2 measurement with Ramsey interferometry and Hahn echo. In Section 4.4 we explain how to calibrate the pulses used in Randomized Benchmarking for the single qubit fidelity measurements. In Section 4.5 we show the Randomized Benchmarking protocol. Finally, we discuss how to put two coupled qubits on-resonance with each other in order to perform an iSWAP gate (Section 4.6).

4.1 Readout resonator spectroscopy

Readout resonators spectroscopy allows to check if all the readout resonators are present, whether their frequency corresponds to the designed value and also looks at the frequency separation between the readout resonators. The latter is important for two reasons: i) if the readout resonators are too close to each other, they might overlap and this would interfere with the readout and ii) if the readout resonators are too far apart from each other, multiplexed readout, fundamental for the implementation of multi-qubit simultaneous readout, becomes a hard task.

In the readout resonator spectroscopy, the input signal is a *single tone* signal, which is in the range of the resonance frequencies of the resonator. This signal resonates with the readout resonators and a typical lorentzian dip stands out among the background.

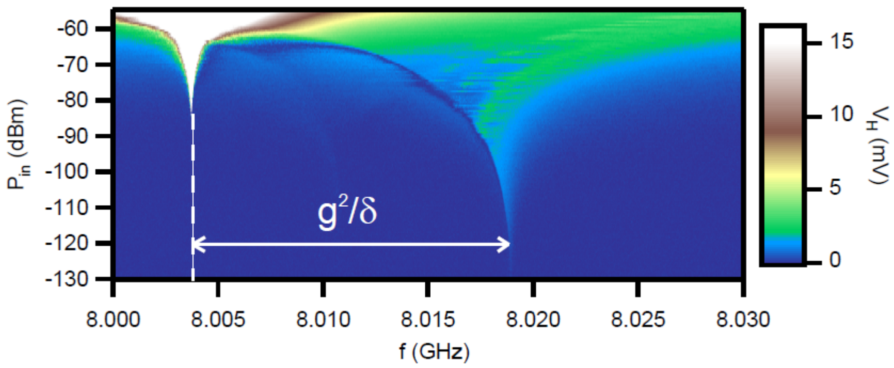

Figure 4.1: Example of dispersive shift spectroscopy from [56]. It shows the shift from the bare to the dressed state, in accordance with Section 2.5.1.

Once all the readout resonators are found, another very important procedure consists in finding out if there is dispersive shift [4]. This measurement guarantees that the resonator is sufficiently coupled to a working qubit. An example of a dispersive shift measurement is shown in Figure 4.1 and consists in performing readout resonator spectroscopy as a function of the power of the input signal. For high values of the input power, the qubit is completely saturated and the input signal only resonates with the frequency of the isolated readout resonator (bare state). The dispersive shift is recovered by decreasing the input signal, i.e. pointing towards the single-photon regime. The readout resonator resonance shift allows to estimate the coupling between the readout resonator and the qubit, as discussed in Section 2.5.1.

4.2 Qubit spectroscopy

For qubit spectroscopy we send a *two tone* signal, composed of an RF signal which is close to the frequency of the readout resonator resonance in the dispersive regime, sent through the feedline to excite the resonator (readout tone), and an RF signal which sweeps in power and in frequency, which excite the qubit (drive tone). The latter can be either sent through the feedline or dedicated qubit drive (QD) lines. Continuous wave qubit spectroscopy uses the VNA to send the readout tone, which is made of three frequency points close to each other (few kHz span). The reason is that the VNA is not able to send a single frequency, so we rather send three very close frequencies. The result of the three measurements, as a function of the qubit signal, is averaged.

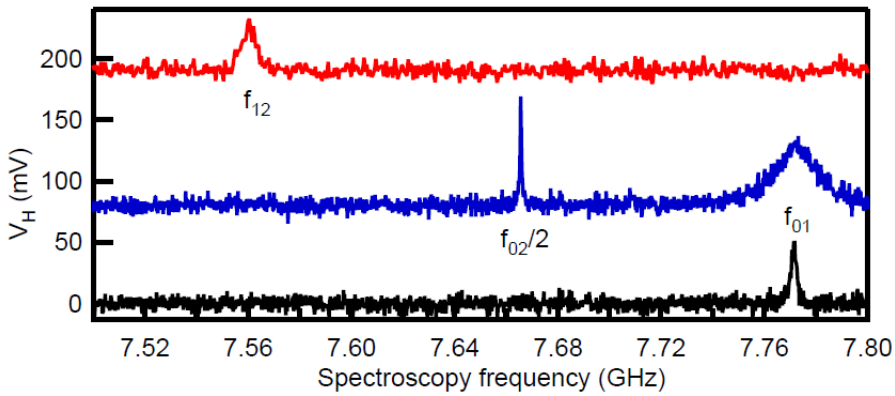

Figure 4.2: Example of qubit spectroscopy showing the different transition frequencies ($|0\rangle \rightarrow |1\rangle$, $|1\rangle \rightarrow |2\rangle$ and $|0\rangle \rightarrow |2\rangle$) [56].

When the drive tone is off-resonance with the qubit, the background of the output signal corresponds to the resonator output signal in the dispersive state, but when it is on-resonance, there will be a peak, representing the transition frequency of the transmon ω_{01}. By varying the drive tone power, it is possible to see more than the $|0\rangle \rightarrow |1\rangle$ transition, like the $|1\rangle \rightarrow |2\rangle$ and $|0\rangle \rightarrow |2\rangle$ transitions, like in Figure 4.2.

4.3 Time-domain protocols

Time-domain measurements are at the core of the qubit characterization. Compared to continuous wave measurements, in time-domain experiments readout and drive tone signals are replaced by microwave pulses sequences, generated with I-Q mixers, AWGs and

RF signal generators, as discussed in Section 3.4. The output signals are down-converted and read out by the digitizer (Section 3.4). Although this is of immeasurable importance when investigating the time-domain response of the qubit, pulsed-measurements can be also used for resonator and qubit spectroscopy, once readout and drive pulses durations are longer than all the typical time-scales of the qubit (above tens of microseconds). In this case, readout and drive pulses can be treated as continuous signals. In the following, we will report the most important time-domain protocols for qubit characterization.

4.3.1 Rabi oscillation

Once all the parameters for the readout resonator and the qubit are inspected through spectroscopy measurements, including the frequency and the power of the readout tone in the dispersive regime and the qubit frequencies, Rabi oscillations measurements provide the estimation of a fundamental quantity for single- and two-qubit gate implementation: the π-pulse. The π-pulse is a drive signal on-resonance with the qubit frequency with an amplitude able to bring the qubit from the ground state to the first excited state. Basic single-qubit gates reported in Section 2.8, like the X and Y gates, are nothing else than π-pulses sent in order to perform a transition from the ground to the excited states of the qubit around the x- or y-axes. The difference between the two pulses is just given by the addition of a relative phase in the drive pulse, but its amplitude is only related to the outcomes of Rabi oscillations.

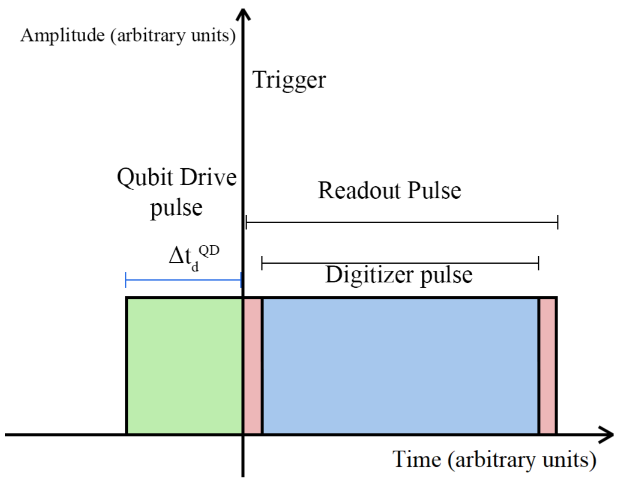

Figure 4.3: Pulse sequence used to measure Rabi oscillations in qubits. Δt_d^{QD} is the qubit drive duration.

In Section 2.5.3 we have obtained for the Rabi oscillations the following result for the population P_1 of the two level system:

$$P_1 = \frac{\omega_d^2}{\omega_d^2 + \delta\omega^2} \sin^2\left(\frac{t\sqrt{\delta\omega^2 + \omega_d^2}}{2}\right), \tag{4.1}$$

which oscillates with the Rabi frequency $\Omega_r = \frac{\sqrt{\delta\omega^2+\omega_d^2}}{2}$, as shown in Figure 2.14. In order to measure the Rabi oscillations, we send an RF signal to excite the qubit, followed by a readout signal sent to the resonators. Reading and digitalization of the output must occur simultaneously. Indeed, we build a sequence in which the digitizing pulse falls inside the readout excitation pulse. An example of the protocol is reported in Figure 4.3. In this measurement, the changing parameter is the QD pulse plateau Δt_d^{QD}, i.e. its duration. The longer it becomes, the larger to induce the transition from the ground state to the first excited state and then again to the ground state. This explains the expected oscillatory behavior of a Rabi measurement.

All these signals must be well aligned, in fact there must not be overlap between different signals or timing mismatches. For these reasons the trigger is carefully chosen. Finally, by changing the amplitude and the frequency of the drive pulse tone, we can have a more precise way to measure the qubit frequency, obtained with spectroscopy measurements, and the π-pulse duration.

For the former, in fact, one can notice that when a detuning between the drive and the qubit frequencies occurs, the Rabi oscillations change both the periodicity and the amplitude. To better see these behaviours, see Figure 4.4, which is the so-called *Chevron plot* [57]. It shows how much the qubit is detuned from the rotating frame frequency, i.e. the drive-qubit frequency detuning $\delta\omega = \omega_q - \omega_d$. The Chevron plot shows that with increasing detuning the amplitude of the Rabi oscillations decreases, while their frequency increases, in accordance with Eq. 4.1. The on-resonance qubit frequency is indeed the center of the Chevron plot.

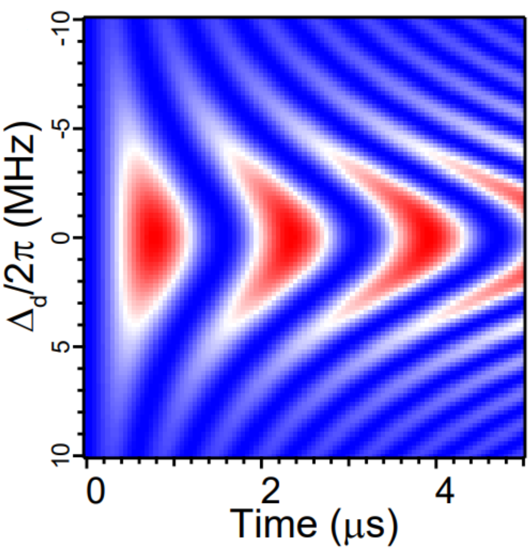

Figure 4.4: Example of Chevron plot for Rabi oscillation in a qubit [57], where the gradient represents the amplitude of the oscillations, in terms of the detuning between the qubit frequency and the drive signal $\delta\omega$, and the duration of the drive pulse.

At the on-resonance frequency of the drive pulse, we can estimate the π-pulse as the semi-period of the Rabi oscillation. However, the π-pulse duration also depends on the power of the drive RF signal:

$$\Omega_r = \sqrt{A^2 + \delta\omega^2}. \tag{4.2}$$

The larger the power of the drive pulse is, the faster the Rabi oscillations are, and as a consequence the π-pulse is shorter. The request for Quantum gate operation is to have the π-pulse as short as possible, in order to have the largest number of gates implemented in the coherence time of the qubit. However, we must find a compromise in the choice of the π-pulse power. As a matter of fact, large drive powers can lead to higher-order transitions (as discussed in Section 4.2), which fall outside of the computational space of our qubit and may be detrimental for the quality of the gate. The better compromise in defining the π-pulse for gate operations is to have the speediest pulse, while setting the QD power weak enough to avoid transitions to higher-energy levels of the transmon. The effect of the QD power in Eq. 4.2 is shown in Figure 4.5 [57].

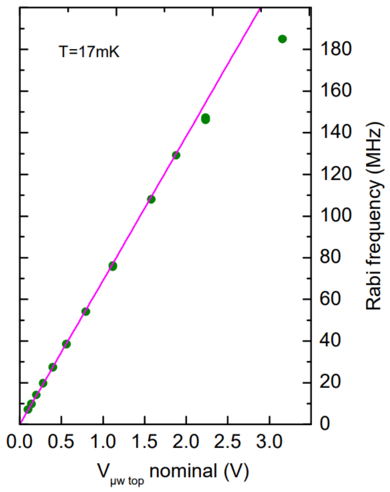

Figure 4.5: Linear dependence of the Rabi frequency as a function of the qubit drive signal amplitude $V_{\mu w\,top}$. Figure adapted from [58].

4.3.2 T_1 measurements

The estimation of the π-pulse is not only fundamental for gate implementation, but also for the measurement of relaxation, dephasing and coherence times of a qubit. As we discussed in Section 2.8, the coherence and relaxation times give a first indication of the maximum fidelity achievable in a superconducting qubits. To measure the relaxation time T_1, we use a protocol which brings the qubit in $|1\rangle$, by sending a π-pulse, and then we measure its state after an increasing amount of time. In Figure 4.6 we report the T_1 protocol sequence.

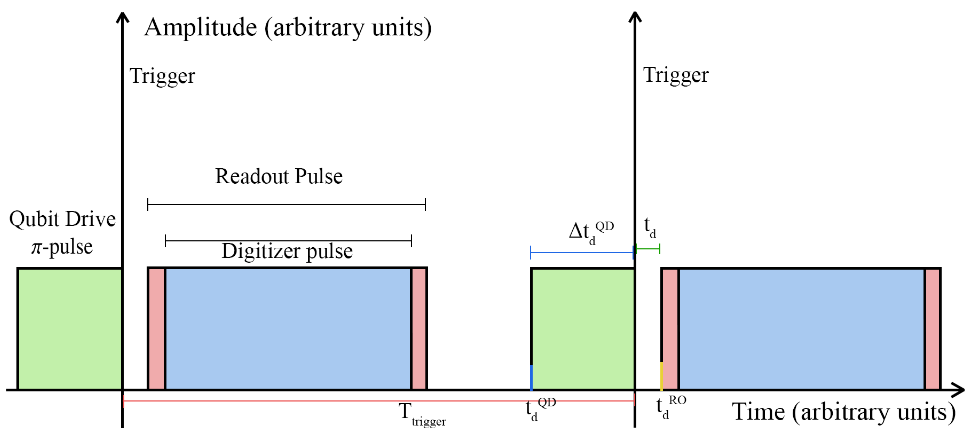

Figure 4.6: Example of a pulse sequence used to study T_1 [4].

The main idea behind this sequence is the following:

- The trigger gives the start of the sequence.

- After a time t_d^{QD} from the trigger the QD π-pulse of duration Δt_d^{QD} is sent.
- There is a delay t_d, as shown in Figure 4.6, between the QD pulse and the Readout (RO) pulse. This is crucial for the protocol, because it allows us to study the relaxation of the qubit. The larger the delay t_d is, the more the qubit relaxes from the excited state $|1\rangle$ to the ground state $|0\rangle$.
- In order to extract the data on the state of the qubit, as usual, the digitizing pulse falls inside the readout excitation pulse.

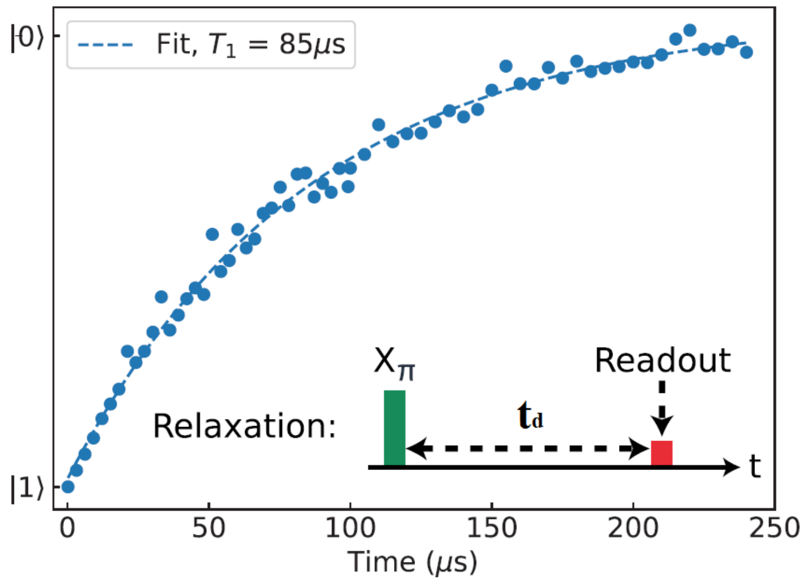

Figure 4.7: Example of a T_1 measurement result and protocol, and simplified diagram for the sequence [4].

The graph in Figure 4.7 is obtained by varying t_d, which represents how much the qubit relaxes from the excited state until we measure its state.

4.3.3 Ramsey Interferometry

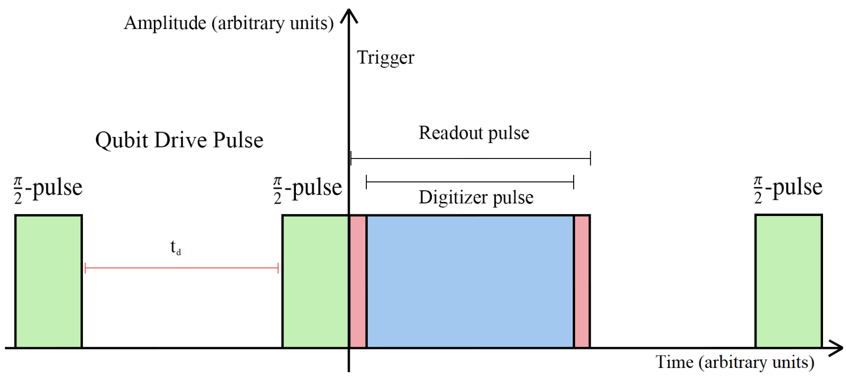

Figure 4.8: Example of pulse sequence used for Ramsey interferometry

Another typical protocol used for the study of the quality of a qubit is Ramsey interferometry. We first prepare the qubit on the equatorial plane of the Bloch sphere sending a $\frac{\pi}{2}$ pulse, i e. with half π-pulse amplitude, and we wait for a variable time period before the application of another $\frac{\pi}{2}$ pulse, which brings the qubit in the excited state. We can measure the effect of dephasing, which is more important the longer the time delay is between one $\frac{\pi}{2}$ pulse and the other.

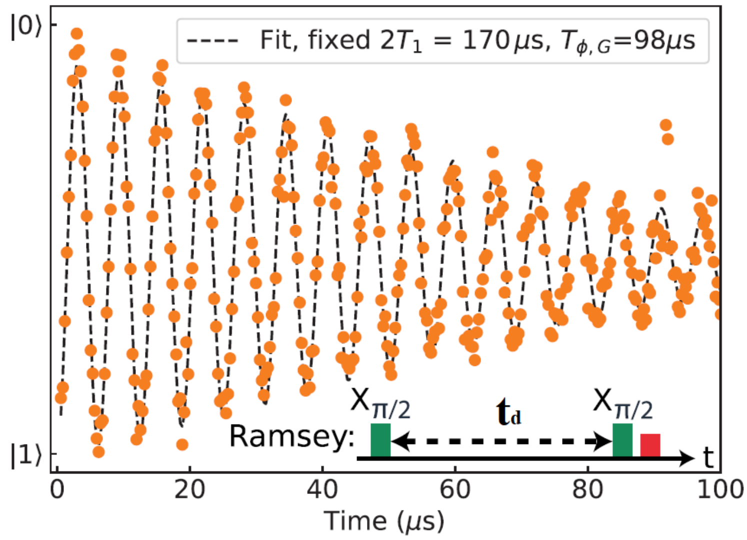

Figure 4.9: Ramsey interferometry with simplified diagram of the sequence. This measurement allows give an estimate of the T_2, which is usually identified as T_2^* [4].

This results in the sequence in Figure 4.8 and it provides the measurement of Ramsey oscillations in Figure 4.9, where the delay time t_d between the two $\frac{\pi}{2}$-pulses is increased. This method provides a quantity called T_2^*. The * stands for the fact that the Ramsey experiment is sensitive to *inhomogeneous broadening*, i.e. it is highly sensitive to quasi-static, low-frequency fluctuations [4].

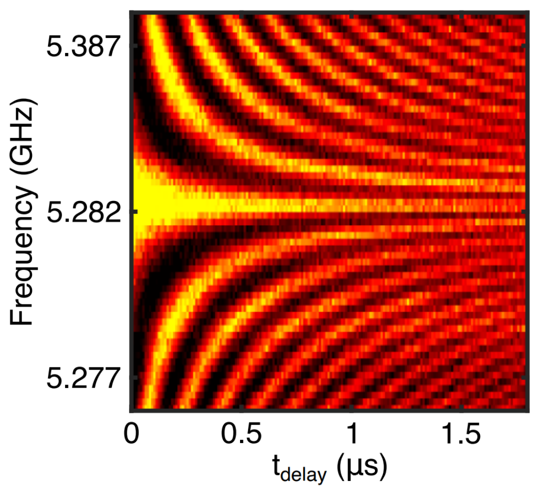

Figure 4.10: Example of Ramsey fringes as a function of the qubit drive frequency and time delay t_d between the two $\frac{\pi}{2}$ pulses. Figure adapted from [59].

When performing the qubit drive for the Ramsey interferometry the detuning $\delta\omega = \omega_q - \omega_d$ between the qubit frequency and the QD frequency is crucial. The Ramsey output signal is proportional to $\cos(\delta\omega t)e^{-\Gamma_2^* t}$. When $\delta\omega$ is non zero, we are off-resonance and we expect the system to behave as a damped oscillator [4]. The period of these oscillations corresponds to the detuning $\delta\omega$ and the damping provides an estimate of T_2^*. When

$\delta\omega = 0$, we are on-resonance, hence the oscillations vanish and we measure an exponential decay of the qubit state. This behaviour is shown in Figure 4.10. If the detuning increases, then the oscillations become faster. Furthermore, when we are off-resonance, the detuning contributes to dephasing in the equatorial plane, but when we are perfectly on-resonance, this dephasing should decrease [4].

4.3.4 Hanh echo protocol

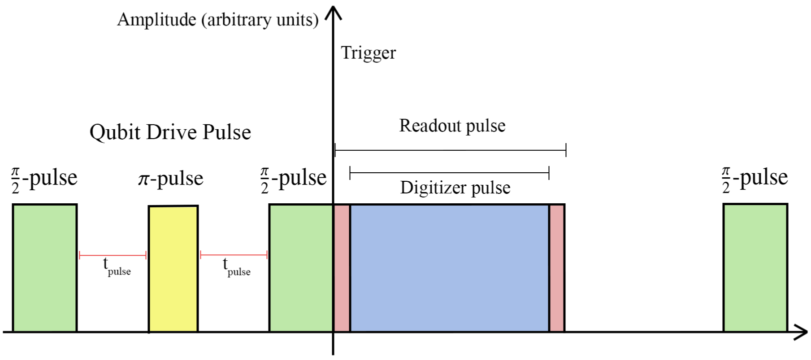

Figure 4.11: Example of pulse sequence used for Hahn echo protocol

One last common procedure used to characterize qubits is the Hahn echo protocol. The main goal is to determine the coherence time T_2. The sequence used to send the pulse is very similar to the Ramsey sequence and is shown in Figure 4.11. The main difference relies in the application of a π-pulse in the middle of the Ramsey sequence. The mid-π-pulse is also known as *refocusing* pulse, and allows to perform a rotation of π around the z-axis of the Bloch sphere, after the qubit preparation in the equatorial plane. By doing so, the quasi-static contributions to dephasing can be suppressed, leaving an estimate of T_2 that is less sensitive to inhomogeneous broadening mechanisms.

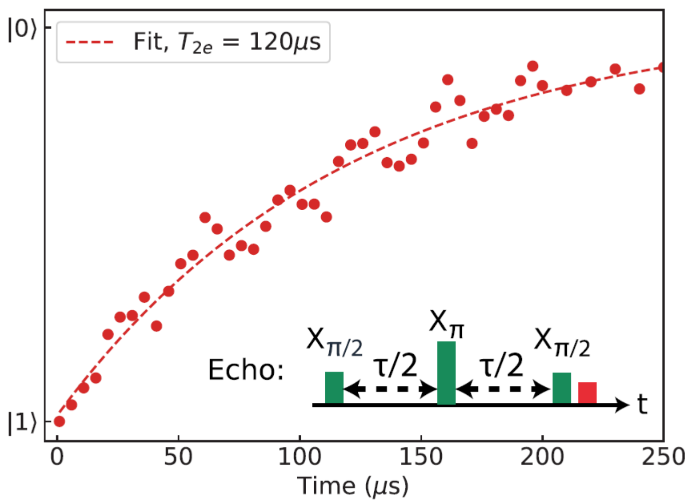

Figure 4.12: Hahn echo experiment with simplified diagram of the used sequence. T_{2e} in the figure is equal to T_2 in the thesis. Figure adapted from [4].

In [60], it has been demonstrated that the inclusion of multiple π-pulses in the middle of the Hahn-echo sequence allows to approach the theoretical limit in absence of dephasing for a qubit, $T_2 = 2T_1$, in accordance with Eq. 2.39 in Section 2.6.3. Depending on the coherence properties of the qubit, a single π-pulse may not completely cancel dephasing contribution. From the results in the measurements in Figure 4.9 and 4.12, we see that the T_2 measurement (120 μs) approaches the limit $2T_1$ (170 μs) [4].

4.4 Pulse optimization for Randomized Benchmarking test

The measurement of relaxation and coherence times in a superconducting qubit is a fundamental step in order to provide a first estimation of the qubit fidelity. However, the experimental protocol for the study of the performances of a superconducting qubit in Quantum processors necessarily requires a careful benchmark of its performances. As mentioned in Section 2.8, Randomized Benchmarking (RB) is one way to evaluate the performance of the qubit.

RB test is based on the measurement of the qubit state after the application of a sequence of Clifford gates. Such Clifford gates are mainly made by a combination of X and Y gates, i.e. drive pulses with π- and $\frac{\pi}{2}$-amplitudes. The implementation of quantum algorithms [38], [61] requires single-qubit fidelities above 99.9 % [10], [11], [62]. One way to achieve such high fidelities is to reduce state preparation and measurement (SPAM) errors, which contribute to the fidelity, as stated in Section 2.8. SPAM errors [63] can be reduced by a careful generation of drive pulses. As provided in more detail in Section 4.3, I e Q signals for π-pulses are typically provided by an Arbitrary Waveform Generator (AWG) and by using an I-Q mixer [4]. It can easily happen that the I-Q mixer could be imbalanced, which means that I and Q signals coming out of the AWG are not equal in amplitude when they should be. Therefore, the calibration of π- and $\frac{\pi}{2}$-pulses is a fundamental step prior to fidelity measurements.

4.4.1 Calibration of the π and $\frac{\pi}{2}$ amplitude

In order to calibrate the amplitude of the π-pulse, we prepare the qubit in the ground state. Then, we send a sequence of an even number of π-pulses, as shown in Figure 4.13.

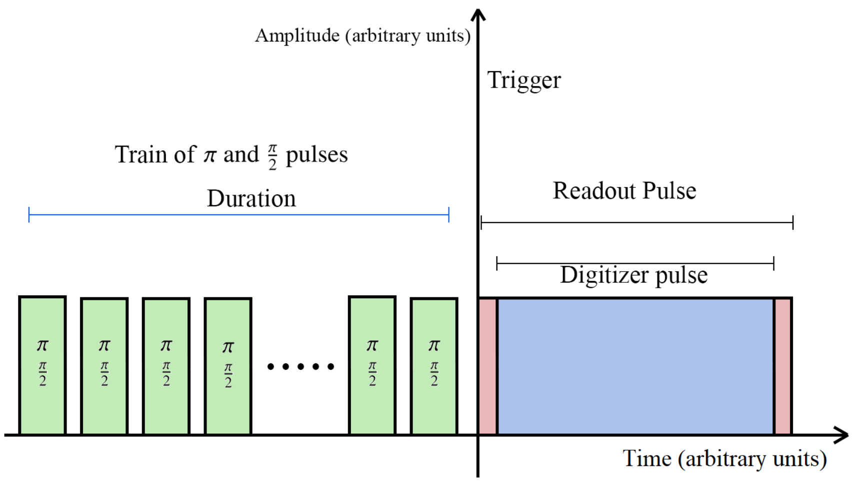

Figure 4.13: Pulse sequence for $V_{amp,\pi}$ and $V_{amp,\frac{\pi}{2}}$ optimization. $V_{amp,\pi}$ corrects the mismatch between the I and Q parts of the π-pulse signal and $V_{amp,\frac{\pi}{2}}$ corrects the amplitude of the $\frac{\pi}{2}$-pulse.

Ideally, 2n π-pulses should carry the qubit from the ground state to the excited state, and then again in the ground state. However, when increasing the number of π-pulses, the qubit may not return to the ground state, because of the unbalance between the I and Q drive signals. In particular, this happens both when the π-pulse amplitude is larger than the ideal one, or smaller. In order to find the optimal π-pulse amplitude, we start with 8 π-pulses as a function of a scaling parameter $V_{amp,\pi}$, which identifies the ratio between the I and Q signals. Then, we gradually increase the number of π pulses following an exponential trend.

As occurs for the π-pulse, a similar calibration is performed for correction of the $\frac{\pi}{2}$ pulse, which is derived from the π-pulse by halving the latter's amplitude. However, in order to return to the ground state, we need to use $\frac{\pi}{2}$ sequences which are multiples of four. In this case, the sweep parameter is the correction of π-pulse amplitude $V_{amp,\frac{\pi}{2}}$.

In both π and $\frac{\pi}{2}$ optimization sequences, we expect to find the qubit in the ground state. This means that, for the best $V_{amp,\pi}$ and $V_{amp,\frac{\pi}{2}}$, we should measure a constant voltage, corresponding to the ground state. By increasing the number of pulses in the train, we are essentially increasing our sensitivity to deviations from the optimal parameters. In fact, the train with less pulses can be used to narrow down the range of parameters to explore, while the longer trains give a preciser estimate of the correction parameters.

4.4.2 π and $\frac{\pi}{2}$ calibration through DRAG optimization techniques.

In addition to the correction of the π and $\frac{\pi}{2}$ pulses amplitude, we have also exploited what is known as DRAG (Derivative Reduction by Adiabatic Gate) pulse shaping [4].

Drive pulses are square wave-like with finite rise time, as shown in Figure 4.14, given by the minimum time of the AWGs generation (1 ns). Specifically, we implement a cosine rise. The duration of the signal is that of the π-pulse for each qubit. When ramping the pulse, the overshoot can be significantly enough to excite the first non-computational state $|2\rangle$. This behaviour is similar to what we discuss in Section 4.2, where we show that by increasing the power of the pulse we are able to observe higher order transitions in the qubit spectroscopy. It is also possible that there are higher harmonics in the signal, which go into resonance with the $|2\rangle$ state.

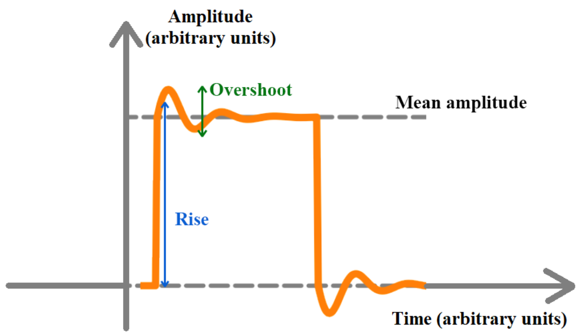

Figure 4.14: Example of square wave-like pulse generated by the AWG with a finite rise time and overshoot due to the limitations of the electronics.

These imperfections cause problems with the control of the qubit. Specifically, this unbalance causes under- or over-rotations on the Bloch sphere. In order to contrast this behaviour, which of course influences the gate performance of the qubit, the DRAG pulse shaping implements a correction on the drive signal in the following way:

$$\Omega^{'}(t) = \Omega(t) - i\alpha\frac{\dot{\Omega}(t)}{\Delta}, \tag{4.3}$$

where $\Omega(t)$ is the original pulse, α is known as DRAG scaling factor and Δ is the qubit anharmonicity. The effect of α on Eq. 2.51 is to vary both the fidelity and the SPAM errors. An example of this study is given in [63], where the predominant SPAM error is the leakage, i.e. the involvement of higher transitions like $|1\rangle \leftrightarrow |2\rangle$ transition.

When trying to implement the DRAG scheme with only α, the results in Figure 4.15 show that there are different sweet spots for the fidelity and the leakage.

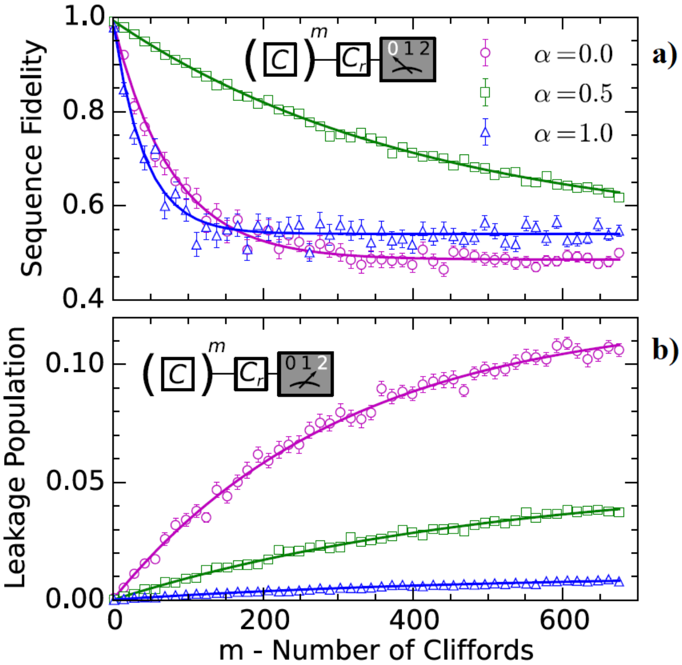

Figure 4.15: Example of the effect of DRAG correction on the fidelity and the leakage error [63]. We can reduce the leakage errors by increasing α to 1, but this does not amount to the best fidelity possible, which is obtained at intermediate α (0.5).

$\alpha = 1$ greatly reduces the leakage, but it makes the fidelity much poorer than for $\alpha = 0.5$. The motivation relies in the presence of phase errors, which may shift the $|1\rangle \leftrightarrow |2\rangle$ transition due to repulsion between the two levels, similarly to an AC-Stark shift [63]. Due to the repulsion of the $|1\rangle$ and $|2\rangle$ levels, a small shift in the frequency of the qubit arises, which detunes it from the QD frequency and causes dephasing [63]. This behaviour could be corrected by adding a detuning pulse:

$$\Omega^{''}(t) = \Omega^{'}(t)e^{2\pi i\delta f t}. \tag{4.4}$$

This signal redefines the anharmonicity to:

$$\Delta = \omega_{21} - (\omega_{10} + 2\pi\delta f). \tag{4.5}$$

The results of this approach in [63] are shown in Figure 4.16. Without the detuning correction, we must find a trade-off that minimizes both the phase and leakage errors. When the detuning correction is applied, we become insensitive to phase errors and we only correct for leakage. Even though the use of a detuning correction increases the fidelity performance for all α and allows to choose the sweet spot for the leakage, the error per Clifford is still limited by the coherence of the qubit, so the improvement in overall fidelity from leakage reduction is not so big [63]. In this thesis, we have chosen to optimize only the scaling parameter α.

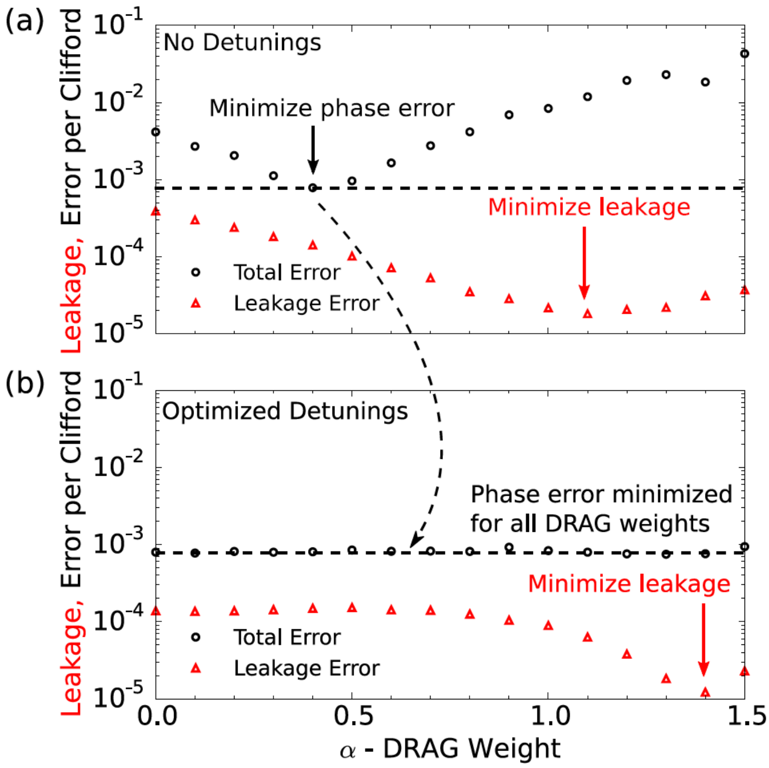

Figure 4.16: Total gate fidelity and leakage rates versus DRAG weighting α, measured using RB. In **a)** there is only the α correction, whereas in **b)** there is also the correction on Δ. The detuning pulse can improve the optimization of the fidelity and the leakage errors [63].

The DRAG scaling factor optimization in this thesis is provided by the **AllXY** technique. The AllXY technique is based on the implementation of gate sequences made of X_π, Y_π, $X_{\frac{\pi}{2}}$, $Y_{\frac{\pi}{2}}$. The error accumulated after the application of two of these pulses depends on both the DRAG scaling factor and the DRAG detuning. The matrix describing the rotation of a qubit by an angle θ about the axis $\hat{\sigma}$ is given by:

$$\hat{U}(\theta, \hat{\sigma}) = e^{-i\frac{\theta}{2}\hat{\sigma}} \tag{4.6}$$

In the first column of Table 2 we show the ideal state of arrival for the sequence [64]. The second and third columns show the first and second pulse in the tested sequence. In the fourth column of Table 2 we show the power error for the sequences. An error in pulse power by x dB is correctly captured by Eq. 4.6 by scaling θ by a factor of $10^{\frac{x}{20}}$, because of the logarithmic units [64]. In the fifth column we show the detuning error, which is understood as an additional z field to $\hat{\sigma}$ (longitudinal noise). It is clear from the study in [64] that different sequences introduce not only a different scaling of the error, but also different signs (positive or negative).

The protocol to find the optimal α parameter in the DRAG scheme uses these four sequences: $\left(X_\pi - X_{\frac{\pi}{2}}\right)$ $\left(X_\pi - Y_{\frac{\pi}{2}}\right)$, $\left(Y_\pi - X_{\frac{\pi}{2}}\right)$ $\left(Y_\pi - Y_{\frac{\pi}{2}}\right)$. For the $\left(X_\pi - X_{\frac{\pi}{2}}\right)$ and $\left(Y_\pi - Y_{\frac{\pi}{2}}\right)$

Ideal $\langle z \rangle$	First pulse	Second pulse	Power dependence	Detuning dependence
1	Id	Id	1	1
1	$X(\pi)$	$X(\pi)$	$1-8\epsilon^2+\mathcal{O}(\epsilon^4)$	$1-\frac{\pi^2\epsilon^4}{32}+\mathcal{O}(\epsilon^6)$
1	$Y(\pi)$	$Y(\pi)$	$1-8\epsilon^2+\mathcal{O}(\epsilon^4)$	$1-\frac{\pi^2\epsilon^4}{32}+\mathcal{O}(\epsilon^6)$
1	$X(\pi)$	$Y(\pi)$	$1-4\epsilon^2+\mathcal{O}(\epsilon^4)$	$1-\epsilon^2+\mathcal{O}(\epsilon^3)$
1	$Y(\pi)$	$X(\pi)$	$1-4\epsilon^2+\mathcal{O}(\epsilon^4)$	$1-\epsilon^2-\mathcal{O}(\epsilon^3)$
0	$X(\pi/2)$	Id	$-\epsilon+\mathcal{O}(\epsilon^3)$	$(1-\frac{\pi}{2})\epsilon^2-\mathcal{O}(\epsilon^4)$
0	$Y(\pi/2)$	Id	$-\epsilon+\mathcal{O}(\epsilon^3)$	$(1-\frac{\pi}{2})\epsilon^2-\mathcal{O}(\epsilon^4)$
0	$X(\pi/2)$	$Y(\pi/2)$	$\epsilon^2-\mathcal{O}(\epsilon^4)$	$-2\epsilon+\mathcal{O}(\epsilon^3)$
0	$Y(\pi/2)$	$X(\pi/2)$	$\epsilon^2-\mathcal{O}(\epsilon^4)$	$2\epsilon-\mathcal{O}(\epsilon^3)$
0	$X(\pi/2)$	$Y(\pi)$	$\epsilon-\mathcal{O}(\epsilon^3)$	$-\epsilon-\mathcal{O}(\epsilon^2)$
0	$Y(\pi/2)$	$X(\pi)$	$\epsilon-\mathcal{O}(\epsilon^3)$	$\epsilon-\mathcal{O}(\epsilon^2)$
0	$X(\pi)$	$Y(\pi/2)$	$\epsilon-\mathcal{O}(\epsilon^3)$	$-\epsilon-\mathcal{O}(\epsilon^2)$
0	$Y(\pi)$	$X(\pi/2)$	$\epsilon-\mathcal{O}(\epsilon^3)$	$\epsilon-\mathcal{O}(\epsilon^2)$
0	$X(\pi/2)$	$X(\pi)$	$3\epsilon-\mathcal{O}(\epsilon^3)$	$\frac{3\pi\epsilon^2}{8}+\mathcal{O}(\epsilon^4)$
0	$X(\pi)$	$X(\pi/2)$	$3\epsilon-\mathcal{O}(\epsilon^3)$	$\frac{3\pi\epsilon^2}{8}+\mathcal{O}(\epsilon^4)$
0	$Y(\pi/2)$	$Y(\pi)$	$3\epsilon-\mathcal{O}(\epsilon^3)$	$\frac{3\pi\epsilon^2}{8}+\mathcal{O}(\epsilon^4)$
0	$Y(\pi)$	$Y(\pi/2)$	$3\epsilon-\mathcal{O}(\epsilon^3)$	$\frac{3\pi\epsilon^2}{8}+\mathcal{O}(\epsilon^4)$
-1	$X(\pi)$	Id	$-1+2\epsilon^2+\mathcal{O}(\epsilon^4)$	$-1+\frac{\epsilon^2}{2}+\mathcal{O}(\epsilon^4)$
-1	$Y(\pi)$	Id	$-1+2\epsilon^2+\mathcal{O}(\epsilon^4)$	$-1+\frac{\epsilon^2}{2}+\mathcal{O}(\epsilon^4)$
-1	$X(\pi/2)$	$X(\pi/2)$	$-1+2\epsilon^2+\mathcal{O}(\epsilon^4)$	$-1+2\epsilon^2+\mathcal{O}(\epsilon^4)$
-1	$Y(\pi/2)$	$Y(\pi/2)$	$-1+2\epsilon^2+\mathcal{O}(\epsilon^4)$	$-1+2\epsilon^2+\mathcal{O}(\epsilon^4)$

Table 2: These are all the possible two-pulse combination. The first column shows the ideal state of arrival in the σ_z basis. The second column is the first pulse and the third column is the second pulse. The fourth and fifth column represent the amplitude and the detuning dependence of the error, respectively [64].

pulses the detuning error dependence is of the second order and of the same sign. For the $\left(X_\pi - Y_{\frac{\pi}{2}}\right)$ and $\left(Y_\pi - X_{\frac{\pi}{2}}\right)$ pulses, instead, the detuning error dependence follows a linear trend with a slope that depends on the error sign.

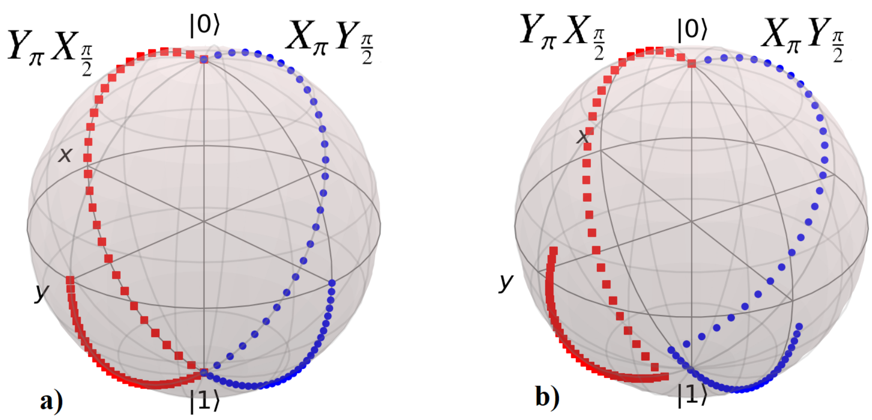

Figure 4.17: In **a)** we show the ideal gate sequences $\left(X_\pi - Y_{\frac{\pi}{2}}\right)$ and $\left(Y_\pi - X_{\frac{\pi}{2}}\right)$. In **b)** we show the gate sequence $\left(X_\pi - Y_{\frac{\pi}{2}}\right)$ and $\left(Y_\pi - X_{\frac{\pi}{2}}\right)$ when there is noise causing detuning error dependece. This graphs have been simulated using the *mesolve* method of *QuTiP* [65].

The effect of the detuning error on the qubit arrival state after a $X_\pi Y_{\frac{\pi}{2}}$ (blue curve) and $Y_\pi X_{\frac{\pi}{2}}$ (red curve) has been simulated in Figure 4.17. In the ideal case of no longitudinal noise ($\epsilon = 0$), the arrival state of the two sequences is predicted to lead the qubit on the equator of the Bloch sphere (Figure 4.17a)). When longitudinal noise cannot be neglected, the detuning error dependence for the sequence $X_\pi Y_{\frac{\pi}{2}}$ ($Y_\pi X_{\frac{\pi}{2}}$) is negative (positive), causing an undershoot (overshoot) on the final qubit state. The DRAG calibration procedure has the aim to correct the behaviour in Figure 4.17b so that the system behaves as Figure 4.17a. The protocol used to send the pulses is reported in Figure 4.18. After the preparation of the qubit state in the ground state, we apply a $\left(X_\pi - Y_{\frac{\pi}{2}}\right)$ pulse sequence and we measure the state as a function of the drag scaling factor. Since $\left(X_\pi - Y_{\frac{\pi}{2}}\right)$ sequence

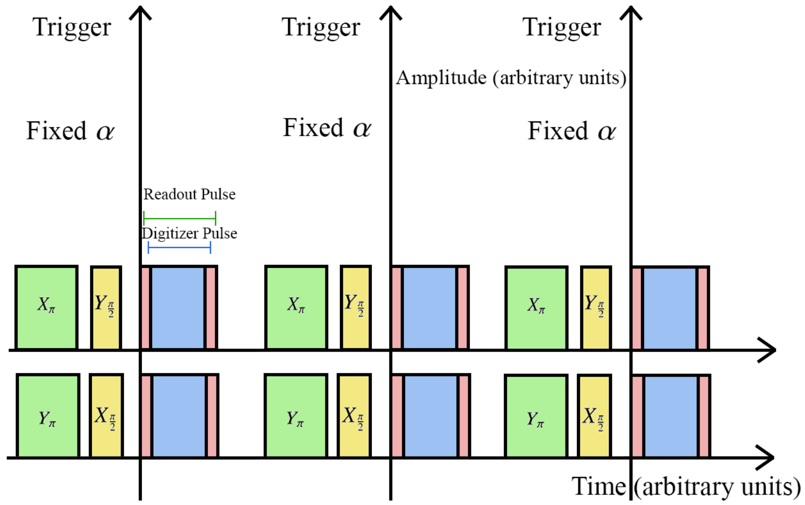

Figure 4.18: Example of the protocol used for DRAG scaling calibration. After every *Trigger period* we change the α parameter and measure the real and imaginary parts of the signal.

introduces a negative sign in the error dependence on the scaling factor amplitude, the sequence gives a negative slope in the readout voltage as a function of the scaling factor. If we instead apply $\left(Y_\pi - X_{\frac{\pi}{2}}\right)$, the error sign is positive and the sequence gives a positive slope. Therefore, this measurement provides us with two distinct curves for $\left(X_\pi - Y_{\frac{\pi}{2}}\right)$ and for $\left(Y_\pi - X_{\frac{\pi}{2}}\right)$ as shown in Figure 4.19. The two sequences have opposite slopes and the optimal operational point is where these two curves intersect. This is the best compromise between sequences with opposite sign error. At the intersection point both pulses are not perfectly tuned, but, since their errors are of opposite signs, we expect them to cancel each other.

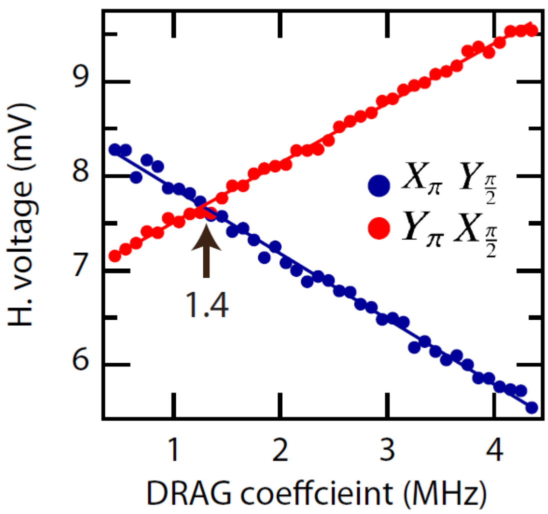

Figure 4.19: Calibration of the DRAG coefficient α by using AllXY technique. The expected state on the equator of the Bloch sphere will be designated by a certain voltage, so by changing α we are changing the arrival state of the qubit. When the two lines cross, we find the optimal α for the DRAG scheme [64]. Figure adapted from [64].

4.5 Randomized Benchmarking

Once the correction parameters for π and $\frac{\pi}{2}$ pulses are implemented, Randomized Benchmarking (RB) test is performed. The RB sequence is reported in Figure 4.20. We initialize the qubit in the ground state. Then we send a sequence of Clifford gates and its inverse gate, so that the final state of the qubit theoretically matches with the initial one. Then we measure in what state the qubit is found. The fidelity of RB is the measure of how often we return to the initial state. We repeat this measurement by increasing the number of Clifford gates in the sequence. As shown in Section 2.8, by increasing the number of Clifford gates the probability to accumulate errors in the sequence increases.

Clifford gates in the sequence are generated randomly, chosen by a pseudo-random seed. By changing the pseudo-random seed, we acquire multiple traces, which are averaged in order to extrapolate the qubit fidelity, as shown in Eq. 2.51.

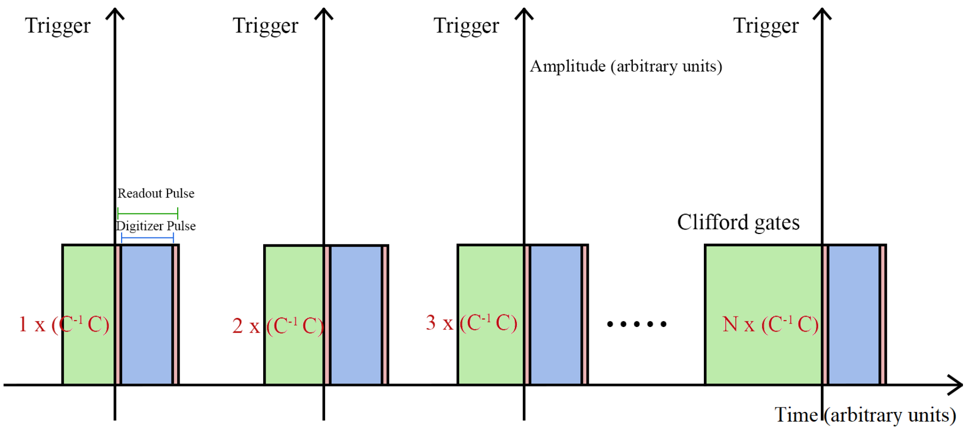

Figure 4.20: Sequence used for RB. The number of Clifford gates (C) and their inverse (C^{-1}) is increased with every step.

In the ideal case of perfectly coherent qubits and unitary Clifford gates with no SPAM errors, the outcome of this experiment should be a constant readout voltage related to the initial state of the qubit when increasing the number of Clifford gates. In reality, the applied inverse might not be the exact inverse of the Clifford gate. Also, the qubit is not perfectly coherent, so both these factors contribute to get as a result a state different from the initial one. An example of this behaviour is shown in Figure 4.21 [30].

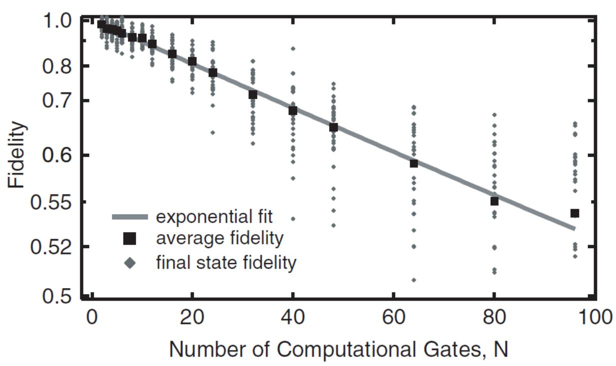

Figure 4.21: Average fidelity as a function of the number of applied computational gates. Computational gates consist of a randomized Clifford generator [30].

The exponential decay obtained through fidelity measurement (Figure 4.21) can be fitted by Eq. 2.51, which can be simplified as follows [66]:

$$F_N = A + Bp^N, \tag{4.7}$$

where p is responsible of the exponential decay and gives an estimate of the polarizing error, A in Eq. 4.7 corresponds to $(1-\alpha_n)$ in Eq. 2.51 and B corresponds to $\alpha_n\left(1-\frac{\epsilon_m}{\alpha_n}\right)$.

In Section 2.8 we showed that the average fidelity related to the imperfect realization of a Clifford gate Λ is given by $F_{avg} = 1-r$, with r representing the average error committed in the sequence. The depolarizing errors mentioned in Section 2.8 can be expressed through Λ_{dep} [67], which is the imperfect realization of the Clifford gates due to depolarization. In [67] they find that all the errors are due to depolarization, so we can equate the average fidelity due to Λ and the fidelity due to Λ_{dep}. For this reason p and r are related by [67]:

$$r = 1 - p - \frac{1-p}{d}. \tag{4.8}$$

By finding the fit parameter p, we are able to estimate the avarage fidelity as:

$$F_{avg} = p + \frac{1-p}{d} \tag{4.9}$$

4.6 iSWAP gate

The next logic step is to study how two qubits interact. Specifically, in this thesis we have investigated two coupled qubits, qubit 0 and qubit 2 (see Section 3.1 for further details). We are going to show how to put qubits 0 and 2 on resonance with each other, as described in Section 2.9, and how to evaluate if there is a swap of energy in the form of the iSWAP gate, which we described in Section 2.10.

First we tune the frequency of qubit 2, which in our chip is the the high-frequency qubit with its flux line, and we perform a qubit spectroscopy on qubit 2.

The avoided level crossing occurs when qubit 2 frequency is on resonance with the low-frequency qubit, which in our chip corresponds to qubit 0. This qubit is kept fixed in frequency during all the measurement. Hence, the range of flux that we investigate corresponds to the values for which qubit 2 has a frequency close to qubit 0.

Once found the avoided level crossing region, we apply a flux voltage pulse on qubit 2 by changing the amplitude and the duration of the pulse. The amplitude is chosen so to be in the avoided level crossing region. In this measurement, we readout simultaneously qubits 0 and 2. The protocol used to send the flux signal is shown in Figure 4.22.

Simultaneous readout uses two signals through the feedline, which need to satisfy the following relation:

$$\begin{cases} \omega_{r,0}^{(LO)} - \omega_{r,0}^{(IF)} = \omega_{r,0}^{(RF)} \\ \omega_{r,2}^{(LO)} - \omega_{r,2}^{(IF)} = \omega_{r,2}^{(RF)} \end{cases} \tag{4.10}$$

where $\omega_{r,0}^{(IF)}$ and $\omega_{r,2}^{(IF)}$ are the intermediate frequency signals from the AWG, $\omega_{r,0}^{(LO)}$ and $\omega_{r,2}^{(LO)}$ are the local oscillator signals and $\omega_{r,0}^{(RF)}$ and $\omega_{r,2}^{(RF)}$ are the frequencies used to resonate with the readout resonators of the two qubits. Since all the readout resonators are

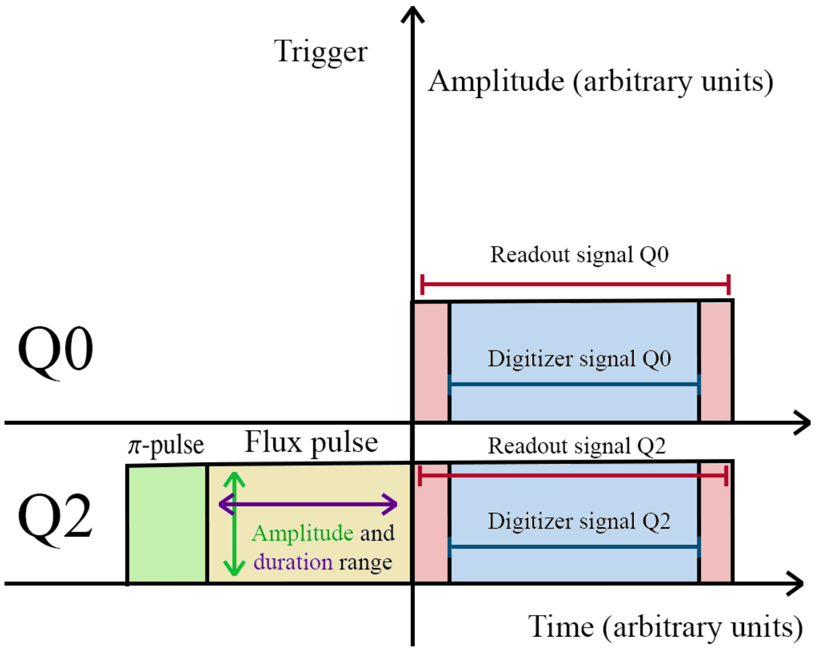

Figure 4.22: Sequence used to enable the energy swap between qubits 0 and 2. Through a π-pulse we prepare qubit 2 in the $|1\rangle$ state. The swap consists in the oscillation between $|01\rangle$ and $|10\rangle$. We vary the the amplitude and duration of the flux pulse and we use two readout pulses for qubits 0 and 2 in accordance with Eq. 4.10.

capacitively coupled to the same feedline, we are indeed able to perform multiplexing readout. This motivates the chip design discussed in Section 3.1.

We fix the local oscillator frequencies such that $\omega_{r,0}^{(LO)} = \omega_{r,2}^{(LO)} = \omega_r^{(LO)}$. $\omega_{r,0}^{(IF)}$ and $\omega_{r,2}^{(IF)}$ frequencies must satisfy Eq. 4.10 in order to read the two qubits simultaneously. The diagram of this measurement is shown in Figure 4.22.

5 Experimental results and Data Analysis

In this Chapter we will focus on the characterization of the qubits labeled as 0 and 2 in Figure 3.1. In Section 5.1 we study the readout resonators coupled to these qubits. In Section 5.2 single-qubit spectroscopy is reported. In Section 5.4 we will explore time-domain characterization, which provides the π-pulse duration, T_1 and T_2. Then we will show in Section 5.5 how to optimize the pulses used in single-qubit Randomized Benchmarking (RB), which we analyze in Section 5.6. Finally, we discuss the avoided level crossing in Section 5.7 with possible future implementations.

5.1 Coupling resonator spectroscopy

In Section 4.1 we explained how resonator spectroscopy is performed. Now we present our results for the readout resonators coupled to the two qubits. Let us begin with the readout resonator labeled as Cavity 2 which is coupled to qubit 0.

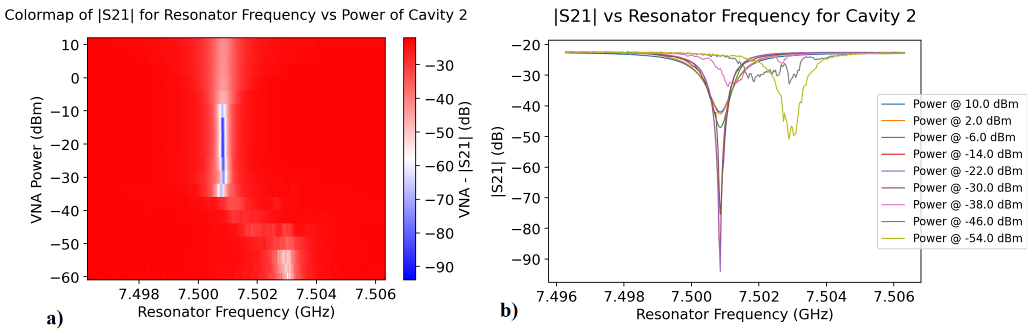

Figure 5.1: a) Cavity 2 dispersive shift colormap: on the y-axis, VNA input power in dBm, on the x-axis resonator tone frequency. The color scale identifies the magnitude of the readout S_{21} output. In **b)** comparison of the magnitude of the S_{21} output for different VNA input power.

In Figure 5.1a we report the transmission magnitude S_{21} as a function of the input power of the VNA. We observe a dip when the readout tone resonates with the resonator, following the protocol reported in Section 5.1. We can clearly notice a shift from the *bare* state of the resonator at higher powers to the low photon regime at lower powers. Line-cuts for different input powers are reported in Figure 5.1b. The bare state occurs when we send enough power to the qubit (in this case qubit 0) to saturate the transitions from $|0\rangle$ to $|1\rangle$, thus decoupling the resonator from its qubit, as discussed in Section 2.5.1. When the power is low enough, the dispersive regime is recovered.

In order to evaluate the dispersive shift, we fit the experimental data representing the bare state and the low photon regime. We use the Python library *resonator tools* [68] to fit the resonances and extrapolate all the relevant parameters (quality factors, resonance frequency, respective errors). In Figure 5.2 we show the results of our fits for Cavity 2 in the bare state (10 dB) and the low photon regime (-58 dB).

The resonance frequency in the two states are $\omega_{r,bare} = 7.50088 \pm 0.00005\, GHz$ and $\omega_{r,lphr} = 7.50299 \pm 0.00003\, GHz$, where the errors provided by resonator tools are statistical errors. The experimental bare resonator frequency is nearly 300 MHz larger than the designed resonator frequency of 7.20GHz. This can be attributed to defects in the fabrication, but as long as its frequency does not overlap with the resonances of other resonators, it does not cause simultaneous excitation of more than one resonator. Using this data, we can calculate the dispersive shift $\chi = 2.11 \pm 0.08\ MHz$. The error on χ is obtained from that of the resonance frequencies by propagation of statistical errors.

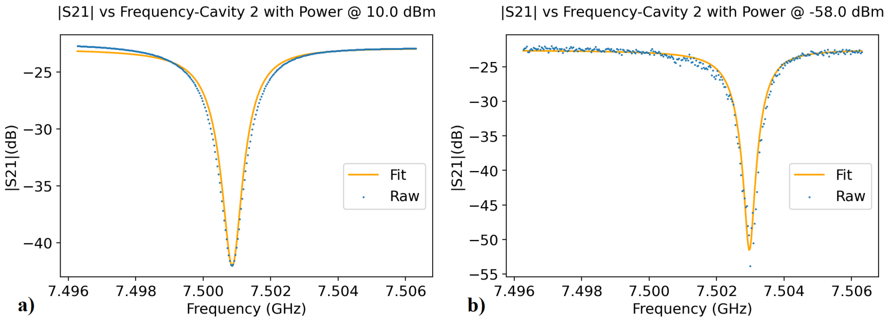

Figure 5.2: Cavity 2 fit in the bare (VNA input power = 10 dBm) **a)** and dressed (VNA input power = - 58 dBm) states **b)** performed with resonator tools Python package [68].

The fit allows also to give an estimate of the quality factors of the readout resonator as shown in Table 3 (Section 3.1).

	Bare	**Low Photon Regime**
Resonance Frequency (GHz)	7.50088 ± 0.00005	7.50299 ± 0.00003
$\mathbf{Q_i}$	$15 \pm 5 \cdot 10^3$	$30 \pm 5 \cdot 10^3$
$\mathbf{Q_c}$	$9.4 \cdot 10^3$	$9.1 \cdot 10^3$
$\mathbf{Q_l}$	$5.8 \pm 0.7 \cdot 10^3$	$7.0 \pm 0.3 \cdot 10^3$

Table 3: We give the loaded (total) quality factor (Q_l), the coupling quality factor (Q_c) and the internal quality factor (Q_i) of Cavity 2 from the fit with resonator tools. The errors in this table are obtained from resonator tools and are of the statistical type.

The intrinsic quality factor Q_i, the coupling quality factor Q_c and the total quality quality factor Q_l are related by the relation:

$$\frac{1}{Q_l} = \frac{1}{Q_i} + \frac{1}{Q_c} \tag{5.1}$$

Q_c takes into account how well the resonator couples to the rest of the system, Q_i give us an idea of all the possible losses in the resonator. In our case, the internal quality factor Q_i is much higher than the coupling quality factor Q_c, so the resonator is not limited by internal losses. In the case of niobium compounds superconducting resonators, these numbers comply with the literature [69] and allow to perform the readout of the qubit state.

We perform the same investigations for readout resonator labeled as Cavity 4, which is coupled to qubit 2. We show in Figure 5.3 the resonator spectroscopy, performed by varying the power of the VNA input signal, where Cavity 4 exhibits the expected dispersive shift. To evaluate it, we fit the resonances in the bare state (10 dB) and in the low photon regime (−60 dB), as shown in Figure 5.4. The fit provides us the resonance frequencies in the two states, which are $\omega_{r,bare} = 7.661144 \pm 0.000005\ GHz$ and $\omega_{r,lphr} = 7.665630 \pm 0.000007\ GHz$. The dispersive shift is $\chi = 4.49 \pm 0.01\ MHz$.

When we compare the readout resonators of qubits 0 and 2, the dispersive shift of Cavity 4 is twice as big. In the hypothesis of similar coupling factors g, which holds if we

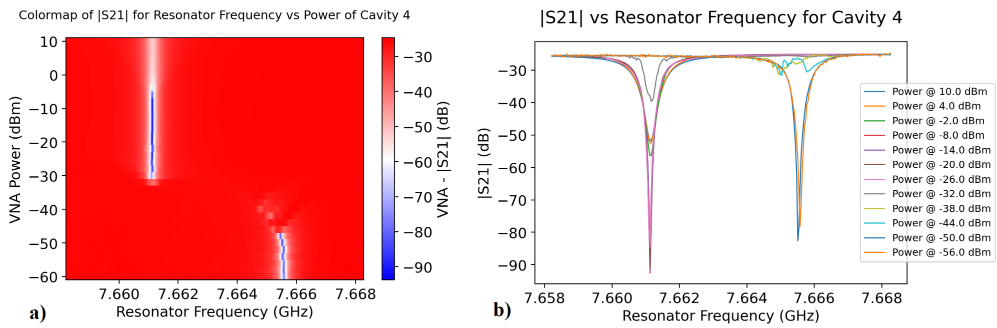

Figure 5.3: In **a)** Cavity 4 dispersive shift colormap: on the y-axis, VNA input power in dBm, on the x-axis resonator tone frequency. The color scale identifies the magnitude of the readout S_{21} output. In **b)** comparison of the magnitude of the S_{21} output for different VNA input power.

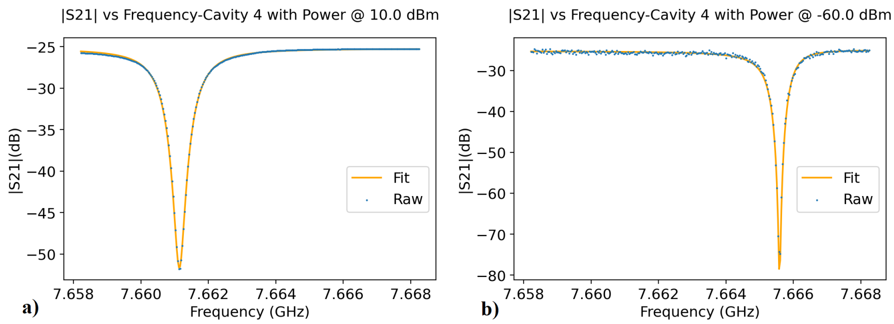

Figure 5.4: Cavity 4 fit in the bare (VNA input power = 10 dBm) **a)** and dressed (VNA input power = - 60 dBm) states **b)** performed with resonator tools Python package[68].

consider that the two resonators are fabricated within the same conditions, the larger dispersive shift can be attributed to smaller detuning for Cavity 4 compared to Cavity 2. More favourable outcome of the limiting manufacturing tolerances leads also to better coupling and less losses for Cavity 4 compared to Cavity 2.

	Bare	Low Photon Regime
Resonance Frequency (GHz)	7.661144 ± 0.000005	7.665630 ± 0.000007
Q_i	$26.3 \pm 0.7 \cdot 10^3$	$15 \pm 3 \cdot 10^4$
Q_c	$9.6 \cdot 10^3$	$9.9 \cdot 10^3$
Q_l	$7.00 \pm 0.05 \cdot 10^3$	$9.30 \pm 0.15 \cdot 10^3$

Table 4: Loaded (total) quality factor (Q_l), the coupling quality factor (Q_c) and the internal quality factor (Q_i) of Cavity 4 from the fit with resonator tools [68]. The errors in this table are obtained from resonator tools and are of the statistical type.

We can now focus on the flux dependence of the resonance frequency of the two readout resonators, which is found in $\tilde{\omega}_r = \omega_r + \chi(\Phi)$. Recalling the flux dependence of the qubit frequency in Eq. 2.40 and the dispersive shift in Eq. 2.16, we expect the resonator resonance frequency to modulate with the flux as:

$$\chi = \frac{g^2}{\Delta} = \frac{g^2}{\left|\sqrt{8E_C E_J \left|\cos\left(\frac{\pi\Phi}{\Phi_0}\right)\right|} - \omega_r\right|} \tag{5.2}$$

This relation suggests a behaviour similar to the one found in Figure 2.18. The results we have obtained are shown in Figure 5.5.

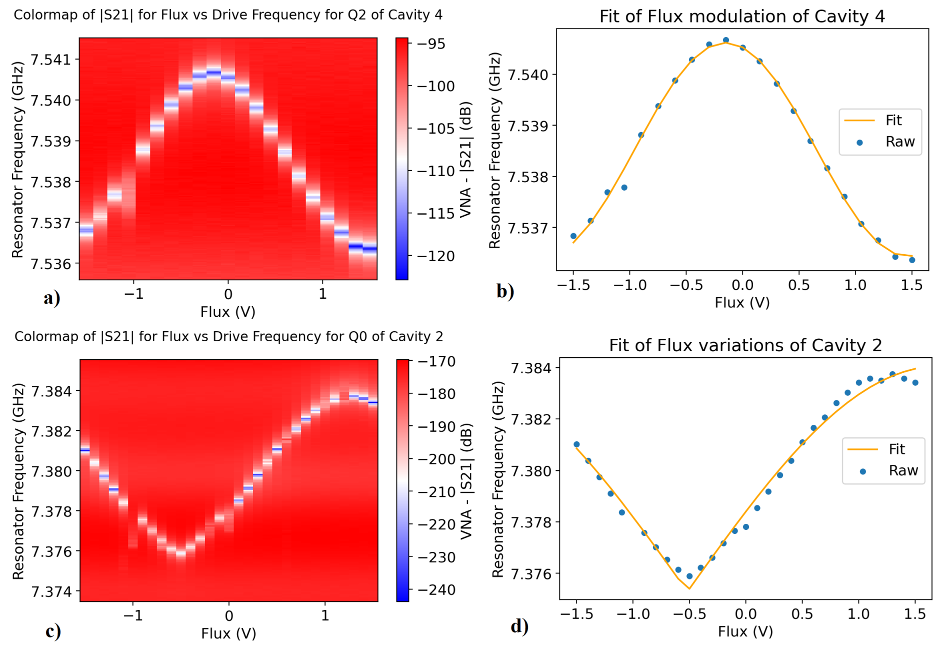

Figure 5.5: a) Flux modulation of Cavity 4 resonance frequency coupled to qubit 2: the x-axis is the voltage applied across the flux line, the y-axis is the resonator frequency, the color scale identifies the magnitude of the S_{21} output. In **b)** we extrapolate the modulation and fit the curve with a cosine. In **c)**, flux modulation of the Cavity 2 resonance frequency coupled to qubit 0: the x-axis is the voltage applied across the flux line, the y-axis is the resonator frequency, the color scale identifies the magnitude of the S_{21} output. In **d)** the fit of the extrapolated curve.

We see from Figure 5.5a that one flux period corresponds to approximately 3 V applied across the flux line of qubit 2. In order to give a quantitative estimate, we extrapolate the modulation and fit it with a cosine function, obtaining a period of $T = 3.22 \pm 0.06\ V$. We have used the Python library *lmfit* [70] for the fit in Figure 5.4 as for most of the fits in this thesis. The errors are given by Non-Linear Least-Squares Minimization. While in Eq. 5.2 the external flux is given in weber (Wb), we use its equivalent in volts in Figures 5.4a and 5.4c. Stainless steel flux lines in our cryostat have a total resistance of the order of 50 Ω considering also the presence of low-pass filters of 1 GHz anchored at the MC plate. This implies that a current $I = V \cdot 50\,\Omega$ flows in the flux lines on chip. According to the Ampère law, this generates a concatenated magnetic flux $\Phi(B)$ orthogonal to the surface of the qubit DC-SQUID. Therefore, the relation between the voltage applied and the flux satisfies: $\Phi = \frac{LV}{R}$, where L is the inductance of the DC-SQUID in the qubit.

The behaviour of Cavity 2 is similar (Figure 5.4c). Nevertheless, the fit is not quite perfect, which is mainly because we are not able to clearly distinguish the maximum of the modulation (this is a limitation of the experimental setup, which can supply up to 1.5 V). We would need more points across a wider flux range for the fit to be more precise. From Figure 5.4c we expect a period of around 4 V and with the fit shown in Figure 5.4d we obtain $T = 4.5 \pm 0.2\ V$.

A very important feature of these measurement regards multiplexing. As explained in Section 3.1, we want the frequency of the readout resonators to be close, but also not too close to each other in order not to overlap. From the measurements in this Section we have clearly demonstrated that, when working in the dispersive regime, the frequencies of Cavities 2 and 4 are sufficiently far from each other, even when a magnetic field flux is applied. This is crucial when we perform a two-qubit gate in Section 6, where a simultaneous readout is necessary and we employ the multiplexing capabilities of our system.

5.2 Qubit spectroscopy

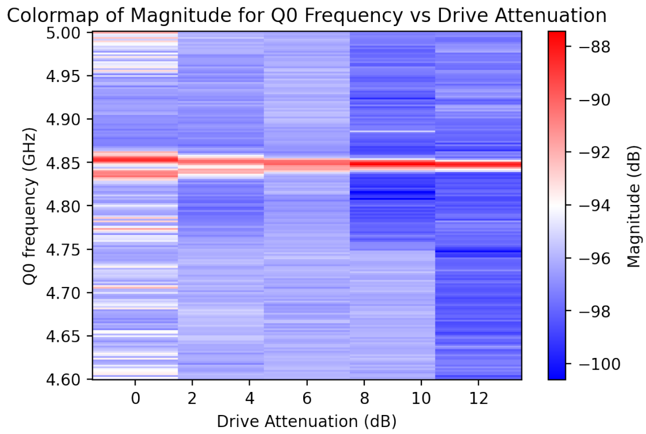

Figure 5.6: Qubit 0 spectroscopy: on the y-axis, the qubit drive Q0 frequency, the x-axis is the attenuation of the qubit drive signal, the color scale identifies the demodulated voltage magnitude in dB of the readout resonator.

On the basis of the arguments given in Section 4.2, we discuss the experimental results of qubit spectroscopy. This measurement give a first estimate of the qubit transition frequencies. In Figure 5.6 we show the magnitude of the demodulated output readout voltage as a function of the qubit drive frequency and the qubit drive power applied across a dedicated drive line for qubit 0. We apply 1.3 V on the flux line of qubit 0 to put it at its flux sweet spot.

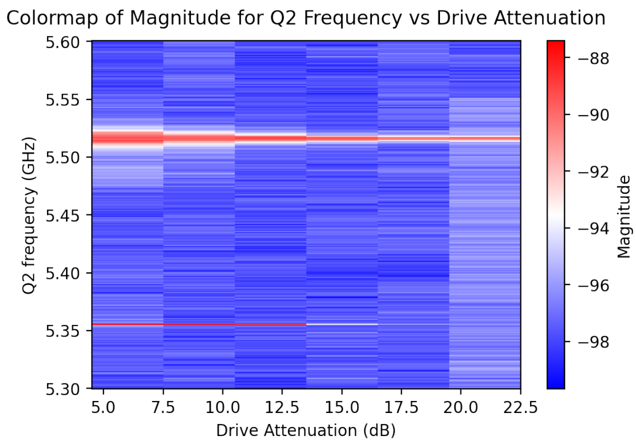

Figure 5.7: Qubit 2 spectroscopy: on the y-axis, the qubit drive Q2 frequency, the x-axis is the attenuation of the qubit drive signal, the color scale identifies the demodulated voltage magnitude in dB of the readout resonator.

We only observe the fundamental transition $|0\rangle \rightarrow |1\rangle$, since the power sent to the qubit is not high enough to excite the $|0\rangle \rightarrow |2\rangle$ transition. A rough estimation of the qubit frequency obtained through qubit spectroscopy is $4.846 \pm 0.002\ GHz$. The errors from qubit spectroscopy are maximum errors. A more precise method is through Ramsey interferometry, as shown in Section 5.4.2. When increasing the qubit drive power, the broadening of the transition increases. This is related to the increasing number of photons in the system, which increases the loss mechanisms.

Qubit spectroscopy for qubit 2 is reported in Figure 5.7. A rough estimation of the qubit frequency with -0.15 V applied on the flux line is $5.517 \pm 0.002\ GHz$. For this qubit, we can clearly distinguish two peaks. The higher-frequency one corresponds to the $|0\rangle \rightarrow |1\rangle$ transition. Increasing the qubit drive power, this transition becomes less pronounced, while the lower-frequency peak becomes stronger and broader. This peak corresponds to the $|0\rangle \rightarrow |2\rangle$ transition. This allows to extrapolate the anharmonicity as $\alpha = \omega_{01} - \omega_{12}$ and we obtain $\alpha = 322 \pm 4\ MHz$, where the error is a maximum error. The anharmonicity by design is $\alpha = 270 \pm 30\ MHz$, where the error accounts for a 10 % tolerance on E_C, as discussed in more detail in Section 5.3.

From Figures 5.6 and 5.7 we observe the $|0\rangle \rightarrow |2\rangle$ transition for qubit 2, but not for qubit 0. A key role is played by the coupling between the dedicated drive line and the qubit. It is plausible that the qubit-drive line coupling for qubit 0 is not as strong as for qubit 2. For this reason, rather than attenuate the qubit drive signal, we should amplify it at room-temperature in order to observe the $|0\rangle \rightarrow |2\rangle$ transition.

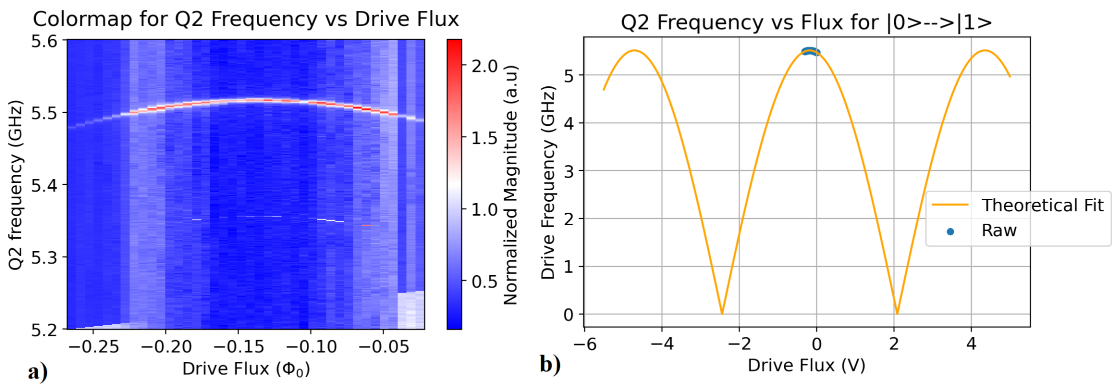

Figure 5.8: Flux spectroscopy of qubit 2. **a)** Colorplot with x-axis the flux on Q2, y-axis the Q2 drive frequency signal, and the color scale the normalized magnitude in a.u. of the readout resonator. **b)** Fit of the qubit frequency ω_{01} extrapolated from **a)**.

As discussed in Sections 2.9 and 4.6, two-qubit gates require that the two coupled qubits must be set on resonance by means of a flux tuning. Single-qubit spectroscopy measurements confirmed that qubit 0 is the lowest frequency qubit in the pair, as expected from the device specifications. Therefore, qubit 0 will be fixed thorough every two-qubit experiments at its sweet-spot (see Section 2.9), while qubit 2 will be flux-tuned towards qubit 0. Hence, qubit 2 spectroscopy as a function of the flux field for a fixed QD attenuation is a crucial step (Figure 5.8). From the theoretical fit, in accordance with Eq. 2.40, we can extrapolate the period $T = 4.492 \pm 0.003\ V$, where the errors are statistical. This result is in agreement with the fit of the period of Cavity 4. This experiment also allows to find the sweet spot of the qubit, i.e. where the derivative of the cosine is zero and it is at $-0.1759 \pm 0.0002\ V$ where errors are statistical. As for qubit 0, Cavity 2 spectroscopy as a function of the flux in Figure 5.4c suggested that the sweet-spot for qubit 0 falls in a range of flux-voltages close to the maximum resolution of our experimental set-up, thus preventing qubit 0 spectroscopy as a function of the flux. Nevertheless, as mentioned in Section 2.7, we want the qubits to be in their flux sweet spot when possible. In this way we minimize flux fluctuations and this definitely benefits the coherence times of the qubit.

5.3 Summary and comparison with design parameters

On the basis of the presented experimental outcomes, we are able to extract many of the characteristics of our chip and compare them to the expected ones by design. In Table 5 we compare the design characteristics with those calculated from the measurements. In order to calculate the charging energy, we use the approximation $E_C \approx -\alpha$ [9]. Since we did not observe the $|0\rangle \rightarrow |2\rangle$ transition for qubit 0, 2e will use for qubit 0 a value for E_C close to the one obtained for qubit 2, since E_C is designed to be similar for all the qubits on chip.

We can calculate E_J by applying 2.40. From this we are able to calculate the $\frac{E_J}{E_C}$ and establish whether we are in the low charge noise regime. We assume the same experimental error for qubit 0 as for qubit 2, i.e. a maximum error of 4 MHz in accordance with Figure 5.7. The error for the theoretical results is obtained by supposing a 10 % error on E_C due to the capacitance C and a 10 % error on E_J due to the critical current I_c. We estimate a ratio $\frac{E_J}{E_C}$ of 37 $\pm$ 1 and 41 ± 1 for qubit 0 and qubit 2 respectively, while the expected values are 42 ± 8 and 60 ± 10. The $\frac{E_J}{E_C}$ ratio of qubit 2 is lower than the expected one, which is due to higher than expected anharmonicity and lower than expected Josephson energy. However, the $\frac{E_J}{E_C}$ ratio for qubit 0 is within errors, since the calculated Josephson energy is much closer to expected one. Despite not matching the design parameters within error for qubit 2, the fabrication process is capable of realising the intended designs, which enables the qubits to reach the $\frac{E_J}{E_C} \gg 1$ regime.

Design parameters			Qubit number	
			0	2
component	parameter	unit		
qubit	frequency (bare) T	*Hz*	4,700E+09	5,600E+09
	frequency (bare) R	*Hz*	4,846E+09	5,517E+09
	Ec (charging energy) T	*Hz*	2,700E+08	2,700E+08
	Ec (charging energy) R	*Hz*	*3,000E+08*	3,220E+08
	EJ T	*Hz*	1,144E+10	1,595E+10
	EJ R	*Hz*	*1,103E+10*	1,324E+10
read-out resonator	frequency (bare) T	*Hz*	7,200E+09	7,600E+09
	frequency (bare) R	*Hz*	7,501E+09	7,661E+09
	Chi (qubit-state dependend frequency shift) T	*Hz*	-1,191E+06	-7,371E+05
	Chi (qubit-state dependend frequency shift) R	*Hz*	-2,107E+06	-4,486E+06
E_J/E_C	E_J/E_C T		42	59
	E_J/E_C R		*37*	41
Junction	Crticial current T	A	1,2E-08	1,6E-08
	Critical current R	A	*1,1E-08*	1,3E-08

Table 5: Comparison between the expected values by design and the actual values of the two qubits under study (Q0 and Q2): qubit frequencies (bare), charging energy, Josephson energy E_J, read-out resonator frequencies (bare), χ shift, $\frac{E_J}{E_C}$ ratio and critical current. T stands for *theoretical* and R stands for *real*. Note that the values in italic blue are not derived from measurements, but are an educated guess.

For qubit 0 we expect by design $g_T = 170 \pm 20\,MHz$, which is related to the theoretical dispersive shifts through $\chi = -\frac{g^2}{\Delta}\frac{\alpha}{\Delta-\alpha}$. We obtain from our measurements $g_R = 220 \pm 3\,MHz$, according to this formula. For Cavity 4 we expect by design $g_T = 110 \pm 10\,MHz$, but we obtain $g_R = 254 \pm 6\,MHz$. For the theoretical estimations of g_T we assume a typical error of 10 % due to manufacturing tolerances. For the experimental estimation of g_R we use maximum errors. The theoretical and measured dispersive shift for the readout resonator of qubits 0 are $\chi_T = -1.19 \pm 0.02\,MHz$ and $\chi_R = -2.1 \pm 0.2\,MHz$, while those of qubit 2 are $\chi_T = -0.74 \pm 0.01\,MHz$ and $\chi_R = -4.49 \pm 0.04\,MHz$. We have used maximum error propagation for the theoretical results and maximum error for the experimental ones. Since the error of χ is statistical, we have taken three times the standard deviation to be able to compare it to the other maximum errors. The theoretical and measured detuning Δ for qubit 0 are $\Delta_T = -2.5 \pm 0.2\,GHz$ and $\Delta_R = -2.655 \pm 0.004\,GHz$, while for qubit 2 we have $\Delta_T = -2.0 \pm 0.2\,GHz$ and $\Delta_R = -2.144 \pm 0.004\,GHz$. In both cases the errors are maximum errors. The larger than expected dispersive shift for both qubits explains the higher than expected qubit-resonator couplings.

5.4 Time domain measurements

As mentioned in Sections 2.5 and 2.6, the time domain measurements give a vast amount of information about the performance of the single qubit. We here present: Rabi oscillations (Section 4.3.1), T_1 measurements (Section 4.3.2), Ramsey interferometry (Section 4.3.3) and Hanh echo (Section 4.3.4). These measurements allow us to find the optimal π-pulse, T_1, T_2^* and T_2. The π-pulse is important because it is the reference pulse for all single-qubit gates, so we need to optimal signal parameters in order to find a fast π-pulse. The relaxation and coherence times are crucial to evaluate the maximum potential of our qubits, since they give us the maximum fidelity we can achieve (Section 2.8).

5.4.1 Rabi oscillations

The Chevron plot in Figure 5.9a shows that the Rabi oscillation frequency for qubit 2 increases while the amplitude decreases when we change the frequency of the QD. This measurement allows us to find for which frequency the QD is resonant with the qubit and it is $5.517 \pm 0.001\,GHz$.

In order to perform gates, we want a π-pulse which is as fast as possible. In Figure 5.9b we set QD frequency to the Chevron plot centre in Figure 5.9a and we vary the attenuation on the QD. In agreement with Eq. 4.2, increasing the QD power leads to larger Rabi frequencies.

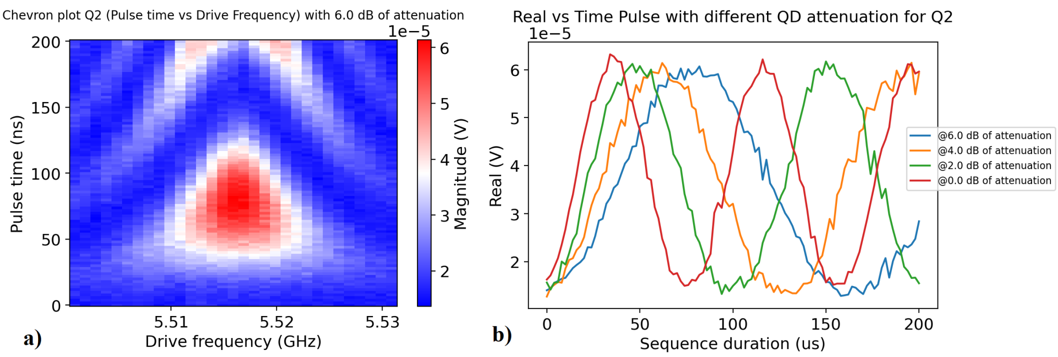

Figure 5.9: Measurement results of Rabi oscillations for qubit 2. **a)** Chevron plot for qubit 2: colorplot with x-axis the Qubit Drive frequency, y-axis the pulse time and color scale the magnitude of the readout resonator. **b)** Behaviour of Rabi oscillation when changing the attenuation on the Qubit Drive pulse.

In Figure 5.10, we fit Rabi oscillations for 0 dB Qubit Drive attenuation. The first trial function is a simple $\sin^2(x)$ (orange curve). The fit parameters provide a π-pulse duration

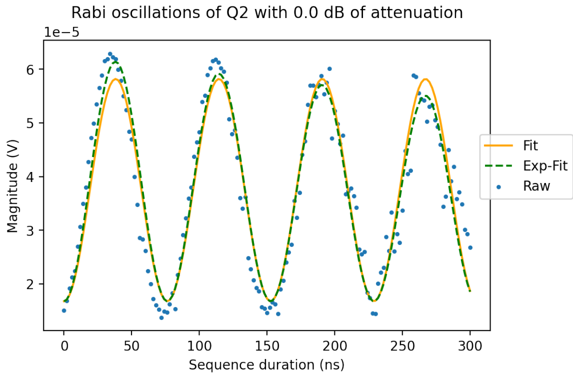

Figure 5.10: Comparison of Rabi oscillations fitting functions for qubit 2. The orange curve represents the fitting function $\sin^2(x)$, the dashed green curve the fitting function $\left(\sin^2(x) \times e^{-x}\right)$.

of 48.6 $\pm$ 0.1 ns, where the error is of the statistical type. In Figure 5.10 we see an example of some decoherence, in fact, trying to fit with a $\left(\sin^2(x) \times e^{-x}\right)$ type of function (dashed green line in Figure 5.10), we obtain better agreement with the data. This can happen if we do not put the qubit in its flux sweet spot [22]. From the analysis of Figure 5.8b, we have found out that the sweet spot of qubit 2 is -0.1759 V, but in the Rabi oscillations we used is -0.1500 V. This accounts for the small decoherence that we observe. Despite this, the duration of the π-pulse is the same.

We have done the same measurements for qubit 0 and the results are shown in Figure 5.11. We obtain the expected Chevron plot and compared to qubit 2 we can see more fringes. The reason is that we are sending more power to qubit 0 compared to qubit 2. In accordance with Eq. 4.2, we expected the Rabi oscillation frequency to increase when we increase power. With the same technique, we estimate the π-pulse for qubit 0 and we obtain 36.5 $\pm$ 0.4 ns, where the error is statistical.

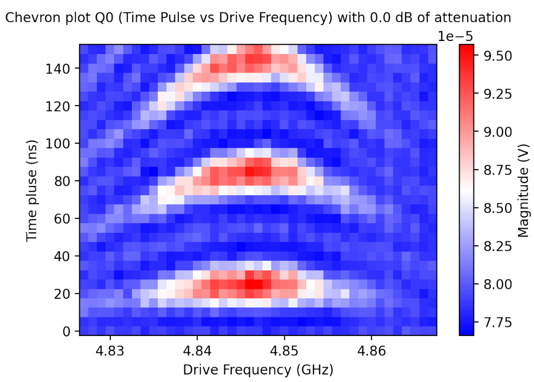

Figure 5.11: Chevron plot for qubit 0: colorplot with x-axis the Qubit Drive frequency, y-axis the pulse time and color scale the magnitude of the readout resonator.

5.4.2 T_1 measurements

We explored the protocol for T_1 measurements in Section 4.3.2 and now we will apply it to qubits 0 and 2. T_1 measures the relaxation from the excited state to the ground state.

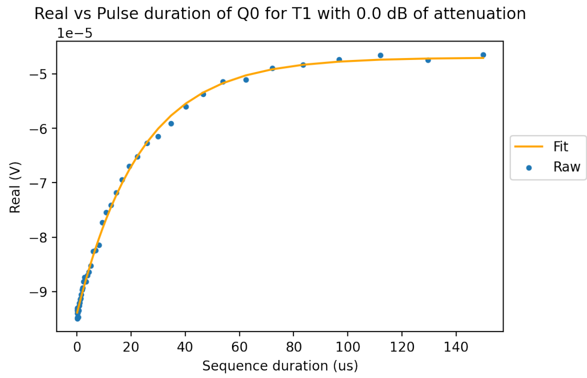

Figure 5.12: T_1 measurement for qubit 0: demodulated voltage output as a function the sequence duration has been fitted with e^{-x}. Experimental data in time are measured with a logarithmic step.

For qubit 0 we obtain the result in Figure 5.12. We fit the data in Figure 5.12 with an exponential fit and obtain the characteristic decay time $T_1 = 23.4 \pm 0.4\,\mu s$, where the error is statistical. This result is in accordance with T_1 times typically found in literature [63].

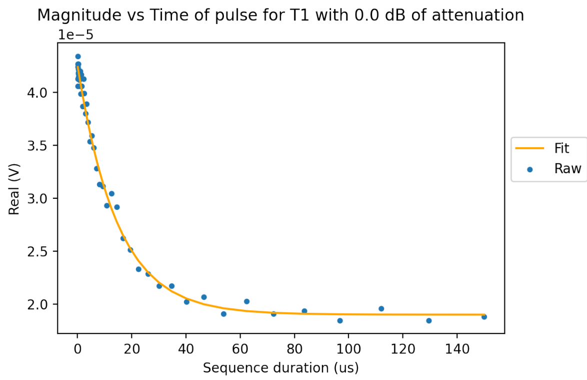

Figure 5.13: T_1 measurement for qubit 2: demodulated voltage output as a function the sequence duration has been fitted with e^{-x}. Experimental data in time are measured with a logarithmic step.

We can do the same measurement for qubit 2 and we obtain the behaviour in Figure 5.13. From the exponential fit we are able to extract $T_1 = 14.6 \pm 0.6\,\mu s$. We can see that both qubits have very good coherence times [63] and this is definitely positive for the execution of gates [32], as explained in Section 2.8.

5.4.3 Ramsey interferometry

Ramsey interferometry, discussed in Section 4.3.3, gives a very precise evaluation of the qubit frequency. It is also a way to give an estimate of T_2 when dephasing is relevant. In order to find the qubit frequency, we perform the Ramsey protocol and we sweep across different QD frequencies. This results in the Ramsey fringes in Figure 5.14a for qubit 2. In order to extrapolate the qubit frequency, we choose the frequency with the longer oscillation period, as shown in Figure 5.14a. In order to verify which of the surrounding frequencies is the closest to resonance, we can compare 5 curves around the center of the Ramsey fringes, as shown in Figure 5.14b. By doing this, we are able to determine that the frequency of qubit 2 is $\omega_{q2} = 5.51645 \pm 0.00003\,GHz$. The error in the qubit frequency is of the maximum type. This result is much more precise compared to the qubit spectroscopy shown in Figure 5.7.

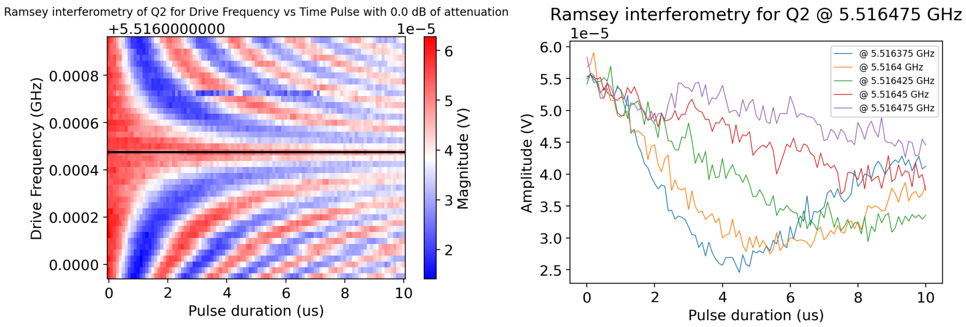

Figure 5.14: Extrapolation of the frequency of qubit 2. **a)** Ramsey fringes for qubit 2: colorplot with x-axis the pulse duration, y-axis the Qubit Drive frequency and color scale the magnitude of the readout resonator. The centre of Ramsey fringes has been highlighted with the black straight lines. In **b)** line-cuts of the colorplot in **a)** for fixed Qubit Drive frequencies around the black line.

Another important result is the T_2^* measurement. It is typically done off-resonance, so that it includes a higher degree of dephasing, as shown in Eq. 2.39. The performed fit uses the function $\left(\sin(x) \times e^{-x^2}\right)$. We can extrapolate the decay time of the exponential and obtain T_2^*.

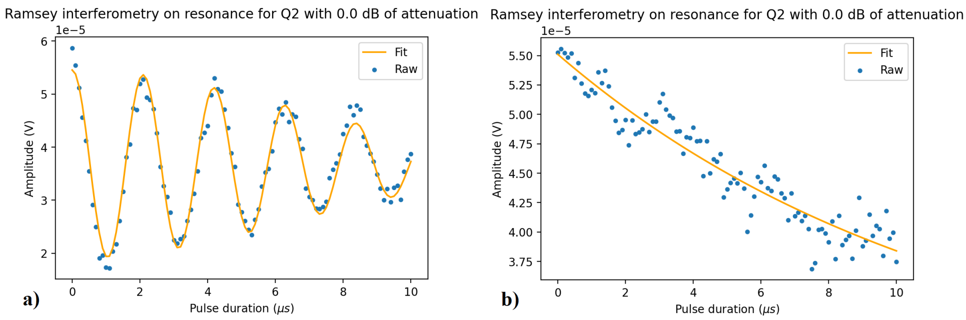

Figure 5.15: On- and off-resonance Ramsey oscillation fit. In **a)** fit of the off-resonance Ramsey oscillation at $\delta\omega = 2.99 \pm 0.01\ MHz$ detuning using $\left(\sin(x) \times e^{-x^2}\right)$. In **b)**, fit of the on-resonance Ramsey measurement with (e^{-x}).

The same procedure can also be done on-resonance, where we simply use an exponential decay of the type (e^{-x}) to fit data points (Figure 5.15). The off-resonance measurement in Figure 5.15a gives us $T_{2,off}^* = 9.2 \pm 0.4\,\mu s$, where the error is statistical. We can also extrapolate the detuning from fitting the oscillation frequency and we obtain $\delta\omega = 2.995 \pm 0.009\ MHz$, where the error is of the statistical type. The decay time in the on-resonance case in Figure 5.15b is $T_{2,on}^* = 12 \pm 3\,\mu s$. It is clear that on-resonance the dephasing has decreased and we obtain longer T_2 times.

We have done the same measurements for qubit 0 (Figure 5.16a). In Figure 5.16b we plot five Ramsey measurements at fixed QD frequency and we look out for the one that oscillates the least. From this procedure we are able to extract the frequency of qubit 0, which is $\omega_{q0} = 4.84762 \pm 0.00002\ GHz$, where the error is maximum. Fit of the on- and off-resonance Ramsey measurements gives a decay time and detuning: $T_{2,off}^* = 3.8 \pm 0.5\,\mu s$ and $\delta\omega = 2.37 \pm 0.04\ MHz$. The on-resonance decay time is $T_{2,on}^* = 4.7 \pm 0.4\,\mu s$. The errors of $T_{2,off}^*$, $T_{2,on}^*$ and $\delta\omega$ are all statistical. We observe an increase of T_2^* when going from off-resonance to on-resonance, as expected.

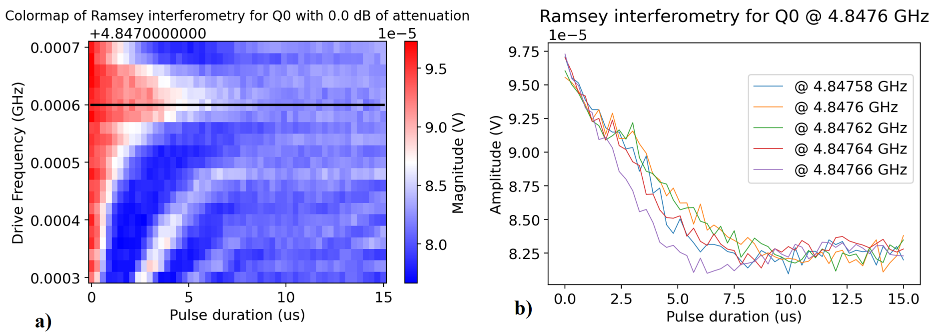

Figure 5.16: Extrapolation of the frequency of qubit 0. **a)** The centre of Ramsey fringes has been highlighted with the black straight lines. In **b)** line-cuts of the colorplot in **a)** for fixed Qubit Drive frequencies around the black line.

5.4.4 Hahn Echo measurement

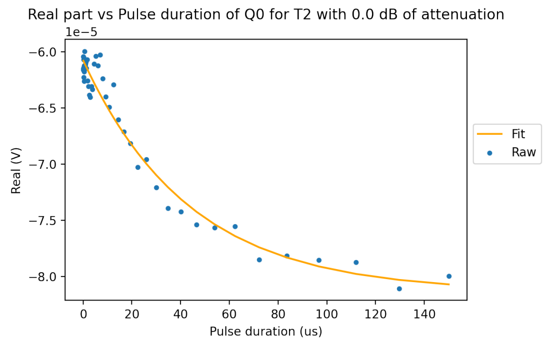

Figure 5.17: Hahn Echo measurement for qubit 0. We plot the real part of the demodulated output voltage signal. The orange line is the fit given by (e^{-x}) to give the Hahn-echo time T_2. Experimental data in time are measured with a logarithmic step.

The Hahn Echo measurement is a way to measure T_2 in which the effect of dephasing is suppressed. As shown in Section 4.3.4, this is achieved through a refocusing pulse, which counteracts dephasing on the equatorial plane by putting the qubit state on the other side of the equator of the Bloch sphere. As a consequence, we expect a $T_2 \approx 2T_1$. Using the protocol in Section 4.3.4, we obtain Figure 5.17 for qubit 0 and Figure 5.18 for qubit 2. For qubit 0, we obtain $T_2 = 44 \pm 5\,\mu s$, while for qubit 2 we obtain $T_2 = 27 \pm 2\,\mu s$, where both the errors are statistical.

As in the case of T_1, the T_2 times are comparable to those found in literature [63]. The two qubits are also comparable to each other. In Hahn echo protocol we expect to have noticeably diminished the effect of dephasing and we expect to be in the $T_2 \approx 2T_1$ limit. For qubit 0 we obtain $T_2 = 44 \pm 5\,\mu s$ and $2T_1 = 46.8 \pm 0.8\,\mu s$, therefore the two estimates are compatible within the errors. For qubit 2 we obtain $T_2 = 27 \pm 2\,\mu s$ and $2T_1 = 29 \pm 1\,\mu s$, as expected.

5.5 Conclusion of single-qubit characterization

After the spectroscopy and time-domain measurements, we have found out the key characteristics of the two qubits under study. They are summarized in Table 6. By using Eq. 2.52 in Section 2.8, we are able to give an estimate of the maximum fidelity expected for the qubits we characterized. We obtain the dephasing decay as $\Gamma_\varphi = \Gamma_2 - \frac{\Gamma_1}{2}$ from Eq.

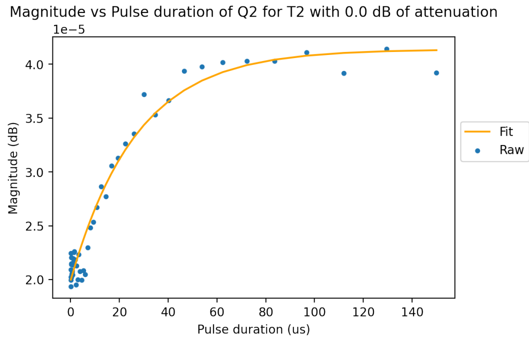

Figure 5.18: Hahn Echo measurement for qubit 2. We plot the real part of the demodulated output voltage signal. The orange line is the fit given by (e^{-x}) to give the Hahn-echo time T_2. Experimental data in time are measured with a logarithmic step.

	Qubit 0	**Qubit 2**
Qubit Frequency	$4.84763 \pm 0.00002\ GHz$	$5.51650 \pm 0.00003\ GHz$
π-pulse	$36.5 \pm 0.4\ ns$	$48.6 \pm 0.1\ ns$
T_1	$23.4 \pm 0.4\ \mu s$	$14.6 \pm 0.6\ \mu s$
$T_{2R,off}$	$3.8 \pm 0.5\ \mu s$	$9.2 \pm 0.4\ \mu s$
$T_{2R,on}$	$4.7 \pm 0.4\ \mu s$	$12 \pm 3\ \mu s$
T_2	$44 \pm 5\ \mu s$	$27 \pm 2\ \mu s$
F_{max}	99.85 ± 0.01 %	99.76 ± 0.03 %

Table 6: A brief summary of all the important qubit characteristics at their flux sweet spot, which will be useful for gate operation and their benchmarking: qubit transition frequency, duration of the π-pulse, relaxation time T_1, on- and off-resonance Ramsey T_2 times, Hanh echo T_2 times and maximum fidelity for $\tau = 100$ ns mean gate duration. The errors of the qubit frequency and maximum fidelity are of the maximum type, while the remaining are statistical.

2.39. For qubit 0 we have $\Gamma_\varphi = 0.001 \pm 0.003\,\mu s^{-1}$ and $\Gamma_\varphi = 0.003 \pm 0.004\,\mu s^{-1}$ for qubit 2, which means that dephasing (Γ_φ) consistent with zero and is less of a factor compared to relaxation and decoherence (Γ_1 and Γ_2). The errors for the dephasing rates are of the maximum type. By substituting these results into Eq. 2.52 with a gate duration $\tau = 100$ ns we obtain a maximum fidelity $F^0_{max} = 99.85 \pm 0.01$ % for qubit 0 and $F^2_{max} = 99.76 \pm 0.03$ % for qubit 2, as shown in Table 5. The errors for the fidelities are maximum errors. The goal in the following Sections is to optimize the pulses we use for Randomized Benchamarking and try to get as close as possible to the maximum theoretical value.

5.6 Calibration of π- and $\frac{\pi}{2}$-pulses

In Section 4.4.1 we have discussed how to calibrate the π- and $\frac{\pi}{2}$-pulses and the great impact that this kind of calibration has on the fidelity of the qubits. In this Section we are going to search for the parameters that optimize the π- and $\frac{\pi}{2}$-pulses for our qubits. We begin with the calibration of the π-pulse of qubit 0. We have to correct for possible differences in amplitude between the I and Q parts of the signal, generated by the AWG, the LO cards and the I-Q mixer. Ideally, the I and Q parts of the signal have equal amplitudes, but a mismatch is not excluded. We use the protocol described in Section 4.4.1 to study and correct this behaviour. We here send a train of 8, 16, 64 and 256 π-pulses to obtain Figure 5.19a.

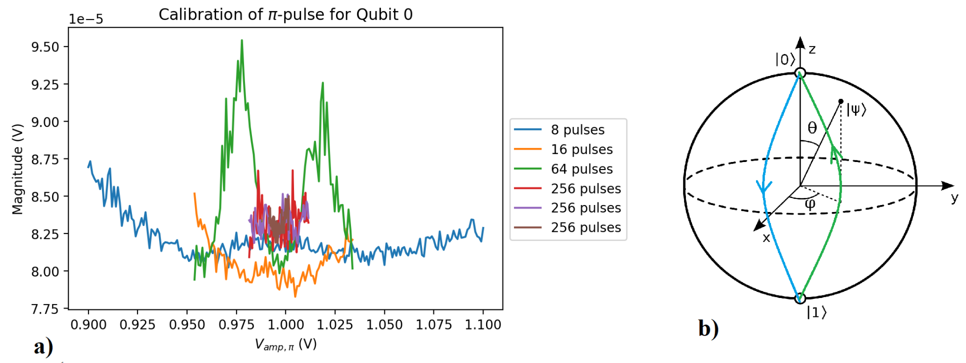

Figure 5.19: π-pulse calibration for qubit 0. **a)** We apply a train of n π-pulses (n is provided in the legend), and we measure the demodulated voltage magnitude as a function of the parameter $V_{amp,\pi}$. When we increase the number of π-pulses the effect of the mismatch between I and Q is more noticeable. **b)** Representation on the Bloch sphere of the applied π-pulses train.

The larger is the number of π-pulses, the larger the probability to observe the effect of the I and Q mismatch. If there is no error, we expect the qubit to be found in the ground state, which is the initial state, for $V_{amp,\pi} = 1$. However, since there are unbalances, we expect to see variations when sweeping across different $V_{amp,\pi}$. Specifically speaking, we observe an oscillatory behavior of the demodulated output voltage as a function of $V_{amp,\pi}$. Such behavior depends on the number of π-pulses applied: the larger it is, the faster these oscillations are. Therefore, we here perform a recursive tune-up: the starting point is the sequence with a small number of π-pulses. See, for example the blue and orange lines in Figure 5.19a (namely, for 8 and 16 pulses, respectively). Then, we send longer trains of pulses, in order to narrow down the range of $V_{amp,\pi}$ that matches the I and Q parts of the signal. When we find the optimal parameter, looking at the Bloch sphere in Figure 5.19b, we ensure that by performing a long train of π-pulses we actually return to the ground state as wanted. We perform this sequence of pulses and we find that the optimal $V_{amp,\pi}$ is $0.9962 \pm 0.0004\ V$, where the error is maximum.

A similar procedure applies for the $\frac{\pi}{2}$-pulse, with a correction parameter $V_{amp,\frac{\pi}{2}}$. The sweet spot for $V_{amp,\frac{\pi}{2}}$ is $0.9322 \pm 0.0001\ V$, where the error is of the maximum type.

We repeat the same procedure for qubit 2 and we obtain an optimal $V_{amp,\pi}$ of $0.923 \pm 0.001\ V$, while for $V_{amp,\frac{\pi}{2}}$ we found $0.839 \pm 0.004\ V$, where these errors are of the maximum type.

5.7 DRAG scheme optimization

In Section 4.4.2 we have discussed the DRAG pulse optimization technique and we have used it to further optimize the signal we are sending to the qubit. We are going to limit ourselves to calibrate the α parameter in Eq. 4.3 and we leave Δ fixed. From the *AllXY* pulses in 4.4.2 we are going to use the four combinations in the legend of Figure 5.20.

When we vary α, we are moving the state of the qubit on the Bloch sphere. As explained in more detail in Section 4.4.2, the optimal parameter we find through the intersection of

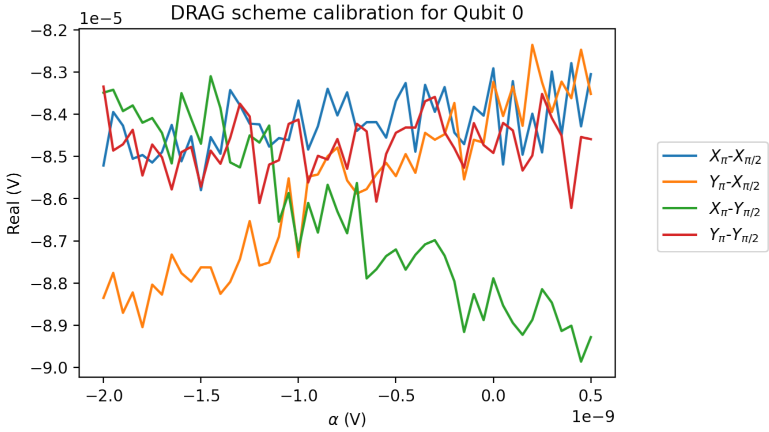

Figure 5.20: DRAG scheme optimization for qubit 0 with the AllXY technique: real part of the demodulated voltage as a function of the DRAG scaling α for the sequences reported in the legend. In accordance with [64], the $X_\pi - X_{\frac{\pi}{2}}$ and $Y_\pi - Y_{\frac{\pi}{2}}$ pulses do not vary with α, while the other two do. The optimal α is where the two curves (green and orange curves) cross each other.

the two linear fit is $\alpha = -1.0\,nV$. We can see that the blue and red curves, which we expect to have negligible error as described in Section 4.4.2, are in agreement with the AllXY protocol in [64].

With the same procedure, we do the DRAG scheme for qubit 2 and we obtain the optimal $\alpha = -0.42 \pm 0.04\,nV$, where this error is maximum. This procedure is very important for the optimization of the qubit performance. In Section 4.4.2 we showed that it is capable of reducing phase and leakage errors, hence improving the fidelity of single-qubit gates.

5.8 Randomized Benchmarking

Up to now we have characterized the two qubits and we have optimized the pulses which we send to perform the single-qubit gates in Section 2.8. Now we are going to perform the single-qubit Randomized Benchmarking (RB) protocol discussed in Sections 2.8 and 4.5.

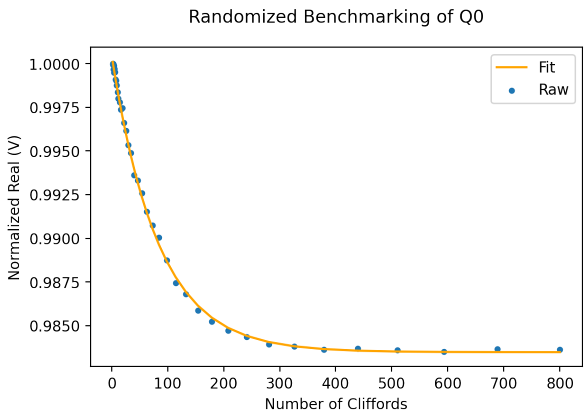

Figure 5.21: Randomized Benchmarking of qubit 0. The x-axis represents the number of Clifford gates used in each sequence and the y-axis is the normalized demodulated voltage of the readout resonator. The orange curve is the fit of the data points and it provides the fidelity.

In Figure 5.21, we report the real part of the demodulated readout voltage averaged over

31 pseudo-random seeds, as a function of the number of Clifford gates in the RB sequence. We used Eq. 4.7 as fitting function, in order to estimate the parameter p, which represents the depolarization errors mentioned in Section 4.5. We find out that $p = 98.803 \pm 0.001$ %, where this error is statistical. The decay fit parameter is related to the r-parameter through Eq. 4.8. By using Eq. 4.9, we obtain the average single-qubit Clifford fidelity $F = 99.40 \pm 0.08$ % for qubit 0 and the error is statistical.

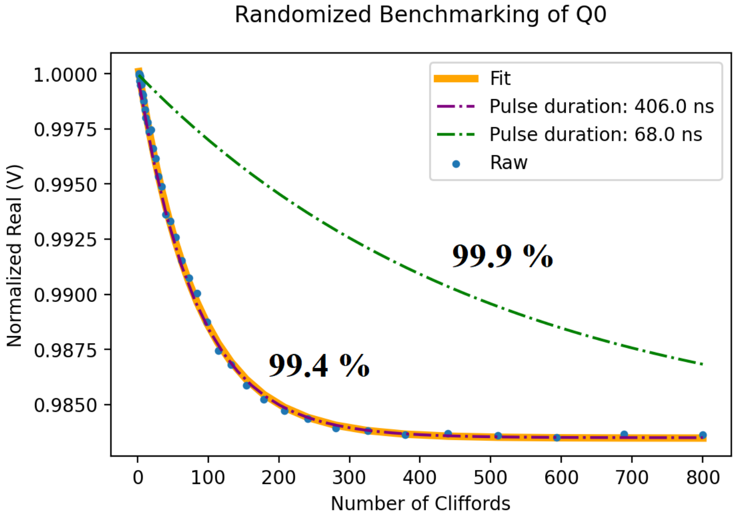

Figure 5.22: Randomized Benchmarking outcomes for qubit 0. The orange line is the experimental fit of the data, obtained from $A + Bp^N$, while the dashed green and magenta curves are the theoretical RB curves obtained for 99.9 % and 99.4 % target fidelities, respectively, obtained by using $1 - \frac{\tau}{3} \cdot (\Gamma_1 + \Gamma_\varphi)$ and mean duration gate pulses in the legend. 99.4 % target fidelity is in agreement with the experimental data, which suggests a mean duration time of the gate pulse sequence of 406.0 ns.

This fidelity is consistent with state of the art qubits [6], [30], but the goal is reaching 99.9 % fidelity for the single-qubit. The higher the single-qubit fidelity is, the better the two-qubit gates will be. As a matter of fact, when we increase the number of qubits for multi-gate operation, these small errors accumulate. This is why there is a big push in making high performance single qubits.

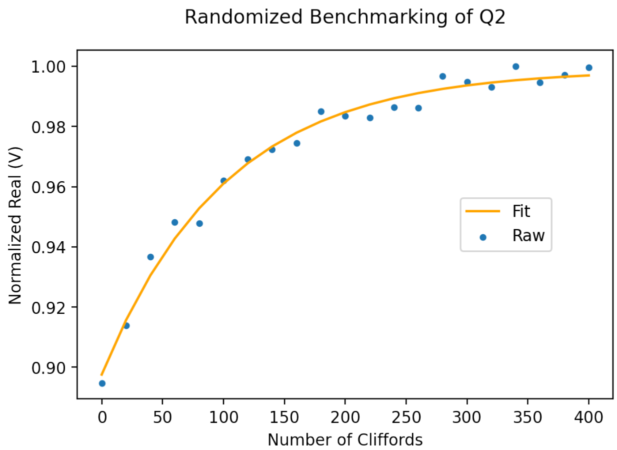

Figure 5.23: Randomized Benchmarking of qubit 2. The x-axis represents the number of Cliffords used in each sequence and the y-axis is the normalized demodulated voltage of the readout resonator. The orange curve is the fit of the data points and it provides the fidelity.

From Eq. 2.52 we are able to find the maximum fidelity and compare it the one found from the fit. In order to obtain the same fidelity of $F = 99.40 \pm 0.08$ %, we need to have a mean gate duration $\tau = 406$ ns, as shown in Figure 5.22. In order to get a fidelity of 99.9 %, the mean duration gate should be 68 ns.

In a similar fashion, we have done the RB measurements for qubit 2 (Figure 5.23). The fit returns $F = 99.51 \pm 0.04$ % with statistical errors. We can compare it with the theoretical expectations given in Eq. 2.52 for two different pulses with duration $\tau = [42, 206]\ ns$. The curve with mean gate duration of 206 ns represents the actual fidelity of $F = 99.51 \pm 0.04$ % and is in agreement with the exponential fit, as shown in Figure 5.24.

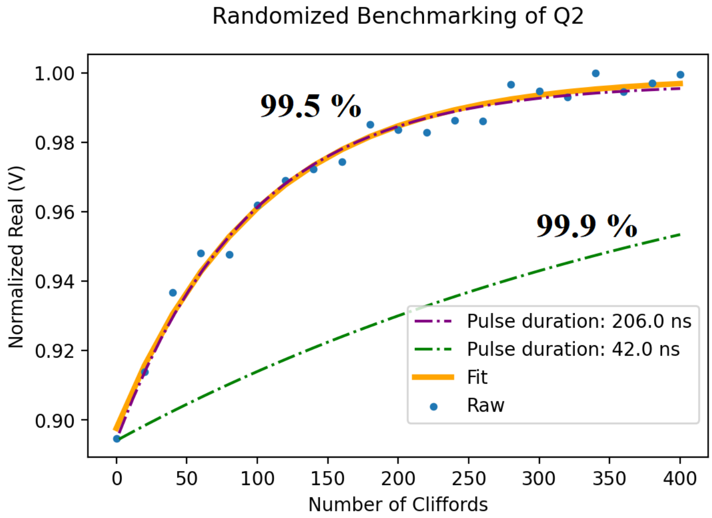

Figure 5.24: Randomized Benchmarking outcomes for qubit 2. The orange line is the experimental fit of the data, obtained from $A + Bp^N$, while the dashed green and magenta curves are the theoretical RB curves obtained for 99.9 % and 99.5 % target fidelities, respectively, obtained by using $1 - \frac{\tau}{3} \cdot (\Gamma_1 + \Gamma_\varphi)$ and mean duration gate pulses in the legend. 99.5 % target fidelity is in agreement with the experimental data, which suggests a mean duration time of the gate pulse sequence of 206.0 ns.

The curve with mean gate duration of 42 ns represents a fidelity of 99.9 ± 0.02 % for qubit 2 and is the goal of our optimization. From the curves with 99.9 % gate fidelity it is clear that we have greatly optimized the signals to evaluate the performance of the qubits, but there is still optimization to be done in order to achieve higher fidelities. The calibration procedure here proposed has been done iteratively for two times. However, in order to optimize the process an automatic tune-up is necessary [6], [11], [30], [63], [66]. This is outside the main goal of this thesis, but we stress that the fidelity can be further improved.

By comparing the results in Figures 5.22 and 5.24, the mean gate time of qubit 0 ($\tau = 406$ ns) is almost double that of qubit 2 ($\tau = 206$ ns). This can be attributed to how fast we can make the π-pulse. In the case of qubit 0, the duration of the π-pulse in this measurement is 29.3 ns, while for qubit 2 the duration of the π-pulse is 10 ns. It is obvious that, if the π-pulse is faster, the qubit is subject to less decoherence while performing a fixed length sequence, which leads to better fidelities, hence shorter mean gate duration.

5.9 Avoided Level Crossing

In order to perform two-qubit gates, like the iSWAP discussed in Section 2.10, we need to couple the two qubits by putting them into resonance. Since qubit 2 has a higher flux sweet spot frequency (Section 5.2), we flux tune its frequency around that of qubit 0 (Section 4.6).

We perform a spectroscopy on qubit 2 while sweeping the flux on qubit 2 and we observe the avoided level crossing in Figure 5.25. With a drive attenuation on qubit 2 of 9 dB, qubit 0 is kept in its ground state at the flux sweet-spot. The avoided level crossing occurs around the eigenvalue of $|11\rangle$, obtained from Eq. 2.54. The reason is that, in order to perform the spectroscopy of qubit 2 in Figure 5.25, we must make the $|0\rangle \rightarrow |1\rangle$ transition occur by sending an appropriate QD pulse. Therefore, it is our measurement that makes the reference energy the eigenvalue of the $|11\rangle$ state of the two coupled qubits. Furthermore, the faint line between the two branches of the avoided level crossing is only visible when enough power is sent to excite also the $|00\rangle \rightarrow |11\rangle$ transition. Since we are interested in performing a two-qubit gate (the iSWAP), this is definitely an aspect that might interfere with the swap of energy between the $|01\rangle$ and $|10\rangle$ states, as described in Sections 2.10 and 4.6. From this experiment we can:

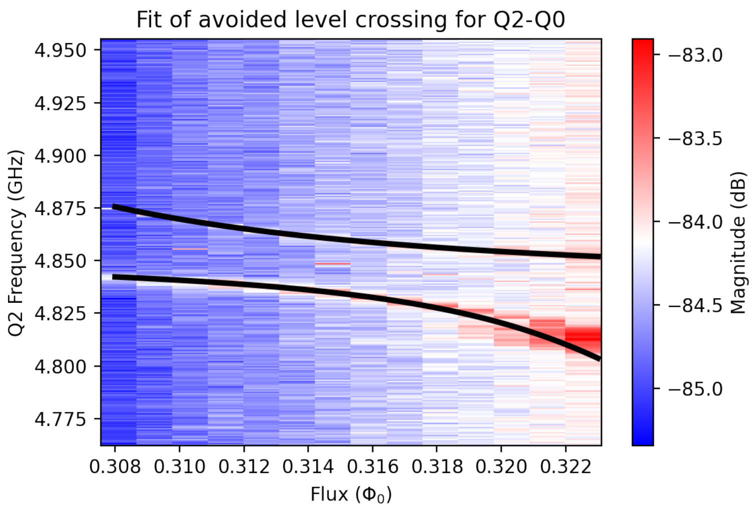

Figure 5.25: Avoided level crossing for qubits 0 and 2: on the x-axis the applied flux on qubit 2 in flux quanta, on the y-axis the qubit frequency of qubit 2 and the color scale is the demodulated magnitude in dB of the readout resonator. The black curves represent the $|01\rangle$ and $|10\rangle$ states of the two-qubit system. They are obtained by fitting the avoided level crossing in accordance with Eq. 2.56.

- estimate the coupling energy J between qubit 0 and qubit 2;
- find the range of the flux on qubit that will allow to put on resonance qubit 0 and qubit 2, and therefore implement two-qubit gates, like the iSWAP described in Section 2.10;

For the latter, we can see that the avoided level crossing occurs around $0.315 \pm 0.001\ \Phi_0$, where this error is of the maximum type. For the former, we can extract the two curves from Figure 5.25 and fit them. In order to fit the two curves, we use Eq. 2.56 as a fit model and we are able to find the coupling $\boldsymbol{J}$. For the lower branch of the avoided level crossing we find that $J_l = 8 \pm 3\ MHz$, while for the upper branch we find that $J_u = 13 \pm 2\ MHz$, where both the errors are statistical. The two coupling strengths are compatible with each other, as expected. Also, the values of the coupling strength are of the same order of magnitude to those found in literature [34].

5.10 Towards two-qubit gates optimization: preliminary results of iSWAP gates

The next step is to focus on two-qubit gate operations. In this work, we had the chance to present preliminary data of an iSWAP gate by using qubits 0 and 2. The starting point for this measurement are the results in Section 5.9, where we find the optimal flux range for the two qubits to resonate. In the iSWAP we implement an energy exchange between the $|01\rangle$ and $|10\rangle$ states of the two qubits, by biasing qubit 2 by means of the external flux knob, in order to put it on resonance with qubit 0 at its flux-sweet spot.

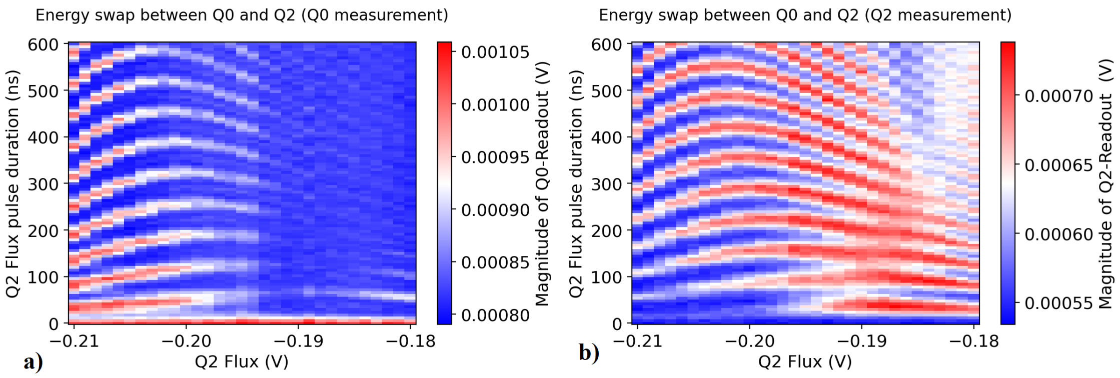

Figure 5.26: iSWAP exchange of energy between qubit 0 and qubit 2: on the x-axis the magnitude flux applied on qubit 2 in V, on the y-axis the duration of the flux pulse and the color scale is demodulated magnitude of the readout resonators of qubit 0 and qubit 2, **a)** and **b)** respectively. We perform a simultaneous measurement of both qubits, as described in Section 4.6. In **a)** we show the oscillations between $|01\rangle$ and $|10\rangle$ when reading qubit 0, while in **b)** we do the same by reading qubit 2.

We here send a flux-voltage pulse with different amplitude and duration, and we obtain a Chevron-like pattern, which corresponds to the exchange of energy between the states $|01\rangle \leftrightarrow |10\rangle$ for both qubits. The proof that the two qubits are actually exchanging energy is that Figures 5.26a and 5.26b are mirrored with regards to the magnitude of the readout signal. We extrapolate the oscillations at a fixed flux voltage pulse amplitude, as shown in Figure 5.27a. We use the approach of Rabi oscillations to find the characteristic oscillation time of the two-level system between $|01\rangle$ and $|10\rangle$. Hence, we fit with a $\sin^2 x$ and it results in Figure 5.27b. The oscillations between the states $|01\rangle$ and $|10\rangle$ happen in 21.5 ± 0.1 ns, where this error is statistical.

The measured oscillations should be symmetric, as shown in Figure 2.23. We can clearly see from Figures 5.26 and 5.27 that the oscillations are strongly distorted. This can be due to many factors. A very common problem is the shape of the signal that we use for the flux biasing. We typically use square wave-like signal pulse, which has a finite rise. As occurs for drive pulses, our electronics generate signals similarly to Figure 4.14, which can cause deviations in the measured response.
This behaviour becomes particularly important when the signal duration is short. When the signal is long, in fact, over- and under-shooting becomes less relevant. A possible way to solve this problem is proposed in [71], where they use a hardware solution named

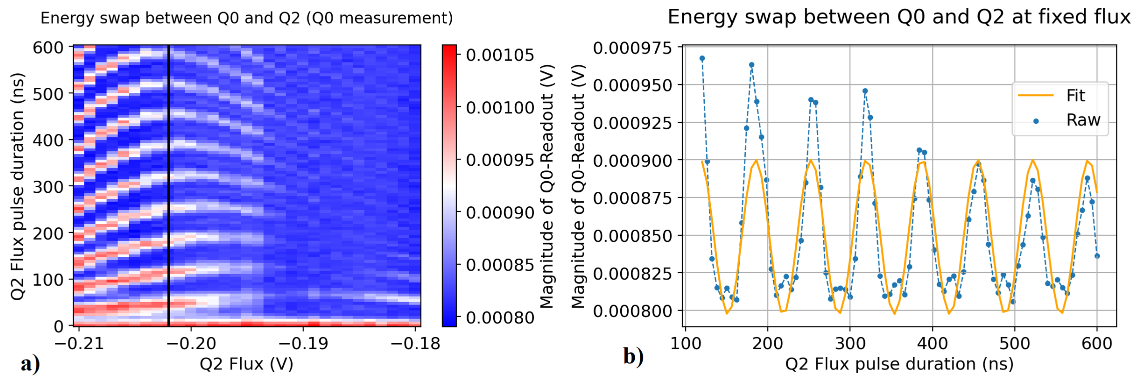

Figure 5.27: In **a)** iSWAP exchange energy diagram between Q0 and Q2. The black line identifies the line-cut corresponding to -0.202 V. In **b)** line-cut plot, which is fitted with a Rabi-like function in order to get an estimation of the iSWAP gate duration time.

Cryoscope. It employs a series of filters which correct this kind of behaviour of the signal.

Other possible imperfections in the system and the setup are: leakage to non-computational states, gate bleedthrough and cross-talk between next-nearest-neighbors (NNN). In [6] they have developed an algorithm, called **ORBIT**, which deals with all the mentioned problems above. Since transmons are not a perfect two-level system, there are non-computational levels, like $|02\rangle$ or $|20\rangle$. When these are close enough to the computational levels $|01\rangle$ and $|10\rangle$ used in the iSWAP, it is possible that the pulses might cause transitions to the non-computational levels. This can occur because of the overshoot during the rise. It is also possible that higher harmonics of the signal might not be attenuated enough, so they could resonate with the non-computational levels. Gate bleedthrough, instead, refers to the possibility that the mechanism for implementing a gate might not turn off adequately at the end of the sequence [6]. Finally, NNN manifests itself in the form of cross-talk, which usually happens when the frequencies of the qubits are similar and resonate, as described in [6], or if a finite cross-talk occurs in the drive lines on chip. A possible solution to NNN coupling and parasitic couplings, which could be responsible for the asymmetry in Figure 5.26, is to change the design of the chip and use a tunable coupler, i.e. the coupling between two qubits is provided by an additional qubit [33]. It allows to turn on and off the coupling between the qubits, which enables better single-qubit gates and decreases the cross-talk between NNN qubits. Tunable couplers also help with reducing parasitic effects when the duration of the gate is longer [33], so that the limiting factor in gate fidelities is the decoherence of the qubits.

6 Conclusions

In this thesis we have characterised two coupled qubits. These measurements provide us with a starting point for the optimization process of the pulses used for single qubit gates. By adjusting specific parameters of the instruments and applying specific pulse calibration procedures, the imperfections in the generated pulses are compensated. This procedure is important because it allows to improve the fidelity of single-qubit operations. In order to give an estimate of this fidelity we use Randomized Benchmarking (RB). This procedure is representative of real-life algorithms and we obtain the following gate fidelities: $F_{Q_0} = 99.40 \pm 0.01$ % and $F_{Q_2} = 99.54 \pm 0.04$ %. The optimization process has enabled us to have high fidelity single-qubit gates. It is reasonable to assume that, by improving the optimization parameters, it is possible to further improve the RB fidelities, in accordance with the theoretical predictions.

The implementation of optimization protocols is crucial for two-qubit gates, because their realization can be hampered if the single-qubit fidelities are low. The golden standard is 99.9 %, but despite this our fidelities are high enough to observe two-qubit gates. Indeed, we have reported preliminary iSWAP gates measurements, which confirm the possibility to implement two-qubit gates on the analyzed device. However, we have noticed a strong asymmetry in the iSWAP oscillations, which may be related to both unoptimized control and drive pulses, unwanted coupling with nearest qubits on chip and leakage to non-computational states.

All these problems are common [6], [33], [71], [72],[73], and further investigation is required in order to optimize the outcomes of the iSWAP measurements for future implementation of high-fidelity two- and multi-qubit gates operations. Future perspectives include the possibility to provide two-qubit iSWAP gate fidelity, study other types of two-qubit gates and eventually exploit the circuit design in order to implement multi-qubit algorithms involving all the 5 qubits on the chip, such as quantum error detection/correction schemes [6], [28], [38]. The results reported in this work are of great value to reach the goal, because they suggest that a correct and deep tune-up of measurement and characterization protocols for multi-qubit system, and its understanding, is fundamental for the scaling of superconducting quantum processors.

Appendix

A Example of up-conversion in an I-Q Mixer

The I-Q mixer requires three input signals: LO signal, I and Q signals. The LO signal is:

$$s_{LO}(t) = A_{LO}\cos(\omega_{LO}t), \tag{A.1}$$

with ω_{LO} the local oscillator frequency and A_{LO} the amplitude of the LO. The I and Q signals are IF signals of the type:

$$s_I(t) = A_I\cos(\omega_{IF}t) \tag{A.2}$$

$$s_Q(t) = A_Q\sin(\omega_{IF}t). \tag{A.3}$$

The LO signals is equally split between the two branches (Figure A.1) and becomes:

$$\frac{s_{LO}(t)}{2} = \frac{A_{LO}}{2}\cos(\omega_{LO}t). \tag{A.4}$$

In one of the two branches occurs a $\frac{\pi}{2}$ shift and the LO signal becomes $-\frac{A_{LO}}{2}\sin(\omega_{LO}t)$. These signals are combined with the I and Q signals and the resulting signal is of the following frequencies:

$$\omega_{RF} = \omega_{LO} \pm \omega_{IF}. \tag{A.5}$$

The output signal is an RF signal of similar frequency of the LO, since the IF signal is usually an order of magnitude lesser than the LO signal. The RF signal has the following expression:

$$s_{RF}(t) = A_{RF}\cos(\omega_{RF}t + \theta_{RF}), \tag{A.6}$$

with ω_{RF} from Eq. 3.3 and θ_{RF} an additional phase given by the mixers when combining the signals.

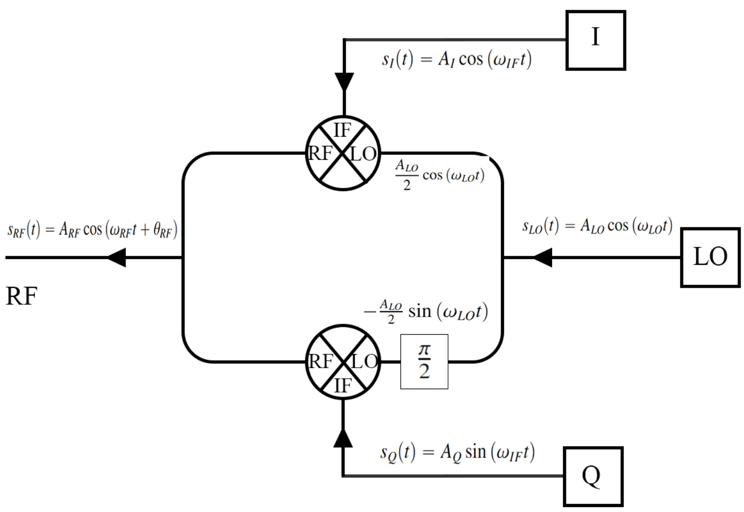

Figure A.1: Diagram of the processes happening for the correct operation of an I-Q Mixer

B Derivation of the theoretical expression of avoided level crossing

The Hamiltonian of the two qubits coupled through the resonator for $\hbar = 1$ reads as [34]:

$$H_J = \frac{\omega_{q1}}{2}\sigma_1^z + \frac{\omega_{q2}}{2}\sigma_2^z + (\omega_r + \chi_1\sigma_1^z + \chi_2\sigma_2^z)a^\dagger a + J(\sigma_1^-\sigma_2^+ + \sigma_1^+\sigma_2^-). \tag{B.1}$$

Here we consider only one mode of the cavity, for example $j = 1$, and we work in the low photon regime, such that $a_j^\dagger a_j = 1$. Now we write Eq. B.1 in the matrix form, remembering that, for example, $\sigma_1^z \equiv \sigma_1^z \otimes \hat{\mathbf{1}}_\mathbf{2}$. These are all matrices in a 4D Hilbert space and we write them as:

$$\sigma_1^z = \begin{pmatrix} 1 & 0 & 0 & 0 \\ 0 & 1 & 0 & 0 \\ 0 & 0 & -1 & 0 \\ 0 & 0 & 0 & -1 \end{pmatrix} \qquad \sigma_2^z = \begin{pmatrix} 1 & 0 & 0 & 0 \\ 0 & -1 & 0 & 0 \\ 0 & 0 & 1 & 0 \\ 0 & 0 & 0 & -1 \end{pmatrix} \tag{B.2}$$

$$\sigma_1^+ = \begin{pmatrix} 0 & 0 & 1 & 0 \\ 0 & 0 & 0 & 1 \\ 0 & 0 & 0 & 0 \\ 0 & 0 & 0 & 0 \end{pmatrix} \qquad \sigma_1^- = \begin{pmatrix} 0 & 0 & 0 & 0 \\ 0 & 0 & 0 & 0 \\ 1 & 0 & 0 & 0 \\ 0 & 1 & 0 & 0 \end{pmatrix} \tag{B.3}$$

$$\sigma_2^+ = \begin{pmatrix} 0 & 1 & 0 & 0 \\ 0 & 0 & 0 & 0 \\ 0 & 0 & 0 & 1 \\ 0 & 0 & 0 & 0 \end{pmatrix} \qquad \sigma_2^- = \begin{pmatrix} 0 & 0 & 0 & 0 \\ 1 & 0 & 0 & 0 \\ 0 & 0 & 0 & 0 \\ 0 & 0 & 1 & 0 \end{pmatrix} \tag{B.4}$$

$$\sigma_2^-\sigma_1^+ = \begin{pmatrix} 0 & 0 & 0 & 0 \\ 0 & 0 & 1 & 0 \\ 0 & 0 & 0 & 0 \\ 0 & 0 & 0 & 0 \end{pmatrix} \qquad \sigma_2^+\sigma_1^- = \begin{pmatrix} 0 & 0 & 0 & 0 \\ 0 & 0 & 0 & 0 \\ 0 & 1 & 0 & 0 \\ 0 & 0 & 0 & 0 \end{pmatrix}. \tag{B.5}$$

Using this representation, we can rewrite the Hamiltonian of the two coupled qubits (ignoring the coupling resonator) in Eq. B.1 in the matrix form as follows:

$$H_J = \begin{pmatrix} \frac{\omega_{q1}}{2} + \frac{\omega_{q2}}{2} & 0 & 0 & 0 \\ 0 & \frac{\omega_{q1}}{2} - \frac{\omega_{q2}}{2} & J & 0 \\ 0 & J & \frac{-\omega_{q1}}{2} + \frac{\omega_{q2}}{2} & 0 \\ 0 & 0 & 0 & \frac{-\omega_{q1}}{2} - \frac{\omega_{q2}}{2} \end{pmatrix}. \tag{B.6}$$

Now we diagonalize Eq.B.6 and we obtain four eigenvalues:

$$f_{1,2} = \pm(\frac{\omega_{q1} + \omega_{q2}}{2}) \tag{B.7}$$

$$f_{3,4} = \pm\frac{\sqrt{(\omega_{q2} - \omega_{q1})^2 + 4J^2}}{2} \tag{B.8}$$

It is clear that the avoided level crossing is described by the eigenvalues $f_{3,4}$. Let us suppose that in Eq. B.8 the variable is the frequency of qubit, so ω_{q1} is kept constant and

$\omega_{q2} = \omega_{q2}^{(0)} \sqrt{\left|\cos\left(\frac{\pi\Phi}{\Phi_0}\right)\right|}$, with the external flux Φ the parameter that we change. In order for the theoretical predictions and experimental measurements, like those in [34] and [35], to be in agreement, we cannot use directly Eq. B.8. Whereas, we set the reference level of the energy to be that of the $|11\rangle$ state, which has the eigenvalue f_1. Therefore, the theoretical prediction that agrees with the experiments is given by:

$$f(\omega_{q2}) = \frac{\omega_{q1} + \omega_{q2}}{2} \pm \frac{\sqrt{(\omega_{q2} - \omega_{q1})^2 + 4J^2}}{2} \tag{B.9}$$

References

[1] Dmitry A Fedorov et al. "Ab initio molecular dynamics on quantum computers". In: *The Journal of Chemical Physics* 154.16 (2021), p. 164103 (cit. on p. 3).

[2] Yudong Cao, Jhonathan Romero, and Alán Aspuru-Guzik. "Potential of quantum computing for drug discovery". In: *IBM Journal of Research and Development* 62.6 (2018), pp. 6–1 (cit. on p. 3).

[3] Göran Wendin. "Quantum information processing with superconducting circuits: a review". In: *Reports on Progress in Physics* 80.10 (2017), p. 106001 (cit. on pp. 3, 5).

[4] Philip Krantz et al. "A quantum engineer's guide to superconducting qubits". In: *Applied Physics Reviews* 6.2 (2019), p. 021318 (cit. on pp. 5, 6, 8–10, 13–15, 18, 19, 21–23, 25, 27–29, 41, 44–49).

[5] Diego Ristè et al. "Initialization by measurement of a superconducting quantum bit circuit". In: *Physical review letters* 109.5 (2012), p. 050507 (cit. on p. 6).

[6] Julian Kelly et al. "Optimal quantum control using randomized benchmarking". In: *Physical review letters* 112.24 (2014), p. 240504 (cit. on pp. 6, 30, 72, 73, 76, 77).

[7] Antonio D Córcoles et al. "Process verification of two-qubit quantum gates by randomized benchmarking". In: *Physical Review A* 87.3 (2013), p. 030301 (cit. on p. 6).

[8] S Poletto et al. "Entanglement of two superconducting qubits in a waveguide cavity via monochromatic two-photon excitation". In: *Physical review letters* 109.24 (2012), p. 240505 (cit. on p. 6).

[9] Jens Koch et al. "Charge-insensitive qubit design derived from the Cooper pair box". In: *Physical Review A* 76.4 (2007), p. 042319 (cit. on pp. 6, 11–13, 20, 26, 63).

[10] Youngkyu Sung et al. "Realization of High-Fidelity CZ and Z Z-Free iSWAP Gates with a Tunable Coupler". In: *Physical Review X* 11.2 (2021), p. 021058 (cit. on pp. 6, 25, 48).

[11] Aaron Somoroff et al. "Millisecond coherence in a superconducting qubit". In: *arXiv preprint arXiv:2103.08578* (2021) (cit. on pp. 6, 48, 73).

[12] Elizabeth Gibney. "Hello quantum world! Google publishes landmark quantum supremacy claim". In: *Nature* 574.7779 (2019), pp. 461–463 (cit. on p. 6).

[13] Diego Garcıa-Martın and Germán Sierra. "Five experimental tests on the 5-qubit IBM quantum computer". In: *arXiv preprint arXiv:1712.05642* (2017) (cit. on pp. 6, 22).

[14] Charles P Poole, Horacio A Farach, and Richard J Creswick. *Superconductivity*. Academic press, 2013 (cit. on pp. 6, 7).

[15] Antonio Barone and Gianfranco Paterno. *Physics and applications of the Josephson effect*. Vol. 1. Wiley Online Library, 1982 (cit. on pp. 7, 9, 10).

[16] Michael Tinkham. *Introduction to superconductivity*. Courier Corporation, 2004 (cit. on p. 7).

[17] David Niepce. "Nanowire Superinductors". PhD thesis. Chalmers Tekniska Hogskola (Sweden), 2018 (cit. on pp. 7, 38, 39).

[18] Uri Vool and Michel Devoret. "Introduction to quantum electromagnetic circuits". In: *International Journal of Circuit Theory and Applications* 45.7 (2017), pp. 897–934 (cit. on p. 7).

[19] Markus Jerger. "Experiments on superconducting qubits coupled to resonators". In: (2013) (cit. on p. 14).

[20] Claude Cohen-Tannoudji, Bernard Diu, and Frank Laloe. "Quantum Mechanics, Volume 2". In: *Quantum Mechanics* 2 (1986), p. 626 (cit. on pp. 16, 17).

[21] J Clarke and AI Braginski. *The squid handbook: Applications of squids and squid systems. vol. 2*. 2006 (cit. on p. 20).

[22] MD Hutchings et al. "Tunable superconducting qubits with flux-independent coherence". In: *Physical Review Applied* 8.4 (2017), p. 044003 (cit. on pp. 22, 65).

[23] Frank Arute et al. "Quantum supremacy using a programmable superconducting processor". In: *Nature* 574.7779 (2019), pp. 505–510 (cit. on p. 22).

[24] Matthew Reagor et al. "Demonstration of universal parametric entangling gates on a multi-qubit lattice". In: *Science advances* 4.2 (2018), eaao3603 (cit. on p. 22).

[25] Kristel Michielsen et al. "Benchmarking gate-based quantum computers". In: *Computer Physics Communications* 220 (2017), pp. 44–55 (cit. on p. 22).

[26] A-SF Obada et al. "Efficient protocol of N-bit discrete quantum Fourier transform via transmon qubits coupled to a resonator". In: *Quantum information processing* 13.2 (2014), pp. 475–489 (cit. on p. 22).

[27] Andreas Dewes. "Demonstrating quantum speed-up with a two-transmon quantum processor". PhD thesis. Université Pierre et Marie Curie-Paris VI, 2012 (cit. on p. 22).

[28] Richard Versluis et al. "Scalable quantum circuit and control for a superconducting surface code". In: *Physical Review Applied* 8.3 (2017), p. 034021 (cit. on pp. 22, 30, 77).

[29] Adam M Meier. "Randomized benchmarking of Clifford operators". PhD thesis. University of Colorado at Boulder, 2013 (cit. on pp. 23, 24).

[30] JM Chow et al. "Randomized benchmarking and process tomography for gate errors in a solid-state qubit". In: *Physical review letters* 102.9 (2009), p. 090502 (cit. on pp. 24, 54, 72, 73).

[31] Kristine Boone. "Concepts and methods for benchmarking quantum computers". In: (2021) (cit. on p. 24).

[32] Tahereh Abad et al. "Universal fidelity reduction of quantum operations from weak dissipation". In: *arXiv preprint arXiv:2110.15883* (2021) (cit. on pp. 25, 66).

[33] Fei Yan et al. "Tunable coupling scheme for implementing high-fidelity two-qubit gates". In: *Physical Review Applied* 10.5 (2018), p. 054062 (cit. on pp. 25, 76, 77).

[34] Johannes Majer et al. "Coupling superconducting qubits via a cavity bus". In: *Nature* 449.7161 (2007), pp. 443–447 (cit. on pp. 26, 75, 79, 80).

[35] S Filipp et al. “Multi-mode mediated exchange coupling in cavity QED”. In: *arXiv preprint arXiv:1011.3732* (2010) (cit. on pp. 26, 27, 80).

[36] Elena Ferraro et al. “Universal set of quantum gates for the flip-flop qubit in the presence of 1/f noise”. In: *EPJ Quantum Technology* 9.1 (2022), pp. 1–11 (cit. on p. 29).

[37] Matthias Steffen et al. “Decoherence of floating qubits due to capacitive coupling”. In: *New Journal of Physics* 11.3 (2009), p. 033030 (cit. on p. 30).

[38] Austin G Fowler et al. “Surface codes: Towards practical large-scale quantum computation”. In: *Physical Review A* 86.3 (2012), p. 032324 (cit. on pp. 30, 48, 77).

[39] HaiJie Li et al. “Experimental demonstrations of high-Q superconducting coplanar waveguide resonators”. In: *Chinese Science Bulletin* 58.20 (2013), pp. 2413–2417 (cit. on p. 32).

[40] *BF-LD-Series*. https://bluefors.com/products/ld-dilution-refrigerator (cit. on p. 33).

[41] OV Lounasmaa. “Dilution refrigeration”. In: *Journal of Physics E: Scientific Instruments* 12.8 (1979), p. 668 (cit. on p. 33).

[42] *LNF-LNC4$_8$CDatasheet*. https://quantummicrowave.com/wp-content/uploads/2016/10/lnf-lnc4_8c-2.pdf (cit. on p. 36).

[43] *LNF-PBA Datasheet*. https://quantummicrowave.com/wp-content/uploads/2019/10/LNF-PBA_Manual_R4-1.pdf (cit. on p. 36).

[44] *LNF-PS3b Datasheet*. https://quantummicrowave.com/wp-content/uploads/2019/10/LNF-PS3b_Manual.pdf (cit. on p. 36).

[45] *LNF-ISC4$_8$A*. https://lownoisefactory.com/product/4-8-ghz-single-junction-isolator-circulator/ (cit. on p. 36).

[46] *M9802A PXIe VNA*. https://www.keysight.com/it/en/assets/3119-1014/data-sheets/5992-3596.pdf (cit. on p. 36).

[47] Halima Giovanna Ahmad. “Physics of the Josephson effect in junctions with ferromagnetic barriers towards quantum circuits and RF applications”. In: (2021) (cit. on p. 36).

[48] *Keysight M3202A AWG*. https://www.keysight.com/it/en/assets/7018-05392/data-sheets/5992-1798.pdf (cit. on pp. 36, 37).

[49] *SC5505a*. https://downloads.signalcore.com/sc5505x_6x/SC5505A_Datasheet.pdf (cit. on p. 36).

[50] *SC5502a*. https://downloads.signalcore.com/sc5502x_3x/SC5502A_Manual.pdf (cit. on p. 36).

[51] *SC5510a*. https://downloads.signalcore.com/sc5510x_11x/sc5510a_datasheet.pdf (cit. on p. 36).

[52] *Keysight M3102A Digitizer*. https://www.keysight.com/it/en/assets/7018-05399/data-sheets/5992-1805.pdf (cit. on pp. 36, 37).

[53] $Pickering_41 - 182B - 006$. https://www.pickeringtest.com/content/downloads/datasheets/41-43-182BD.pdf (cit. on p. 36).

[54] Shan Williams Jolin et al. “Calibration of mixer amplitude and phase imbalance in superconducting circuits”. In: *Review of Scientific Instruments* 91.12 (2020), p. 124707 (cit. on p. 37).

[55] *Labber software from Keysight*. https://www.keysight.com/it/en/products/software/application-sw/labber-software.html (cit. on p. 38).

[56] Hanhee Paik et al. “How coherent are Josephson junctions?” In: *Bulletin of the American Physical Society* 57 (2012) (cit. on pp. 40, 41).

[57] Mahdi Naghiloo. “Introduction to experimental quantum measurement with superconducting qubits”. In: *arXiv preprint arXiv:1904.09291* (2019) (cit. on pp. 43, 44).

[58] Grégoire Ithier. “Manipulation, readout and analysis of the decoherence of a superconducting quantum bit”. PhD thesis. Université Pierre et Marie Curie-Paris VI, 2005 (cit. on p. 44).

[59] Abhinandan Antony et al. “Miniaturizing transmon qubits using van der Waals materials”. In: *Nano letters* 21.23 (2021), pp. 10122–10126 (cit. on p. 46).

[60] Jonas Bylander et al. “Noise spectroscopy through dynamical decoupling with a superconducting flux qubit”. In: *Nature Physics* 7.7 (2011), pp. 565–570 (cit. on p. 47).

[61] Ehsan Zahedinejad, Joydip Ghosh, and Barry C Sanders. “High-fidelity single-shot Toffoli gate via quantum control”. In: *Physical review letters* 114.20 (2015), p. 200502 (cit. on p. 48).

[62] David Shaw. *Quantum Hardware Outlook 2022*. Tech. rep. tech. rep., Fact Based Insight, 2022 (cit. on p. 48).

[63] Zijun Chen et al. “Measuring and suppressing quantum state leakage in a superconducting qubit”. In: *Physical review letters* 116.2 (2016), p. 020501 (cit. on pp. 48, 50, 51, 66, 68, 73).

[64] Matthew Reed. *Entanglement and quantum error correction with superconducting qubits*. Lulu. com, 2013 (cit. on pp. 51–53, 71).

[65] *QuTiP*. https://qutip.org/index.html (cit. on p. 52).

[66] Timothy Proctor et al. “What randomized benchmarking actually measures”. In: *Physical review letters* 119.13 (2017), p. 130502 (cit. on pp. 55, 73).

[67] Easwar Magesan, Jay M Gambetta, and Joseph Emerson. “Scalable and robust randomized benchmarking of quantum processes”. In: *Physical review letters* 106.18 (2011), p. 180504 (cit. on p. 55).

[68] *Resonator tools from Sebastian Probst*. https://github.com/sebastianprobst/resonator_tools.git (cit. on pp. 57–59).

[69] Luigi Frunzio et al. “Fabrication and characterization of superconducting circuit QED devices for quantum computation”. In: *IEEE transactions on applied superconductivity* 15.2 (2005), pp. 860–863 (cit. on p. 58).

[70] *Non-Linear Least-Squares Minimization and Curve fitting*. https://lmfit.github.io/lmfit-py/ (cit. on p. 60).

[71] Michiel A Rol et al. “Time-domain characterization and correction of on-chip distortion of control pulses in a quantum processor”. In: *Applied Physics Letters* 116.5 (2020), p. 054001 (cit. on pp. 75, 77).

[72] Daniel J Egger and Frank K Wilhelm. “Optimized controlled-Z gates for two superconducting qubits coupled through a resonator”. In: *Superconductor Science and Technology* 27.1 (2013), p. 014001 (cit. on p. 77).

[73] Michele C Collodo et al. “Implementation of Conditional Phase Gates Based on Tunable Z Z Interactions”. In: *Physical Review Letters* 125.24 (2020), p. 240502 (cit. on p. 77).